

1 SEARCH FOR PRODUCTION OF A HIGGS BOSON AND A SINGLE TOP  
2 QUARK IN MULTILEPTON FINAL STATES IN  $pp$  COLLISIONS AT  $\sqrt{s} = 13$   
3 TeV.

4 by

5 Jose Andres Monroy Montañez

# A DISSERTATION

7 Presented to the Faculty of

8 The Graduate College at the University of Nebraska

In Partial Fulfilment of Requirements

10 For the Degree of Doctor of Philosophy

11 Major: Physics and Astronomy

12 Under the Supervision of Kenneth Bloom and Aaron Dominguez

13 Lincoln, Nebraska

14 July, 2018

15 SEARCH FOR PRODUCTION OF A HIGGS BOSON AND A SINGLE TOP  
16 QUARK IN MULTILEPTON FINAL STATES IN pp COLLISIONS AT  $\sqrt{s} = 13$   
17 TeV.

18 Jose Andres Monroy Montañez, Ph.D.

19 University of Nebraska, 2018

20 Adviser: Kenneth Bloom and Aaron Dominguez

# **<sup>21</sup> Table of Contents**

<b><sup>22</sup> Table of Contents</b>	<b>iii</b>
<b><sup>23</sup> List of Figures</b>	<b>vii</b>
<b><sup>24</sup> List of Tables</b>	<b>x</b>
<b><sup>25</sup> 1 INTRODUCTION</b>	<b>1</b>
<b><sup>26</sup> 2 Theoretical approach</b>	<b>2</b>
27     2.1 Introduction . . . . .	2
28     2.2 Standard model of particle physics . . . . .	3
29     2.2.1 Fermions . . . . .	5
30     2.2.1.1 Leptons . . . . .	6
31     2.2.1.2 Quarks . . . . .	8
32     2.2.2 Fundamental interactions . . . . .	13
33     2.2.3 Gauge bosons . . . . .	18
34     2.3 Electroweak unification and the Higgs mechanism . . . . .	20
35     2.3.1 Spontaneous symmetry breaking (SSB) . . . . .	28
36     2.3.2 Higgs mechanism . . . . .	32
37     2.3.3 Masses of the gauge bosons . . . . .	35

38	2.3.4	Masses of the fermions . . . . .	36
39	2.3.5	The Higgs field . . . . .	37
40	2.3.6	Production of Higgs bosons at LHC . . . . .	38
41	2.3.7	Higgs boson decay channels . . . . .	42
42	2.4	Associated production of a Higgs boson and a single Top quark. . . . .	43
43	2.5	The CP-mixing in tH processes . . . . .	47
44	2.6	Experimantal status of the anomalous Higg-fermion coupling. . . . .	52
45	<b>3</b>	<b>The CMS experiment at the LHC</b>	<b>54</b>
46	3.1	Introduction . . . . .	54
47	3.2	The LHC . . . . .	55
48	3.3	The CMS experiment . . . . .	65
49	3.3.1	Coordinate system . . . . .	67
50	3.3.2	Pixels detector . . . . .	68
51	3.3.3	Silicon strip tracker . . . . .	70
52	3.3.4	Electromagnetic calorimeter . . . . .	72
53	3.3.5	Hadronic calorimeter . . . . .	73
54	3.3.6	Superconducting solenoid magnet . . . . .	75
55	3.3.7	Muon system . . . . .	76
56	3.3.8	CMS trigger system . . . . .	77
57	3.3.9	CMS computing . . . . .	79
58	<b>4</b>	<b>Event generation, simulation and reconstruction</b>	<b>83</b>
59	4.1	Event generation . . . . .	84
60	4.2	Monte Carlo Event Generators. . . . .	88
61	4.3	CMS detector simulation. . . . .	89
62	4.4	Event reconstruction. . . . .	91

63	4.4.1	Particle-Flow Algorithm. . . . .	91
64	4.4.1.1	Missing transverse energy. . . . .	103
65	4.4.2	Event reconstruction examples . . . . .	104
66	<b>5 Statistical methods</b>		<b>107</b>
67	5.1	Multivariate analysis . . . . .	107
68	5.1.1	Decision trees . . . . .	110
69	5.1.2	Boosted decision trees (BDT). . . . .	113
70	5.1.3	Overtraining. . . . .	116
71	5.1.4	Variable ranking. . . . .	116
72	5.1.5	BDT output example. . . . .	117
73	5.2	Statistical inference. . . . .	118
74	5.2.1	Nuisance parameters. . . . .	118
75	5.2.2	Maximum likelihood estimation method . . . . .	119
76	5.2.3	Hypothesis test . . . . .	120
77	5.3	exclusion limits . . . . .	121
78	5.4	asymptotic limits . . . . .	121
79	<b>6 Search for production of a Higgs boson and a single top quark in multilepton final states in pp collisions at <math>\sqrt{s} = 13</math> TeV</b>		<b>122</b>
81	6.1	Introduction . . . . .	122
82	6.2	$tHq$ signature . . . . .	124
83	6.3	Background processes . . . . .	126
84	6.4	Object Identification and event selection . . . . .	128
85	6.4.1	Jets and $b$ tagging. . . . .	128
86	6.4.2	Missing Energy MET. . . . .	129
87	6.4.3	Lepton reconstruction and identification . . . . .	130

88	6.4.4 Lepton selection efficiency . . . . .	138
89	6.5 Data and MC Samples . . . . .	141
90	6.5.1 Full 2016 dataset and MC samples . . . . .	142
91	6.5.2 Triggers . . . . .	142
92	6.6 Background predictions . . . . .	146
93	6.7 Signal discrimination . . . . .	147
94	6.7.1 Classifiers response . . . . .	151
95	6.8 Additional discriminating variables . . . . .	154
96	<b>Bibliography</b>	<b>155</b>
97	<b>References</b>	<b>157</b>

## <sup>98</sup> List of Figures

99	2.1 Standard model of particle physics. . . . .	4
100	2.2 Transformations between quarks . . . . .	12
101	2.3 Fundamental interactions in nature. . . . .	13
102	2.4 SM interactions diagrams . . . . .	14
103	2.5 Neutral current processes . . . . .	21
104	2.6 Spontaneous symmetry breaking mechanism . . . . .	29
105	2.7 SSB Potential form . . . . .	30
106	2.8 Potential for complex scalar field . . . . .	31
107	2.9 SSB mechanism for complex scalar field . . . . .	32
108	2.10 Proton-Proton collision . . . . .	39
109	2.11 Higgs boson production mechanism Feynman diagrams . . . . .	40
110	2.12 Higgs boson production cross section and decay branching ratios . . . . .	41
111	2.13 Associated Higgs boson production mechanism Feynman diagrams . . . . .	43
112	2.14 Cross section for tHq process as a function of $\kappa_t$ . . . . .	46
113	2.15 Cross section for $tHW$ process as a function of $\kappa_{Htt}$ . . . . .	47
114	2.16 NLO cross section for $tX_0$ and $t\bar{t}X_0$ . . . . .	50
115	2.17 NLO cross section for $tWX_0$ , $t\bar{t}X_0$ . . . . .	51

116	2.18 Two dimentional $\kappa_t$ - $\kappa_V$ plot of the coupling modifiers. ATLAS and CMS 117 combination. . . . .	52
118	3.1 CERN accelerator complex . . . . .	55
119	3.2 LHC protons source. First acceleration stage. . . . .	56
120	3.3 The LINAC2 accelerating system at CERN. . . . .	57
121	3.4 LHC layout and RF cavities module. . . . .	58
122	3.5 LHC dipole magnet. . . . .	60
123	3.6 Integrated luminosity delivered by LHC and recorded by CMS during 2016	62
124	3.7 LHC interaction points . . . . .	63
125	3.8 Multiple $pp$ collision bunch crossing at CMS. . . . .	65
126	3.9 Layout of the CMS detector . . . . .	66
127	3.10 CMS detector coordinate system . . . . .	67
128	3.11 CMS pixel detector schematic view. . . . .	70
129	3.12 SST Schematic view. . . . .	71
130	3.13 CMS ECAL schematic view . . . . .	72
131	3.14 CMS HCAL schematic view . . . . .	74
132	3.15 CMS solenoid magnet . . . . .	75
133	3.16 CMS Muon system schematic view . . . . .	76
134	3.17 CMS Level-1 trigger architecture . . . . .	78
135	3.18 WLCG structure . . . . .	80
136	3.19 Data flow from CMS detector through hardware Tiers . . . . .	82
137	4.1 Event generation process. . . . .	84
138	4.2 Particle flow algorithm. . . . .	92
139	4.3 Jet reconstruction. . . . .	100
140	4.4 Jet energy corrections. . . . .	101

141	4.5	Secondary vertex in a b-hadron decay.	102
142	4.6	HIG-13-004 Event 1 reconstruction.	104
143	4.7	$e\mu$ event reconstruction.	105
144	4.8	Recorded event reconstruction.	106
145	5.1	Scatter plots-MVA event classification.	109
146	5.2	Scalar test statistical.	109
147	5.3	Decision tree.	111
148	5.4	Decision tree output example.	114
149	5.5	BDT output example.	117
150	6.1	$tHq$ event signature.	125
151	6.2	$t\bar{t}$ and $t\bar{t}W$ events signature.	127
152	6.3	Tight vs loose lepton selection efficiencies in the 2lss channel.	138
153	6.4	Tight vs loose lepton selection efficiencies in the 3l channel.	139
154	6.5	Input variables to the BDT for signal discrimination normalized.	148
155	6.6	Input variables to the BDT for signal discrimination not normalized.	150
156	6.7	BDT inputs as seen by TMVA against $t\bar{t}$ .	151
157	6.8	BDT inputs as seen by TMVA against $t\bar{t}V$ .	152
158	6.9	Correlation matrices for the input variables in the TMVA.	153
159	6.10	MVA classifiers performance.	153
160	6.11	Additional discriminating variables distributions.	155

# <sup>161</sup> List of Tables

162	2.1	Fermions of the SM. . . . .	5
163	2.2	Fermion masses. . . . .	6
164	2.3	Leptons properties. . . . .	9
165	2.4	Quarks properties. . . . .	9
166	2.5	Fermion weak isospin and weak hypercharge multiplets. . . . .	11
167	2.6	Fundamental interactions features. . . . .	15
168	2.7	SM gauge bosons. . . . .	20
169	2.8	Higgs boson properties. . . . .	38
170	2.9	Predicted branching ratios for a SM Higgs boson with $m_H = 125 \text{ GeV}/c^2$ . . . . .	42
171	2.10	Predicted SM cross sections for tH production at $\sqrt{s} = 13 \text{ TeV}$ . . . . .	44
172	2.11	Predicted enhancement of the $tHq$ and $tHW$ cross sections at LHC . . . . .	48
173	6.1	Effective areas, for electrons and muons. . . . .	134
174	6.2	Requirements on each of the three muon selections. . . . .	137
175	6.3	Criteria for each of the three electron selections. . . . .	137
176	6.4	Signal samples and their cross section and branching fraction. . . . .	142
177	6.5	$\kappa_V$ and $\kappa_t$ combinations. . . . .	143
178	6.6	List of background samples used in this analysis (CMSSW 80X). . . . .	144
179	6.7	Leading-order $t\bar{t}W$ and $t\bar{t}Z$ samples used in the signal BDT training. . . . .	144

180	6.8	Table of high-level triggers that we consider in the analysis. . . . .	145
181	6.9	Trigger efficiency scale factors and associated uncertainties. . . . .	145
182	6.10	MVA input discriminating variables . . . . .	149
183	6.11	TMVA input variables ranking for BDTA_GRAD method . . . . .	154
184	6.12	TMVA configuration used in the BDT training. . . . .	154
185	6.13	ROC-integral for all the testing cases. . . . .	156

<sup>186</sup> Chapter 1

<sup>187</sup> INTRODUCTION

<sup>188</sup> **Chapter 2**

<sup>189</sup> **Theoretical approach**

<sup>190</sup> **2.1 Introduction**

<sup>191</sup> The physical description of the universe is a challenge that physicists have faced by  
<sup>192</sup> making theories that refine existing principles and proposing new ones in an attempt  
<sup>193</sup> to embrace emerging facts and phenomena.

<sup>194</sup>

<sup>195</sup> At the end of 1940s Julian Schwinger [1] and Richard P. Feynman [2], based in the  
<sup>196</sup> work of Sin-Itiro Tomonaga [3], developed an electromagnetic theory consistent with  
<sup>197</sup> special relativity and quantum mechanics that describes how matter and light inter-  
<sup>198</sup> act; the so-called “quantum eletrodynamics” (QED) had born.

<sup>199</sup>

<sup>200</sup> QED has become the guide in the development of theories that describe the universe.  
<sup>201</sup> It was the first example of a quantum field theory (QFT), which is the theoretical  
<sup>202</sup> framework for building quantum mechanical models that describes particles and their  
<sup>203</sup> interactions. QFT is composed of a set of mathematical tools that combines classical  
<sup>204</sup> fields, special relativity and quantum mechanics, while keeping the quantum point

205 particles and locality ideas.

206 This chapter gives an overview of the standard model of particle physics, starting  
 207 with a description of the particles and interactions that compose it, followed by a  
 208 description of the electroweak interaction, the Higgs boson and the associated pro-  
 209 duction of Higgs boson and a single top quark ( $tH$ ). The description contained in  
 210 this chapter is based on references [4–6].

## 211 2.2 Standard model of particle physics

212 Particle physics at the fundamental level is modeled in terms of a collection of in-  
 213 teracting particles and fields in a theory known as the “standard model of particle  
 214 physics (SM)”<sup>1</sup>.

215

216 The full picture of the SM is composed of three fields<sup>2</sup>, whose excitations are inter-  
 217 preted as particles called mediators or force-carriers; a set of fields, whose excitations  
 218 are interpreted as elementary particles, interacting through the exchange of those  
 219 mediators and a field that gives the mass to elementary particles. Figure 2.1 shows  
 220 an scheme of the SM particles organization. In addition to the particles in the scheme  
 221 (but not listed in it), their corresponding anti-particles, with opposite quantum num-  
 222 bers, are also part of the picture; some particles are their own anti-particles, like  
 223 photon or Higgs, or anti-particle is already listed like in the  $W^+$  and  $W^-$  case.

224

225 The mathematical formulation of the SM is based on group theory and the use of  
 226 Noether’s theorem [8] which states that for a physical system modeled by a Lagrangian

---

<sup>1</sup> The formal and complete treatment of the SM is out of the scope of this document, however a plenty of textbooks describing it at several levels are available in the literature. The treatment in references [?] is quite comprehensive and detailed.

<sup>2</sup> Note that gravitational field is not included in the standard model formulation

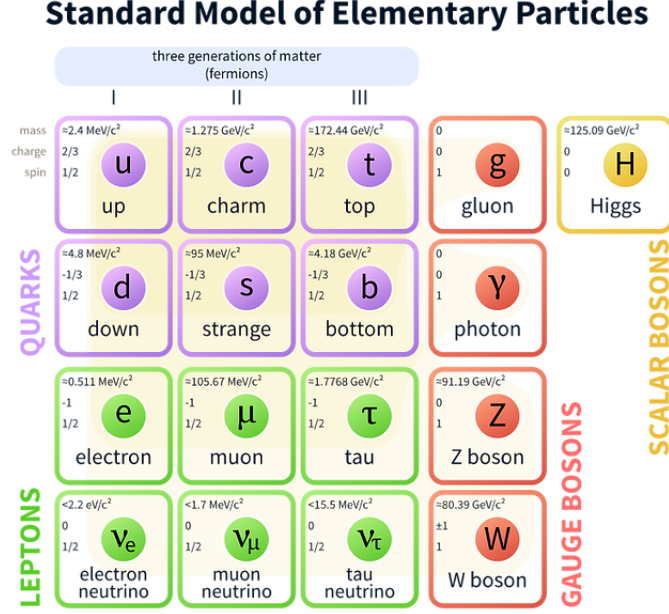


**Figure 2.1:** Schematic representation of the Standard model of particle physics. SM is a theoretical model intended to describe three of the four fundamental forces of the universe in terms of a set of particles and their interactions. [7].

227 that is invariant under a group of transformations a conservation law is expected. For  
 228 instance, a system described by a time-independent Lagrangian is invariant (symmet-  
 229 ric) under time changes (transformations) with the total energy conservation law as  
 230 the expected conservation law. In QED, the charge operator ( $Q$ ) is the generator of  
 231 the  $U(1)$  symmetry which according to the Noether's theorem means that there is a  
 232 conserved quantity; this conserved quantity is the electric charge and thus the law  
 233 conservation of electric charge is established.

234

235 In the SM, the symmetry group  $SU(3)_C \otimes SU(2)_L \otimes U(1)_Y$  describes three of the  
 236 four fundamental interactions in nature(see section 2.2.2): strong interaction(SI),  
 237 weak interaction(WI) and electromagnetic interactions (EI) in terms of symmetries  
 238 associated to physical quantities:

- 239     • Strong:  $SU(3)_C$  associated to color charge
- 240     • Weak:  $SU(2)_L$  associated to weak isospin and chirality
- 241     • Electromagnetic:  $U(1)_Y$  associated to weak hypercharge and electric charge
- 242   It will be shown that the electromagnetic and weak interactions are combined in  
 243   the so-called electroweak interaction where chirality, hypercharge, weak isospin and  
 244   electric charge are the central concepts.

245   **2.2.1 Fermions**

246   The basic constituents of the ordinary matter at the lowest level, which form the set  
 247   of elementary particles in the SM formulation, are quarks and leptons. All of them  
 248   have spin 1/2, therefore they are classified as fermions since they obey Fermi-Dirac  
 249   statistics. There are six “flavors” of quarks and three of leptons organized in three  
 250   generations, or families, as shown in table 2.1.

251

		Generation		
		1st	2nd	3rd
Leptons	Charged	Electron (e)	Moun( $\mu$ )	Tau ( $\tau$ )
	Neutral	Electron neutrino ( $\nu_e$ )	Muon neutrino ( $\nu_\mu$ )	Tau neutrino ( $\nu_\tau$ )
Quarks	Up-type	Up (u)	Charm (c)	Top (t)
	Down-type	Down (d)	Strange (s)	Bottom (b)

**Table 2.1:** Fermions of the SM. There are six flavors of quarks and three of leptons, organized in three generations, or families, composed of two pairs of closely related particles. The close relationship is motivated by the fact that WI between leptons is limited to the members of the same generation; WI between quarks is not limited but greatly favoured, to same generation members.

252

253   There is a mass hierarchy between generations (see table 2.2), where the higher gener-  
 254   ation particles decays to the lower one, which can explain why the ordinary matter is

made of particles in the first generation. In the SM, neutrinos are modeled as massless particles so they are not subject to this mass hierarchy; however, today it is known that neutrinos are massive so the hierarchy could be restated. The reason behind this mass hierarchy is one of the most important open questions in particle physics, and it becomes more puzzling when noticing that the mass difference between first and second generation fermions is small compared to the mass difference with respect to the third generation.

Lepton	Mass (MeV/c <sup>2</sup> )	Quark	Mass (MeV/c <sup>2</sup> )
e	0.51	u	2.2
$\mu$	105.65	c	$1.28 \times 10^3$
$\tau$	1776.86	t	$173.1 \times 10^3$
$\nu_e$	Unknown	d	4.7
$\nu_\mu$	Unknown	s	96
$\tau_\mu$	Unknown	b	$4.18 \times 10^3$

**Table 2.2:** Fermion masses [9]. Generations differ by mass in a way that have been interpreted as a masss hierarchy. Approximate values with no uncertainties are used, for comparison purpose.

Usually, the second and third generation fermions are produced in high energy processes, like the ones recreated in particle accelerators.

### 2.2.1.1 Leptons

A lepton is an elementary particle that is not subject to the SI. As seen in table 2.1, there are two types of leptons, the charged ones (electron, muon and tau) and the neutral ones (the three neutrinos). The electric charge (Q) is the property that gives leptons the ability to participate in the EI. From the classical point of view, Q plays a central role determining, among others, the strength of the electric field through which the electromagnetic force is exerted. It is clear that neutrinos are not affected

272 by EI because they don't carry electric charge.

273

274 Another feature of the leptons that is fundamental in the mathematical description  
275 of the SM is the chirality, which is closely related to spin and helicity. Helicity defines  
276 the handedness of a particle by relating its spin and momentum such that if they  
277 are parallel then the particle is right-handed; if spin and momentum are antiparallel  
278 the particle is said to be left-handed. The study of parity conservation (or viola-  
279 tion) in  $\beta$ -decay has shown that only left-handed electrons/neutrinos or right-handed  
280 positrons/anti-neutrinos are created [10]; the inclusion of that feature in the theory  
281 was achieved by using projection operators for helicity, however, helicity is frame de-  
282 pendent for massive particles which makes it not Lorentz invariant and then another  
283 related attribute has to be used: *chirality*.

284

285 Chirality is a purely quantum attribute which makes it not so easy to describe in  
286 graphical terms but it defines how the wave function of a particle transforms under  
287 certain rotations. As with helicity, there are two chiral states, left-handed chiral (L)  
288 and right-handed chiral (R). In the highly relativistic limit where  $E \approx p \gg m$  helicity  
289 and chirality converge, becoming exactly the same for massless particles.

290

291 In the following, when referring to left-handed (right-handed) it will mean left-handed  
292 chiral (right-handed chiral). The fundamental fact about chirality is that while EI  
293 and SI are not sensitive to chirality, in WI left-handed and right-handed fermions are  
294 treated asymmetrically, such that only left handed fermions and right-handed anti-  
295 fermions are allowed to couple to WI mediators, which is a violation of parity. The  
296 way to translate this statement in a formal mathematical formulation is based on the  
297 isospin symmetry group  $SU(2)_L$ .

298

299 Each generation of leptons is seen as a weak isospin doublet.<sup>3</sup> The left-handed charged  
 300 lepton and its associated left-handed neutrino are arranged in doublets of weak isospin  
 301 T=1/2 while their right-handed partners are singlets:

$$\begin{pmatrix} \nu_l \\ l \end{pmatrix}_L, l_R := \begin{pmatrix} \nu_e \\ e \end{pmatrix}_L, \begin{pmatrix} \nu_\mu \\ \mu \end{pmatrix}_L, \begin{pmatrix} \nu_\tau \\ \tau \end{pmatrix}_L, e_R, \mu_R, \tau_R, \nu_{eR}, \nu_{\mu R}, \nu_{\tau R} \quad (2.1)$$

302 The isospin third component refers to the eigenvalues of the weak isospin operator  
 303 which for doublets is  $T_3 = \pm 1/2$ , while for singlets it is  $T_3 = 0$ . The physical meaning  
 304 of this doublet-singlet arrangement falls in that the WI couples the two particles in  
 305 the doublet by exchanging the interaction mediator while the singlet member is not  
 306 involved in WI. The main properties of the leptons are summarized in table 2.3.

307

308 Altough all three flavor neutrinos have been observed, their masses remain unknown  
 309 and only some estimations have been made [11]. The main reason is that the fla-  
 310 vor eigenstates are not the same as the mass eigenstates which implies that when  
 311 a neutrino is created its mass state is a linear combination of the three mass eigen-  
 312 states and experiments can only probe the squared difference of the masses. The  
 313 Pontecorvo-Maki-Nakagawa-Sakata (PMNS) mixing matrix encode the relationship  
 314 between flavor and mass eigenstates.

315

### 316 2.2.1.2 Quarks

317 Quarks are the basic constituents of protons and neutrons. The way quarks join to  
 318 form bound states, called “hadrons”, is through the SI. Quarks are affected by all the

---

<sup>3</sup> The weak isospin is an analogy of the isospin symmetry in strong interaction where neutron and proton are affected equally by strong force but differ in their charge.

Lepton	Q(e)	$T_3$	$L_e$	$L_\mu$	$L_\tau$	Lifetime (s)
Electron (e)	-1	-1/2	1	0	0	Stable
Electron neutrino( $\nu_e$ )	0	1/2	1	0	0	Unknown
Muon ( $\mu$ )	-1	-1/2	0	1	0	$2.19 \times 10^{-6}$
Muon neutrino ( $\nu_\mu$ )	0	1/2	0	1	0	Unknown
Tau ( $\tau$ )	-1	-1/2	0	0	1	$290.3 \times 10^{-15}$
Tau neutrino ( $\tau_\mu$ )	0	1/2	0	0	1	Unknown

**Table 2.3:** Leptons properties [9]. Q: electric charge,  $T_3$ : weak isospin. Only left-handed leptons and right-handed anti-leptons participate in the WI. Anti-particles with inverted  $T_3$ , Q and lepton number complete the leptons set but are not listed. Right-handed leptons and left-handed anti-leptons, neither listed, form weak isospin singlets with  $T_3 = 0$  and do not take part in the weak interaction.

319 fundamental interactions which means that they carry all the four types of charges:  
 320 color, electric charge, weak isospin and mass.

Flavor	Q(e)	$I_3$	$T_3$	B	C	S	T	$B'$	Y	Color
Up (u)	2/3	1/2	1/2	1/3	0	0	0	0	1/3	r,b,g
Charm (c)	2/3	0	1/2	1/3	1	0	0	0	4/3	r,b,g
Top(t)	2/3	0	1/2	1/3	0	0	1	0	4/3	r,b,g
Down(d)	-1/3	-1/2	-1/2	1/3	0	0	0	0	1/3	r,b,g
Strange(s)	-1/3	0	-1/2	1/3	0	-1	0	0	-2/3	r,b,g
Bottom(b)	-1/3	0	-1/2	1/3	0	0	0	-1	-2/3	r,b,g

**Table 2.4:** Quarks properties [9]. Q: electric charge,  $I_3$ : isospin,  $T_3$ : weak isospin, B: baryon number, C: charmness, S: strangeness, T: topness,  $B'$ : bottomness, Y: hypercharge. Anti-quarks posses the same mass and spin as quarks but all charges (color, flavor numbers) have opposite sign.

321  
 322 Table 2.4 summarizes the features of quarks, among which the most particular is  
 323 their fractional electric charge. Note that fractional charge is not a problem, given  
 324 that quarks are not found isolated, but serves to explain how composed particles are  
 325 formed out of two or more valence quarks<sup>4</sup>.

326

---

<sup>4</sup> Hadrons can contain an indefinite number of virtual quarks and gluons, known as the quark and gluon sea, but only the valence quarks determine hadrons' quantum numbers.

327 Color charge is the responsible for the SI between quarks and is the symmetry  
 328 ( $SU(3)_C$ ) that defines the formalism to describe SI. There are three colors: red (r),  
 329 blue(b) and green(g) and their corresponding three anti-colors; thus each quark carries  
 330 one color unit while anti-quarks carries one anti-color unit. As said above, quarks are  
 331 not allowed to be isolated due to the color confinement effect, therefore their features  
 332 have been studied indirectly by observing their bound states created when:

- 333     • one quark with a color charge is attracted by an anti-quark with the correspond-  
 334         ing anti-color charge forming a colorless particle called a “meson.”
- 335     • three quarks (anti-quarks) with different color (anti-color) charges are attracted  
 336         among them forming a colorless particle called a “baryon(anti-baryon).”

337 In practice, when a quark is left alone isolated a process called “hadronization” occurs  
 338 where the quark emits gluons (see section 2.2.3) which eventually will generate new  
 339 quark-antiquark pairs and so on; those quarks will recombine to form hadrons that  
 340 will decay into leptons. This proliferation of particles looks like a “jet” coming from  
 341 the isolated quark. More details about the hadronization process and jet structure  
 342 will be given in chapter4.

343 In the first version of the quark model (1964), M. Gell-Mann [12] and G. Zweig  
 344 [13, 14] developed a consistent way to classify hadrons according to their properties.  
 345 Only three quarks (u, d, s) were involved in a scheme in which all baryons have  
 346 baryon number  $B=1$  and therefore quarks have  $B=1/3$ ; non-baryons have  $B=0$ . The  
 347 scheme organizes baryons in a two-dimensional space ( $I_3 - Y$ );  $Y$  (hypercharge) and  $I_3$   
 348 (isospin) are quantum numbers related by the Gell-Mann-Nishijima formula [15, 16]:

$$Q = I_3 + \frac{Y}{2} \quad (2.2)$$

349 where  $Y = B + S + C + T + B'$  are the quantum numbers listed in table 2.4. Baryon  
 350 number is conserved in SI and EI which means that single quarks cannot be created  
 351 but in pairs  $q - \bar{q}$ .

352

353 There are six quark flavors organized in three generations (see table 2.1) following a  
 354 mass hierarchy which, again, implies that higher generations decay to first generation  
 355 quarks.

	Quarks			$T_3$	$Y_W$	Leptons			$T_3$	$Y_W$
Doublets	$(\begin{smallmatrix} u \\ d' \end{smallmatrix})_L$	$(\begin{smallmatrix} c \\ s' \end{smallmatrix})_L$	$(\begin{smallmatrix} t \\ b' \end{smallmatrix})_L$	$(\begin{smallmatrix} 1/2 \\ -1/2 \end{smallmatrix})$	1/3	$(\begin{smallmatrix} \nu_e \\ e \end{smallmatrix})_L$	$(\begin{smallmatrix} \nu_\mu \\ \mu \end{smallmatrix})_L$	$(\begin{smallmatrix} \nu_\tau \\ \tau \end{smallmatrix})_L$	$(\begin{smallmatrix} 1/2 \\ -1/2 \end{smallmatrix})$	-1
Singlets	$u_R$	$c_R$	$t_R$	0	4/3	$\nu_{eR}$	$\nu_{\mu R}$	$\nu_{\tau R}$	0	-2
	$d'_R$	$s'_R$	$b'_R$	0	-2/3	$e_R$	$\mu_R$	$\tau_R$		

**Table 2.5:** Fermion weak isospin and weak hypercharge multiplets. Weak hypercharge is calculated through the Gell-Mann-Nishijima formula 2.2 but using the weak isospin and charge for quarks.

356

357 Isospin doublets of quarks are also defined (see table 2.5) and as for neutrinos, the  
 358 mass eigenstates are not the same as the WI eigenstates which means that members of  
 359 different quark generations are connected by the WI mediator; thus, up-type quarks  
 360 are coupled not to down-type quarks directly but to a superposition of down-type  
 361 quarks ( $q'_d$ ) via WI according to:

$$q'_d = V_{CKM} q_d$$

362

$$\begin{pmatrix} d' \\ s' \\ b' \end{pmatrix} = \begin{pmatrix} V_{ud} & V_{us} & V_{ub} \\ V_{cd} & V_{cs} & V_{cb} \\ V_{td} & V_{ts} & V_{tb} \end{pmatrix} \begin{pmatrix} d \\ s \\ b \end{pmatrix} \quad (2.3)$$

363 where  $V_{CKM}$  is known as Cabibbo-Kobayashi-Maskawa (CKM) mixing matrix [17,18].

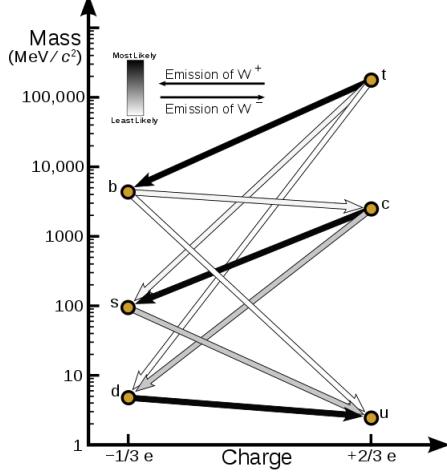


**Figure 2.2:** Transformations between quarks through the exchange of a WI. Higher generations quarks decay to first generation quarks by emitting a W boson. The arrow color indicates the likelihood of the transition according to the grey scale in the top left side which represent the CKM matrix parameters [19].

364 The weak decays of quarks are represented in the diagram of figure 2.2; again the  
 365 CKM matrix plays a central role since it contains the probabilities for the different  
 366 quark decay channels, in particular, note that quark decays are greatly favored be-  
 367 tween generation members.

368

369 CKM matrix is a  $3 \times 3$  unitary matrix parametrized by three mixing angles and  
 370 the *CP-mixing phase*; the latter is the parameter responsible for the Charge-Parity  
 371 symmetry violation (CP-violation) in the SM. The fact that the b quark decays almost  
 372 all the times to a top quark is exploited in this thesis when making the selection of  
 373 the signal events by requiring the presence of a jet tagged as a jet coming from a  
 374 b quark in the final state. The effect of the *CP-mixing phase* on the cross section of  
 375 associated production of Higgs boson and a single top process is also explored in this  
 376 thesis.

377 **2.2.2 Fundamental interactions**

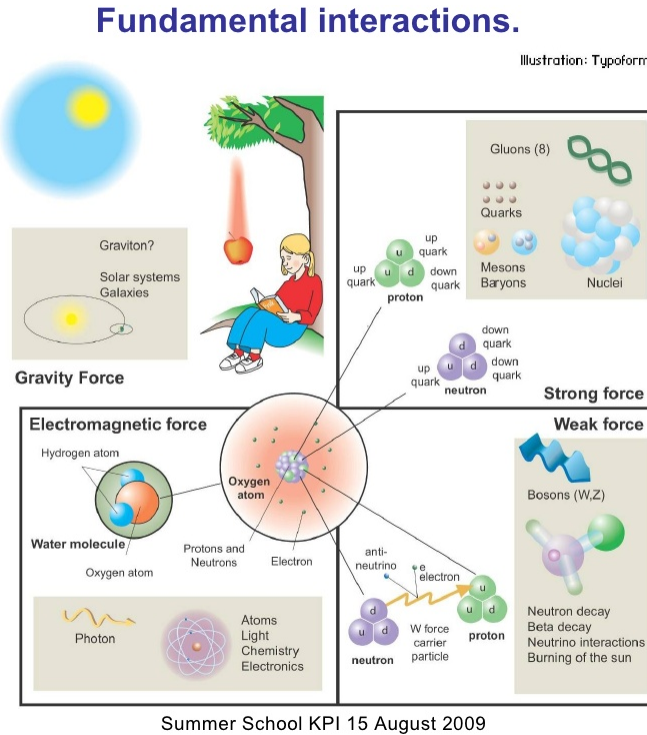


**Figure 2.3:** Fundamental interactions in nature. Despite the many manifestations of forces in nature, we can track all of them back to one of the fundamental interactions. The most common forces are gravity and electromagnetic given that all of us are subject and experience them in everyday life.

378 Even though there are many manifestations of force in nature, like the ones repre-

379 sented in figure 2.3, we can classify all of them into one of four fundamental interac-

380 tions:

- 381 • *Electromagnetic interaction (EI)* affects particles that are “electrically charged,”
- 382 like electrons and protons. It is described by QED combining quantum mechan-
- 383 ics, special relativity and electromagnetism in order to explain how particles
- 384 with electric charge interact through the exchange of photons, therefore, one
- 385 says that “Electromagnetic Force” is mediated by “photons”. Figure 2.4a. shows

386 a graphical representation, known as “feynman diagram”, of electron-electron  
 387 scattering.

- 388 • *Strong interaction (SI)* described by Quantum Chromodynamics (QCD). Hadrons  
 389 like proton and neutron have internal structure given that they are composed  
 390 of two or more valence quarks<sup>5</sup>. Quarks have fractional electric charge which  
 391 means that they are subject to electromagnetic interaction and in the case of the  
 392 proton they should break apart due to electrostatic repulsion; however, quarks  
 393 are held together inside the hadrons against their electrostatic repulsion by the  
 394 “Strong Force” through the exchange of “gluons.” The analog to the electric  
 395 charge is the “color charge”. Electrons and photons are elementary particles  
 396 as quarks but they don’t carry color charge, therefore they are not subject to  
 397 SI. The feynman diagram for gluon exchange between quarks is shown in figure  
 398 2.4b.

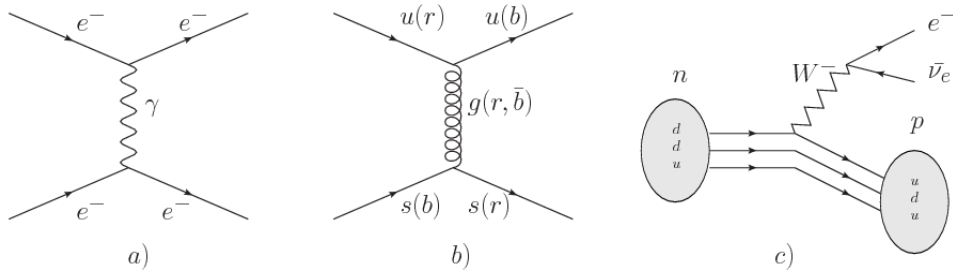


**Figure 2.4:** Feynman diagrams representing the interactions in SM; a) EI: e-e scattering; b) SI: gluon exchange between quarks ; c) WI:  $\beta$ -decay

- 399 • *Weak interaction (WI)* described by the weak theory (WT), is responsible, for  
 400 instance, for the radioactive decay in atoms and proton-proton (pp) fusion  
 401 within the sun. Quarks and leptons are the particles affected by the weak  
 402 interaction; they possess a property called “flavor charge” (see 2.2.1) which can  
 403 be changed by emitting or absorbing one weak force mediator. There are three

<sup>5</sup> particles made of four and five quarks are exotic states not so common.

404 mediators of the “weak force” known as “Z” boson in the case of electrically  
 405 neutral changes and “ $W^\pm$ ” bosons in the case of electrically charged changes.  
 406 The “weak isospin” is the WI analog to electric charge in EI, and color charge  
 407 in SI, and defines how quarks and leptons are affected by the weak force. Figure  
 408 2.4c. shows the feynman diagram of  $\beta$ -decay where a newtron (n) is transformed  
 409 in a proton (p) by emmiting a  $W^-$  particle. Since this thesis is in the frame  
 410 of the electroweak interaction, a more detailed description of it will be given in  
 411 section 2.3

412 • *Gravitational interaction (GI)* described by General Theory of Relativity (GR).  
 413 It is responsible for the structure of galaxies and black holes as well as the  
 414 expansion of the universe. As a classical theory, in the sense that it can be for-  
 415 mulated without even appeal to the concept of quantization, it implies that the  
 416 spacetime is a continuum and predictions can be made without limitation to the  
 417 precision of the measurement tools. The latter represent a direct contradiction  
 418 of the quantum mechanics principles. Gravity is deterministic while quantum  
 419 mechanics is probabilistic; despite that, efforts to develop a quantum theory of  
 420 gravity have predicted the “graviton” as mediator of the Gravitational force<sup>6</sup>.

Interaction	Acts on	Relative strength	Range (m)	Mediators
Electromagnetic (QED)	Electrically charged particles	$10^{-2}$	Infinite	Photon
Strong (QCD)	Quarks and gluons	1	$10^{-15}$	Gluon
Weak (WI)	Leptons and quarks	$10^{-6}$	$10^{-18}$	$W^\pm$ , Z
Gravitational (GI)	Massive particles	$10^{-39}$	Infinite	Graviton

**Table 2.6:** Fundamental interactions features [20].

421

---

<sup>6</sup> Actually a wide variety of theories have been developed in an attempt to describe gravity; some famous examples are string theory and supergravity.

422 Table 2.6 summarizes the main features of the fundamental interactions. The rela-  
 423 tive strength of the fundamental forces reveals the meaning of strong and weak; in  
 424 a context where the relative strength of the SI is 1, the EI is about hundred times  
 425 weaker and WI is about million times weaker than the SI. A good description on  
 426 how the relative strength and range of the fundamental interactions are calculated  
 427 can be found in references [20, 21]. In the everyday life, only EI and GI are explicitly  
 428 experienced due to the range of these interactions; i.e., at the human scale distances  
 429 only EI and GI have appreciable effects, in contrast to SI which at distances greater  
 430 than  $10^{-15}$ m become negligible.

431

432 QED was built successfully on the basis of the classical electrodynamics theory (CED)  
 433 of Maxwell and Lorentz, following theoretical and experimental requirements imposed  
 434 by

- 435     • lorentz invariance: independence on the reference frame.
- 436     • locality: interacting fields are evaluated at the same space-time point to avoid  
     437       action at a distance.
- 438     • renormalizability: physical predictions are finite and well defined
- 439     • particle spectrum, symmetries and conservation laws already known must emerge  
     440       from the theory.
- 441     • gauge invariance.

442 The gauge invariance requirement reflects the fact that the fundamental fields cannot  
 443 be directly measured but associated fields which are the observables. Electric (“E”)  
 444 and magnetic (“B”) fields in CED are associated with the electric scalar potential

445 “V” and the vector potential “A”. In particular,  $\mathbf{E}$  can be obtained by measuring  
 446 the change in the space of the scalar potential ( $\Delta V$ ); however, two scalar potentials  
 447 differing by a constant “f” correspond to the same electric field. The same happens in  
 448 the case of the vector potential “A”; thus, different configurations of the associated  
 449 fields result in the same set of values of the observables. The freedom in choosing  
 450 one particular configuration is known as “gauge freedom”; the transformation law con-  
 451 necting two configurations is known as “gauge transformation” and the fact that the  
 452 observables are not affected by a gauge transformation is called “gauge invariance”.

453

454 When the gauge transformation:

$$\begin{aligned} \mathbf{A} &\rightarrow \mathbf{A} - \Delta f \\ V &\rightarrow V - \frac{\partial f}{\partial t} \end{aligned} \tag{2.4}$$

455 is applied to Maxwell equations, they are still satisfied and the fields remain invariant.  
 456 Thus, CED is invariant under gauge transformations and is called a “gauge theory”.  
 457 The set of all gauge transformations form the “symmetry group” of the theory, which  
 458 according to the group theory, has a set of “group generators”. The number of group  
 459 generators determine the number of “gauge fields” of the theory.

460

461 As mentioned in the first lines of section 2.2, QED has one symmetry group ( $U(1)$ )  
 462 with one group generator (the  $Q$  operator) and one gauge field (the electromagnetic  
 463 field  $A^\mu$ ). In CED there is not a clear definition, beyond the historical convention, of  
 464 which fields are the fundamental and which are the associated, but in QED it is clear  
 465 that the fundamental field is  $A^\mu$ . When a gauge theory is quantized, the gauge field

466 is quantized and its quanta is called “gauge boson”. The word boson characterizes  
 467 particles with integer spin which obvey Bose-einstein statistics.

468

469 As will be detailed in section 2.3, interactions between partcles in a system can be  
 470 obtained by considering first the Lagrangian density of free particles in the system,  
 471 which of course is incomplete because the interaction terms have been left out, and  
 472 demanding global phase transformation invariance. Global phase transformation in-  
 473 variance means that a gauge transformation is performed identically to every point  
 474 in the space<sup>7</sup> and the Lagrangian remains invariant. Then, the global transformation  
 475 is promoted to a local phase transformation (this time the gauge transformation de-  
 476 pends on the position in space) and again invariance is required.

477

478 Due to the space dependence of the local tranformation, the Lagrangian density is  
 479 not invariant anymore. In order to restate the gauge invariance, the gauge covariant  
 480 derivative is introduced in the Lagrangian and with it the gauge field responsible for  
 481 the interaction between particles in the system. The new Lagrangian density is gauge  
 482 invariant, includes the interaction terms needed to account for the interactions and  
 483 provides a way to explain the interaction between particles through the exchange of  
 484 the gauge boson.

485 This recipe was used to build QED and the theories that aim to explain the funda-  
 486 mental interactions.

### 487 **2.2.3 Gauge bosons**

488 The importance of the gauge bosons comes from the fact that they are the force  
 489 mediators or force carriers. The features of the gauge bosons reflect those of the

---

<sup>7</sup> Here space corresponds to the 4-dimensional space i.e. space-time.

490 fields they represent and they are extracted from the Lagrangian density used to  
 491 describe the interactions. In section 2.3, it will be shown how the gauge bosons of the  
 492 EI and WI emerge from the electroweak Lagrangian. The SI gauge bosons features  
 493 are also extracted from the SI Lagrangian but it is not detailed in this document. The  
 494 main features of the SM gauge bosons will be briefly presented below and summarized  
 495 in table 2.7.

- 496     • **Photon.** EI occurs when the photon couples to (is exchanged between) particles  
     497 carrying electric charge; however, the photon itself does not carry electric charge,  
     498 therefore, there is no coupling between photons. Given that the photon is  
     499 massless the EI is of infinite range, i.e., electrically charged particles interact  
     500 even if they are located far away one from each other; this also implies that  
     501 photons always move with the speed of light.
- 502     • **Gluon.** SI is mediated by gluons which, same as photons, are massless. They  
     503 carry one unit of color charge and one unit of anticolor charge which means that  
     504 gluons couple to other gluons. As a result, the range of the SI is not infinite  
     505 but very short due to the attraction between gluons, giving rise to the “color  
     506 confinement” which explains why color charged particles cannot be isolated but  
     507 live within composited particles, like quarks inside protons.
- 508     • **W, Z.** The WI mediators,  $W^\pm$  and Z, are massive which explains their short-  
     509 range. Given that the WI is the only interaction that can change the flavor  
     510 of the interacting particles, the W boson is the responsible for the nuclear  
     511 transmutation where a neutron is converted in a proton or vice versa with the  
     512 involvement of an electron and a neutrino (see figure 2.4c). The Z boson is the  
     513 responsible of the neutral weak processes like neutrino elastic scattering where

514 no electric charge but momentum transference is involved. WI gauge bosons  
 515 carry isospin charge which makes possible the interaction between them.

Interaction	Mediator	Electric charge (e)	Color charge	Weak Isospin	mass (GeV/c <sup>2</sup> )
Electromagnetic	Photon ( $\gamma$ )	0	No	0	0
Strong	Gluon (g)	0	Yes -octet	No	0
Weak	$W^\pm$ Z	$\pm 1$ 0	No No	$\pm 1$ 0	$80.385 \pm 0.015$ $91.188 \pm 0.002$

**Table 2.7:** SM gauge bosons main features [9].

516

## 517 **2.3 Electroweak unification and the Higgs 518 mechanism**

519 Physicists dream of building a theory that contains all the interactions in one single  
 520 interaction, i.e., showing that at some scale in energy all the four fundamental in-  
 521 teractions are unified and only one interaction emerges in a “Theory of everything”.  
 522 The first sign of the feasibility of such unification comes from success in the con-  
 523 struction of the CED. Einstein spent years trying to reach that dream, which by  
 524 1920 only involved electromagnetism and gravity, with no success; however, a new  
 525 partial unification was achieved in the 1960’s, when S.Glashow [22], A.Salam [23] and  
 526 S.Weinberg [24] independently proposed that electromagnetic and weak interactions  
 527 are two manifestations of a more general interaction called “electroweak interaction  
 528 (EWT)”. Both, QCD and EWT, were developed in parallel and following the useful  
 529 prescription provided by QED and the gauge invariance principles.

530

531 The theory of weak interactions was capable of explaining the  $\beta$ -decay and in general  
 532 the processes mediated by  $W^\pm$  bosons. However, there were some processes like the

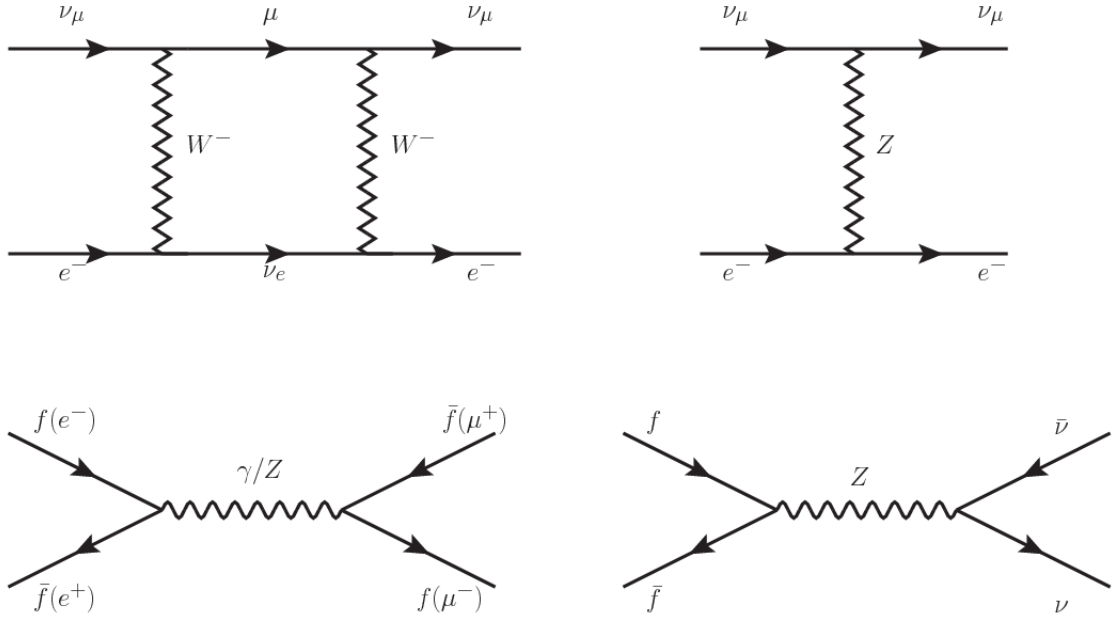


**Figure 2.5:** Top:  $\nu_\mu - e^-$  scattering going through charged currents (left) and neutral currents (right). Bottom: neutral current processes for charged fermions (left) and involving neutrinos (right). While neutral current processes involving only charged fermions can proceed through EI or WI, those involving neutrinos can only proceed via WI.

533 “ $\nu_\mu - e$  scattering” which would require the exchange of two  $W$  bosons (see figure 2.5  
534 top diagrams) giving rise to divergent loop integrals and then non finite predictions.  
535 By including neutral currents involving fermions via the exchange of neutral bosons  
536  $Z$ , those divergences are compensated and the predictions become realistic.

537

538 Neutral weak interaction vertices conserve flavor in the same way as the electromag-  
539 netic vertices do, but additionally, the  $Z$  boson can couple to neutrinos which implies  
540 that processes involving charged fermions can proceed through EI or WI but processes  
541 involving neutrinos can proceed only through WI.

542

543 The prescription to build a gauge theory of the WI consists of proposing a free field  
544 Lagrangian density that includes the particles involved; next, by requesting invari-

545 ance under global phase transformations first and generalizing to local phase trans-  
 546 formations invariance later, the conserved currents are identified and interactions are  
 547 generated by introducing gauge fields. Given that the goal is to include the EI and  
 548 WI in a single theory, the group symmetry considered should be a combination of  
 549  $SU(2)_L$  and  $U(1)_{em}$ , however the latter cannot be used directly because the EI treats  
 550 left and right-handed particles indistinctly in contrast to the former. Fortunately, the  
 551 weak hypercharge, which is a combination of the weak isospin and the electric charge  
 552 (eqn 2.2) is suitable to be used since it is conserved by the EI and WI. Thus, the  
 553 symmetry group to be considered is

$$G \equiv SU(2)_L \otimes U(1)_Y \quad (2.5)$$

554 The following treatment applies to any of the fermion generations, but for simplicity  
 555 the first generation of leptons will be considered [5, 6, 25, 26].

556

557 Given the first generation of leptons

$$\psi_1 = \begin{pmatrix} \nu_e \\ e^- \end{pmatrix}_L, \quad \psi_2 = \nu_{eR}, \quad \psi_3 = e_R^- \quad (2.6)$$

558 the charged fermionic currents are given by

$$J_\mu \equiv J_\mu^+ = \bar{\nu}_{eL} \gamma_\mu e_L, \quad J_\mu^\dagger \equiv J_\mu^- = \bar{e}_L \gamma_\mu \nu_{eL} \quad (2.7)$$

559 and the free Lagrangian is given by

$$\mathcal{L}_0 = \sum_{j=1}^3 i\bar{\psi}_j(x) \gamma^\mu \partial_\mu \psi_j(x). \quad (2.8)$$

560 Mass terms are included directly in the QED and QCD free Lagrangians since they

561 preserve the invariance under the symmetry transformations involved which treat  
 562 left-handed and right-handed similarly, however mass terms of the form

$$m_W^2 W_\mu^\dagger(x) W^\mu(x) + \frac{1}{2} m_Z^2 Z_\mu(x) Z^\mu(x) - m_e \bar{\psi}_e(x) \psi_e(x) \quad (2.9)$$

563 which represent the mass of  $W^\pm$ , Z and electrons, are not invariant under G trans-  
 564 formations, therefore the gauge fields described by the EWI are in principle massless.

565

566 Experiments have shown that the gauge fields are not massless; however, they have  
 567 to acquire mass through a mechanism compatible with the gauge invariance; that  
 568 mechanism is known as the “Higgs mechanism” and will be considered later in this  
 569 section. The global transformations in the combined symmetry group G can be  
 570 written as

$$\begin{aligned} \psi_1(x) &\xrightarrow{G} \psi'_1(x) \equiv U_Y U_L \psi_1(x), \\ \psi_2(x) &\xrightarrow{G} \psi'_2(x) \equiv U_Y \psi_2(x), \\ \psi_3(x) &\xrightarrow{G} \psi'_3(x) \equiv U_Y \psi_3(x) \end{aligned} \quad (2.10)$$

571 where  $U_L$  represent the  $SU(2)_L$  transformation acting only on the weak isospin dou-  
 572 blet and  $U_Y$  represent the  $U(1)_Y$  transformation acting on all the weak isospin mul-  
 573 tiplets. Explicitly

$$U_L \equiv \exp\left(i \frac{\sigma_i}{2} \alpha^i\right), \quad U_Y \equiv \exp(i y_i \beta) \quad (i = 1, 2, 3) \quad (2.11)$$

574 with  $\sigma_i$  the Pauli matrices and  $y_i$  the weak hypercharges. In order to promote the  
 575 transformations from global to local while keeping the invariance, it is required that

576  $\alpha^i = \alpha^i(x)$ ,  $\beta = \beta(x)$  and the replacement of the ordinary derivatives by the covariant  
 577 derivatives

$$\begin{aligned} D_\mu \psi_1(x) &\equiv \left[ \partial_\mu + ig\sigma_i W_\mu^i(x)/2 + ig'y_1 B_\mu(x) \right] \psi_1(x) \\ D_\mu \psi_2(x) &\equiv \left[ \partial_\mu + ig'y_2 B_\mu(x) \right] \psi_2(x) \\ D_\mu \psi_3(x) &\equiv \left[ \partial_\mu + ig'y_3 B_\mu(x) \right] \psi_3(x) \end{aligned} \quad (2.12)$$

578 introducing in this way four gauge fields,  $W_\mu^i(x)$  and  $B_\mu(x)$ , in the process. The  
 579 covariant derivatives (eqn 2.12) are required to transform in the same way as fermion  
 580 fields  $\psi_i(x)$  themselves, therefore, the gauge fields transform as:

$$\begin{aligned} B_\mu(x) &\xrightarrow{G} B'_\mu(x) \equiv B_\mu(x) - \frac{1}{g'} \partial_\mu \beta(x) \\ W_\mu^i(x) &\xrightarrow{G} W_\mu^{i\prime}(x) \equiv W_\mu^i(x) - \frac{i}{g} \partial_\mu \alpha_i(x) - \varepsilon_{ijk} \alpha_i(x) W_\mu^j(x). \end{aligned} \quad (2.13)$$

581 The G invariant version of the Lagrangian density 2.8 can be written as

$$\mathcal{L}_0 = \sum_{j=1}^3 i\bar{\psi}_j(x) \gamma^\mu D_\mu \psi_j(x) \quad (2.14)$$

582 where free massless fermion and gauge fields and fermion-gauge boson interactions  
 583 are included. The EWI Lagrangian density must additionally include kinetic terms  
 584 for the gauge fields ( $\mathcal{L}_G$ ) which are built from the field strengths, according to

$$B_{\mu\nu}(x) \equiv \partial_\mu B_\nu - \partial_\nu B_\mu \quad (2.15)$$

$$W_{\mu\nu}^i(x) \equiv \partial_\mu W_\nu^i(x) - \partial_\nu W_\mu^i(x) - g\varepsilon^{ijk}W_\mu^j W_\nu^k \quad (2.16)$$

585 the last term in eqn. 2.16 is added in order to hold the gauge invariance; therefore,

$$\mathcal{L}_G = -\frac{1}{4}B_{\mu\nu}(x)B^{\mu\nu}(x) - \frac{1}{4}W_{\mu\nu}^i(x)W_i^{\mu\nu}(x) \quad (2.17)$$

586 which contains not only the free gauge fields contributions, but also the gauge fields  
587 self-interactions and interactions among them.

588

589 The three weak isospin conserved currents resulting from the  $SU(2)_L$  symmetry are  
590 given by

$$J_\mu^i(x) = \frac{1}{2}\bar{\psi}_1(x)\gamma_\mu\sigma^i\psi_1(x) \quad (2.18)$$

591 while the weak hypercharge conserved current resulting from the  $U(1)_Y$  symmetry is  
592 given by

$$J_\mu^Y = \sum_{j=1}^3 \bar{\psi}_j(x)\gamma_\mu y_j\psi_j(x) \quad (2.19)$$

593 In order to evaluate the electroweak interactions modeled by an isos triplet field  $W_\mu^i$   
594 which couples to isospin currents  $J_\mu^i$  with strength  $g$  and additionally the singlet  
595 field  $B_\mu$  which couples to the weak hypercharge current  $J_\mu^Y$  with strength  $g'/2$ . The  
596 interaction Lagrangian density to be considered is

$$\mathcal{L}_I = -g J^{i\mu}(x) W_\mu^i(x) - \frac{g'}{2} J^{Y\mu}(x) B_\mu(x) \quad (2.20)$$

597 Note that the weak isospin currents are not the same as the charged fermionic currents  
 598 that were used to describe the WI (eqn 2.7), since the weak isospin eigenstates are  
 599 not the same as the mass eigenstates, but they are closely related

$$J_\mu = \frac{1}{2}(J_\mu^1 + iJ_\mu^2), \quad J_\mu^\dagger = \frac{1}{2}(J_\mu^1 - iJ_\mu^2). \quad (2.21)$$

600 The same happens with the gauge fields  $W_\mu^i$  which are related to the mass eigenstates  
 601  $W^\pm$  by

$$W_\mu^+ = \frac{1}{\sqrt{2}}(W_\mu^1 - iW_\mu^2), \quad W_\mu^- = \frac{1}{\sqrt{2}}(W_\mu^1 + iW_\mu^2). \quad (2.22)$$

602 The fact that there are three weak isospin conserved currents is an indication that in  
 603 addition to the charged fermionic currents, which couple charged to neutral leptons,  
 604 there should be a neutral fermionic current that does not involve electric charge  
 605 exchange; therefore, it couples neutral fermions or fermions of the same electric charge.  
 606 The third weak isospin current contains a term that is similar to the electromagnetic  
 607 current ( $j_\mu^{em}$ ), indicating that there is a relation between them and resembling the  
 608 Gell-Mann-Nishijima formula 2.2 adapted to electroweak interactions

$$Q = T_3 + \frac{Y_W}{2}. \quad (2.23)$$

609 Just as  $Q$  generates the  $U(1)_{em}$  symmetry, the weak hypercharge generates the  $U(1)_Y$   
 610 symmetry as said before. It is possible to write the relationship in terms of the currents  
 611 as

$$j_\mu^{em} = J_\mu^3 + \frac{1}{2} J_\mu^Y. \quad (2.24)$$

612 The neutral gauge fields  $W_\mu^3$  and  $B_\mu$  cannot be directly identified with the  $Z$  and the  
 613 photon fields since the photon interacts similarly with left and right-handed fermions;  
 614 however, they are related through a linear combination given by

$$\begin{aligned} A_\mu &= B_\mu \cos \theta_W + W_\mu^3 \sin \theta_W \\ Z_\mu &= -B_\mu \sin \theta_W + W_\mu^3 \cos \theta_W \end{aligned} \quad (2.25)$$

615 where  $\theta_W$  is known as the “Weinberg angle.” The interaction Lagrangian is now given  
 616 by

$$\mathcal{L}_I = -\frac{g}{\sqrt{2}}(J^\mu W_\mu^+ + J^{\mu\dagger} W_\mu^-) - \left( g \sin \theta_W J_\mu^3 + g' \cos \theta_W \frac{J_\mu^Y}{2} \right) A^\mu - \left( g \cos \theta_W J_\mu^3 - g' \sin \theta_W \frac{J_\mu^Y}{2} \right) Z^\mu \quad (2.26)$$

617 the first term is the weak charged current interaction, while the second term is the  
 618 electromagnetic interaction under the condition

$$g \sin \theta_W = g' \cos \theta_W = e, \quad \frac{g'}{g} = \tan \theta_W \quad (2.27)$$

619 contained in the eqn.2.24; the third term is the neutral weak current.

620

621 Note that the neutral fields transformation given by the eqn. 2.25 can be written in  
 622 terms of the coupling constants  $g$  and  $g'$  as:

$$A_\mu = \frac{g' W_\mu^3 + g B_\mu}{\sqrt{g^2 + g'^2}}, \quad Z_\mu = \frac{g W_\mu^3 - g' B_\mu}{\sqrt{g^2 + g'^2}} \quad (2.28)$$

623 So far, the Lagrangian density describing the non-massive EWI is:

$$\mathcal{L}_{nmEWI} = \mathcal{L}_0 + \mathcal{L}_G \quad (2.29)$$

624 where fermion and gauge fields have been considered massless because their regular  
 625 mass terms are manifestly non invariant under  $G$  transformations; therefore, masses  
 626 have to be generated in a gauge invariant way. The mechanism by which this goal is  
 627 achieved is known as the “Higgs mechanism” and is closely connected to the concept  
 628 of “spontaneous symmetry breaking.”

### 629 2.3.1 Spontaneous symmetry breaking (SSB)

630 Figure 2.6 left shows a steel nail (top) which is subject to an external force; the form  
 631 of the potential energy is also shown (bottom).

632

633 Before reaching the critical force value, the system has rotational symmetry with re-  
 634 spect to the nail axis; however, after the critical force value is reached the nail buckles  
 635 (top right). The form of the potential energy (bottom right) changes, preserving its  
 636 rotational symmetry although its minima does not exhibit that rotational symmetry  
 637 any longer. Right before the nail buckles there is no indication of the direction the  
 638 nail will bend because any of the directions are equivalent, but once the nail bends,  
 639 choosing a direction, an arbitrary minimal energy state (ground state) is selected and  
 640 it does not share the system’s rotational symmetry. This mechanism for reaching an  
 641 asymmetric ground state is known as “*spontaneous symmetry breaking*”.

642 The lesson from this analysis is that the way to introduce the SSB mechanism into a  
 643 system is by adding the appropriate potential to it.

644

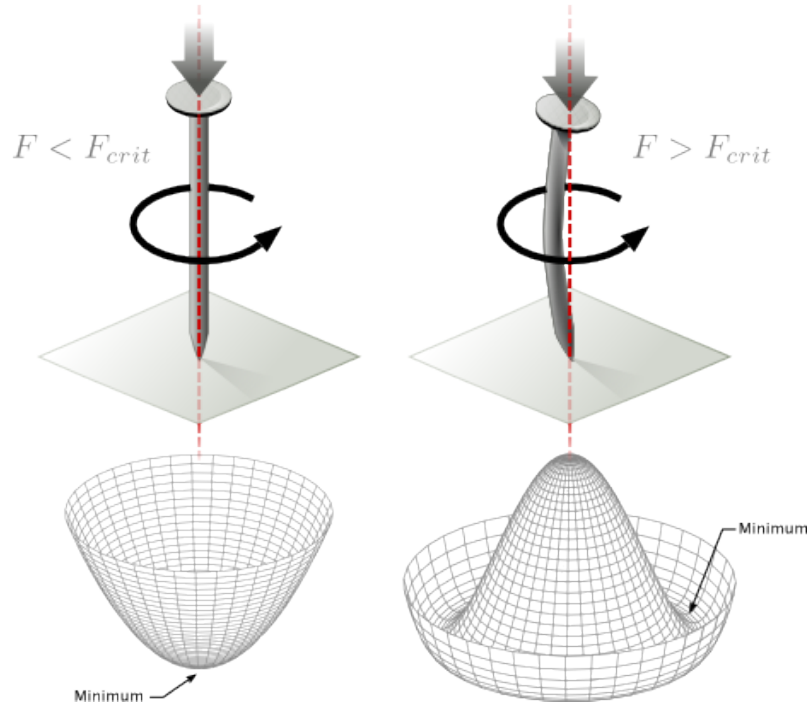


**Figure 2.6:** Spontaneous symmetry breaking mechanism. The steel nail, subject to an external force (top left), has rotational symmetry with respect to its axis. When the external force overcomes a critical value the nail buckles (top right) choosing a minimal energy state (ground state) and thus “*breaking spontaneously the rotational symmetry*”. The potential energy (bottom) changes but holds the rotational symmetry; however, an infinite number of asymmetric ground states are generated and circularly distributed in the bottom of the potential [27].

645 Figure 2.7 shows a plot of the potential  $V(\phi)$  in the case of a scalar field  $\phi$

$$V(\phi) = \mu^2 \phi^\dagger \phi + \lambda (\phi^\dagger \phi)^2 \quad (2.30)$$

646 If  $\mu^2 > 0$  the potential has only one minimum at  $\phi = 0$  and describes a scalar field  
 647 with mass  $\mu$ . If  $\mu^2 < 0$  the potential has a local maximum at  $\phi = 0$  and two minima  
 648 at  $\phi = \pm\sqrt{-\mu^2/\lambda}$  which enables the SSB mechanism to work.

649

650 In the case of a complex scalar field  $\phi(x)$

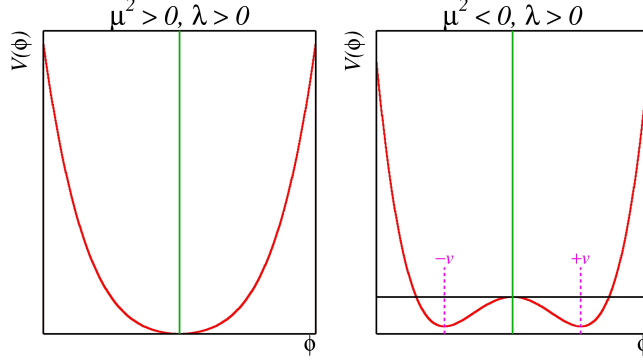


**Figure 2.7:** Shape of the potential  $V(\phi)$  for  $\lambda > 0$  and:  $\mu^2 > 0$  (left) and  $\mu^2 < 0$  (right). The case  $\mu^2 < 0$  corresponds to the potential suitable for introducing the SSB mechanism by choosing one of the two ground states which are connected via reflection symmetry. [27].

$$\phi(x) = \frac{1}{\sqrt{2}}(\phi_1 + i\phi_2) \quad (2.31)$$

651 the Lagrangian (invariant under global  $U(1)$  transformations) is given by

$$\mathcal{L} = (\partial_\mu \phi)^\dagger (\partial^\mu \phi) - V(\phi), \quad V(\phi) = \mu^2 \phi^\dagger \phi + \lambda (\phi^\dagger \phi)^2 \quad (2.32)$$

652 where an appropriate potential has been added in order to introduce the SSB.

653

654 As seen in figure 2.8, the potential has now an infinite number of minima circularly  
 655 distributed along the  $\xi$ -direction which makes possible the occurrence of the SSB by  
 656 choosing an arbitrary ground state; for instance,  $\xi = 0$ , i.e.  $\phi_1 = v, \phi_2 = 0$

$$\phi_0 = \frac{v}{\sqrt{2}} \exp(i\xi) \xrightarrow{\text{SSB}} \phi_0 = \frac{v}{\sqrt{2}} \quad (2.33)$$

657 As usual, excitations over the ground state are studied by making an expansion about

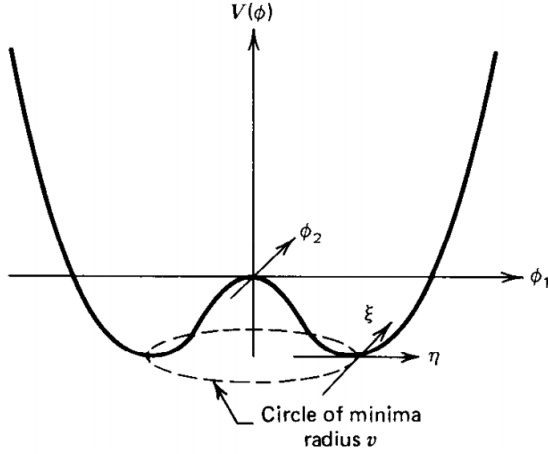


**Figure 2.8:** Potential for complex scalar field. There is a circle of minima of radius  $v$  along the  $\xi$ -direction [6].

658 it; thus, the excitation can be parametrized as:

$$\phi(x) = \frac{1}{\sqrt{2}}(v + \eta(x) + i\xi(x)) \quad (2.34)$$

659 which when substituted into eqn. 2.32 produces a Lagrangian in terms of the new  
660 fields  $\eta$  and  $\xi$

$$\mathcal{L}' = \frac{1}{2}(\partial_\mu \xi)^2 + \frac{1}{2}(\partial_\mu \eta)^2 + \mu^2 \eta^2 - V(\phi_0) - \lambda v \eta (\eta^2 + \xi^2) - \frac{\lambda}{4}(\eta^2 + \xi^2)^2 \quad (2.35)$$

661 where the last two terms represent the interactions and self-interaction between the  
662 two fields  $\eta$  and  $\xi$ . The particular feature of the SSB mechanism is revealed when  
663 looking to the first three terms of  $\mathcal{L}'$ . Before the SSB, only the massless  $\phi$  field is  
664 present in the system; after the SSB there are two fields of which the  $\eta$ -field has  
665 acquired mass  $m_\eta = \sqrt{-2\mu^2}$  while the  $\xi$ -field is still massless (see figure 2.9).

666

667 Thus, the SSB mechanism serves as a method to generate mass but as a side effect a

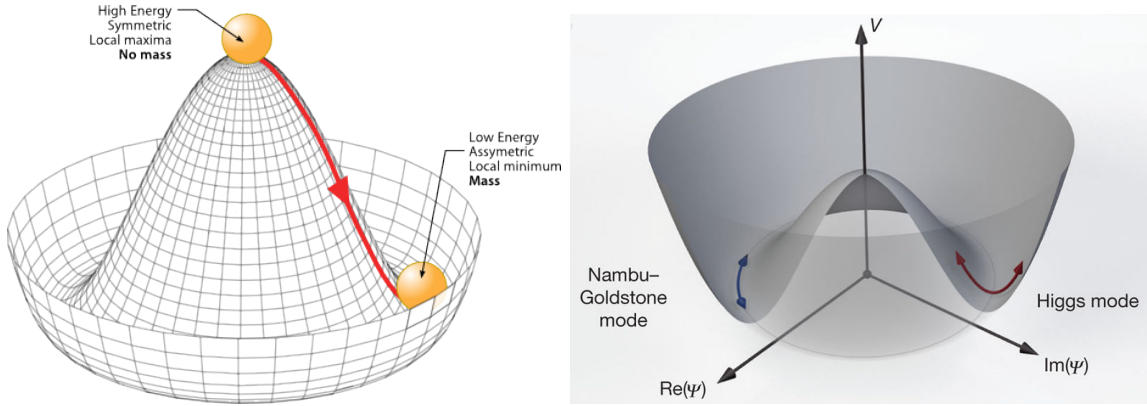


**Figure 2.9:** SSB mechanism for a complex scalar field [27, 28].

668 *massless field is introduced in the system.* This fact is known as the Goldstone theorem  
 669 and states that a massless scalar field appears in the system for each continuous  
 670 symmetry spontaneously broken. Another version of the Goldstone theorem states  
 671 that “*if a Lagrangian is invariant under a continuous symmetry group  $G$ , but the*  
 672 *vacuum is only invariant under a subgroup  $H \subset G$ , then there must exist as many*  
 673 *massless spin-0 particles (Nambu-Goldstone bosons) as broken generators.*” [26] The  
 674 Nambu-Goldstone boson can be understood considering that the potential in the  $\xi$ -  
 675 direction is flat so excitations in that direction are not energy consuming and thus  
 676 represent a massless state.

### 677 2.3.2 Higgs mechanism

678 When the SSB mechanism is introduced in the formulation of the EWI in an attempt  
 679 to generate the mass of the so far massless gauge bosons and fermions, an interesting  
 680 effect is revealed. In order to keep the  $G$  symmetry group invariance and generate  
 681 the mass of the EW gauge bosons, a  $G$  invariant Lagrangian density ( $\mathcal{L}_S$ ) has to be  
 682 added to the non massive EWI Lagrangian (eqn. 2.29)

$$\mathcal{L}_S = (D_\mu \phi)^\dagger (D^\mu \phi) - \mu^2 \phi^\dagger \phi - \lambda (\phi^\dagger \phi)^2, \quad \lambda > 0, \mu^2 < 0 \quad (2.36)$$

$$D_\mu \phi = \left( i\partial_\mu - g \frac{\sigma_i}{2} W_\mu^i - g' \frac{Y}{2} B_\mu \right) \phi \quad (2.37)$$

683  $\phi$  has to be an isospin doublet of complex scalar fields so it preserves the G invariance;  
 684 thus  $\phi$  can be defined as:

$$\phi = \begin{pmatrix} \phi^+ \\ \phi^0 \end{pmatrix} \equiv \frac{1}{\sqrt{2}} \begin{pmatrix} \phi_1 + i\phi_2 \\ \phi_3 + i\phi_4 \end{pmatrix}. \quad (2.38)$$

685 The minima of the potential are defined by

$$\phi^\dagger \phi = \frac{1}{2} (\phi_1^2 + \phi_2^2 + \phi_3^2 + \phi_4^2) = -\frac{\mu^2}{2\lambda}. \quad (2.39)$$

686 The choice of the ground state is critical. By choosing a ground state, invariant under  
 687  $U(1)_{em}$  gauge symmetry, the photon will remain massless and the  $W^\pm$  and  $Z$  bosons  
 688 masses will be generated which is exactly what is needed. In that sense, the best  
 689 choice corresponds to a weak isospin doublet with  $T_3 = -1/2$ ,  $Y_W = 1$  and  $Q = 0$   
 690 which defines a ground state with  $\phi_1 = \phi_2 = \phi_4$  and  $\phi_3 = v$ :

$$\phi_0 \equiv \frac{1}{\sqrt{2}} \begin{pmatrix} 0 \\ v \end{pmatrix}, \quad v^2 \equiv -\frac{\mu^2}{\lambda}. \quad (2.40)$$

691 where the vacuum expectation value  $v$  is fixed by the Fermi coupling  $G_F$  according  
 692 to  $v = (\sqrt{2}G_F)^{1/2} \approx 246$  GeV.

693

694 The G symmetry has been broken and three Nambu-Goldstone bosons will appear.

695 The next step is to expand  $\phi$  about the chosen ground state as:

$$\phi(x) = \frac{1}{\sqrt{2}} \exp\left(\frac{i}{v} \sigma_i \theta^i(x)\right) \begin{pmatrix} 0 \\ v + H(x) \end{pmatrix} \approx \frac{1}{\sqrt{2}} \begin{pmatrix} \theta_1(x) + i\theta_2(x) \\ v + H(x) - i\theta_3(x) \end{pmatrix} \quad (2.41)$$

696 to describe fluctuations from the ground state  $\phi_0$ . The fields  $\theta_i(x)$  represent the  
 697 Nambu-Goldstone bosons while  $H(x)$  is known as “higgs field.” The fundamental  
 698 feature of the parametrization used is that the dependence on the  $\theta_i(x)$  fields is  
 699 factored out in a global phase that can be eliminated by taking the physical “unitary  
 700 gauge”  $\theta_i(x) = 0$ . Therefore the expansion about the ground state is given by:

$$\phi(x) \frac{1}{\sqrt{2}} \begin{pmatrix} 0 \\ v + H(x) \end{pmatrix} \quad (2.42)$$

701 which when substituted into  $\mathcal{L}_S$  (eqn. 2.36) results in a Lagrangian containing the now  
 702 massive three gauge bosons  $W^\pm, Z$ , one massless gauge boson (photon) and the new  
 703 Higgs field ( $H$ ). The three degrees of freedom corresponding to the Nambu-Goldstone  
 704 bosons are now integrated into the massive gauge bosons as their longitudinal po-  
 705 larizations which were not available when they were massless particles. The effect  
 706 by which vector boson fields acquire mass after an spontaneous symmetry breaking,  
 707 but without an explicit gauge invariance breaking is known as the “*Higgs mechanism*”.

708

709 The mechanism was proposed by three independent groups: F.Englert and R.Brout  
 710 in August 1964 [29], P.Higgs in October 1964 [30] and G.Guralnik, C.Hagen and  
 711 T.Kibble in November 1964 [31]; however, its importance was not realized until  
 712 S.Glashow [22], A.Salam [23] and S.Weinberg [24], independently, proposed that elec-  
 713 tromagnetic and weak interactions are two manifestations of a more general interac-  
 714 tion called “electroweak interaction” in 1967.

### 715 2.3.3 Masses of the gauge bosons

716 The mass of the gauge bosons is extracted by evaluating the kinetic part of Lagrangian

717  $\mathcal{L}_S$  in the ground state (known also as the vacuum expectation value), i.e.,

$$\left| \left( \partial_\mu - ig \frac{\sigma_i}{2} W_\mu^i - i \frac{g'}{2} B_\mu \right) \phi_0 \right|^2 = \left( \frac{1}{2} v g \right)^2 W_\mu^+ W^{-\mu} + \frac{1}{8} v^2 (W_\mu^3, B_\mu) \begin{pmatrix} g^2 & -gg' \\ -gg' & g'^2 \end{pmatrix} \begin{pmatrix} W^{3\mu} \\ B^\mu \end{pmatrix} \quad (2.43)$$

718 comparing with the typical mass term for a charged boson  $M_W^2 W^+ W^-$

$$M_W = \frac{1}{2} v g. \quad (2.44)$$

The second term in the right side of the eqn.2.43 comprises the masses of the neutral bosons, but it needs to be written in terms of the gauge fields  $Z_\mu$  and  $A_\mu$  in order to be compared to the typical mass terms for neutral bosons, therefore using eqn. 2.28

$$\begin{aligned} \frac{1}{8} v^2 [g^2 (W_\mu^3)^2 - 2gg' W_\mu^3 B^\mu + g'^2 B_\mu^2] &= \frac{1}{8} v^2 [g W_\mu^3 - g' B_\mu]^2 + 0[g' W_\mu^3 + g B_\mu]^2 \quad (2.45) \\ &= \frac{1}{8} v^2 [\sqrt{g^2 + g'^2} Z_\mu]^2 + 0[\sqrt{g^2 + g'^2} A_\mu]^2 \end{aligned}$$

719 and then

$$M_Z = \frac{1}{2} v \sqrt{g^2 + g'^2}, \quad M_A = 0 \quad (2.46)$$

720 **2.3.4 Masses of the fermions**

721 The lepton mass terms can be generated by introducing a gauge invariant Lagrangian  
 722 term describing the Yukawa coupling between the lepton field and the Higgs field

$$\mathcal{L}_{Yl} = -G_l \left[ (\bar{\nu}_l, \bar{l})_L \begin{pmatrix} \phi^+ \\ \phi^0 \end{pmatrix} l_R + \bar{l}_R (\phi^-, \bar{\phi}^0) \begin{pmatrix} \nu_l \\ l \end{pmatrix} \right], \quad l = e, \mu, \tau. \quad (2.47)$$

723 After the SSB and replacing the usual field expansion about the ground state (eqn.2.40)  
 724 into  $\mathcal{L}_{Yl}$ , the mass term arises

$$\mathcal{L}_{Yl} = -m_l (\bar{l}_L l_R + \bar{l}_R l_L) - \frac{m_l}{v} (\bar{l}_L l_R + \bar{l}_R l_L) H = -m_l \bar{l} l \left( 1 + \frac{H}{v} \right) \quad (2.48)$$

725

$$m_l = \frac{G_l}{\sqrt{2}} v \quad (2.49)$$

726 where the additional term represents the lepton-Higgs interaction. The quark masses  
 727 are generated in a similar way as lepton masses but for the upper member of the  
 728 quark doublet a different Higgs doublet is needed:

$$\phi_c = -i\sigma_2 \phi^* = \begin{pmatrix} -\bar{\phi}^0 \\ \phi^- \end{pmatrix}. \quad (2.50)$$

729 Additionally, given that the quark isospin doublets are not constructed in terms of  
 730 the mass eigenstates but in terms of the flavor eigenstates, as shown in table2.5, the  
 731 coupling parameters will be related to the CKM matrix elements; thus the quark  
 732 Lagrangian is given by:

$$\mathcal{L}_{Yq} = -G_d^{i,j} (\bar{u}_i, \bar{d}'_i)_L \begin{pmatrix} \phi^+ \\ \phi^0 \end{pmatrix} d_{jR} - G_u^{i,j} (\bar{u}_i, \bar{d}'_i)_L \begin{pmatrix} -\bar{\phi}^0 \\ \phi^- \end{pmatrix} u_{jR} + h.c. \quad (2.51)$$

733 with  $i,j=1,2,3$ . After SSB and expansion about the ground state, the diagonal form

734 of  $\mathcal{L}_{Yq}$  is:

$$\mathcal{L}_{Yq} = -m_d^i \bar{d}_i d_i \left(1 + \frac{H}{v}\right) - m_u^i \bar{u}_i u_i \left(1 + \frac{H}{v}\right) \quad (2.52)$$

735 Fermion masses depend on arbitrary couplings  $G_l$  and  $G_{u,d}$  and are not predicted by  
736 the theory.

### 737 2.3.5 The Higgs field

738 After the characterization of the fermions and gauge bosons as well as their interac-  
739 tions, it is necessary to characterize the Higgs field itself. The Lagrangian  $\mathcal{L}_S$  in eqn.  
740 2.36 written in terms of the gauge bosons is given by

$$\mathcal{L}_S = \frac{1}{4} \lambda v^4 + \mathcal{L}_H + \mathcal{L}_{HV} \quad (2.53)$$

741

$$\mathcal{L}_H = \frac{1}{2} \partial_\mu H \partial^\mu H - \frac{1}{2} m_H^2 H^2 - \frac{1}{2v} m_H^2 H^3 - \frac{1}{8v^2} m_H^2 H^4 \quad (2.54)$$

742

$$\mathcal{L}_{HV} = m_H^2 W_\mu^+ W^{\mu-} \left(1 + \frac{2}{v} H + \frac{2}{v^2} H^2\right) + \frac{1}{2} m_Z^2 Z_\mu Z^\mu \left(1 + \frac{2}{v} H + \frac{2}{v^2} H^2\right) \quad (2.55)$$

743 The mass of the Higgs boson is deduced as usual from the mass term in the Lagrangian  
744 resulting in:

$$m_H = \sqrt{-2\mu^2} = \sqrt{2\lambda}v \quad (2.56)$$

745 however, it is not predicted by the theory either. The experimental efforts to find  
746 the Higgs boson, carried out by the “Compact Muon Solenoid (CMS)” experiment  
747 and the “A Toroidal LHC AppartuS (ATLAS)” experiments at the “Large Hadron  
748 Collider(LHC)”, gave great results by July of 2012 when the discovery of a new  
749 particle compatible with the Higgs boson predicted by the electroweak theory [32, 33]  
750 was announced. Although at the announcement time there were some reservations  
751 about calling the new particle the “Higgs boson”, today this name is widely accepted.

752 The Higgs mass measurement, reported by both experiments [34], is in table 2.8.

Property	Value
Electric charge	0
Colour charge	0
Spin	0
Weak isospin	-1/2
Weak hypercharge	1
Parity	1
Mass ( $\text{GeV}/c^2$ )	$125.09 \pm 0.21 \text{ (stat.)} \pm 0.11 \text{ (syst.)}$

**Table 2.8:** Higgs boson properties. Higgs mass is not predicted by the theory and the value here corresponds to the experimental measurement.

753

### 754 2.3.6 Production of Higgs bosons at LHC

755 At LHC, Higgs boson is produced as a result of the collision of two counter-rotating  
 756 protons beams. A detailed description of the LHC machine will be presented in  
 757 chapter 3. “The total cross section” is a parameter that quantifies the number of pp  
 758 collisions that happen when a number of protons are fired at each other. Different  
 759 results can be obtained after a pp collision and for each one the “cross section” is  
 760 defined as the number of pp collisions that conclude in that particular result with  
 761 respect to the number of protons fired at each other.

762 Protons are composed of quarks and these quarks are bound by gluons; however,  
 763 what is commonly called the quark content of the proton makes reference to the  
 764 valence quarks. A sea of quarks and gluons is also present inside the proton as repre-  
 765 sented in figure 2.10. In a proton-proton (pp) collision, the constituents (quarks and  
 766 gluons) are those who collide. The pp cross section depends on the momentum of  
 767 the colliding particles, reason for which it is needed to know how the momentum is  
 768 distributed inside the proton. Quarks and gluons are known as partons and the func-  
 769 tions that describe how the proton momentum is distributed among partons inside it

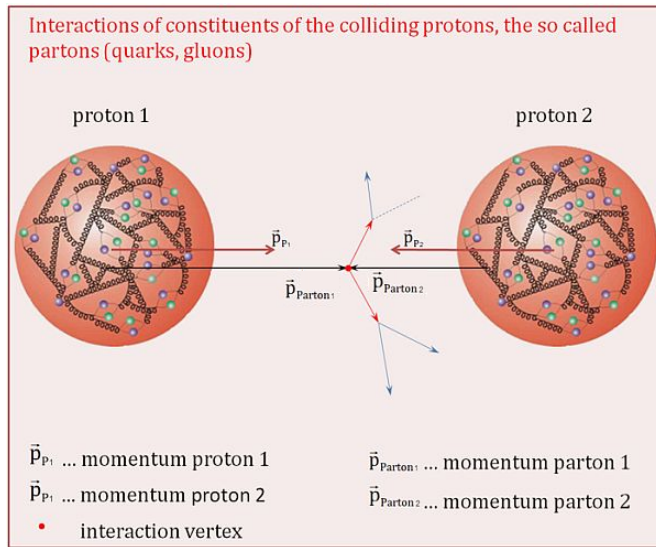


**Figure 2.10:** Proton-proton collision. Protons are composed of 3 valence quarks, a sea of quarks and gluons; therefore in a proton-proton collision, quarks and gluons are those who collide. [35].

are called “parton distribution functions (PDFs)”; PDFs are determined from experimental data obtained in experiments where the internal structure of hadrons is tested.

772

In addition, in physics, a common approach to study complex systems consists in starting with a simpler version of them, for which a well known description is available, and add an additional “perturbation” which represents a small deviation from the known behavior. If the perturbation is small enough, the physical quantities associated with the perturbed system are expressed as a series of corrections to those of the simpler system; therefore, the more terms are considered in the series (the higher order in the perturbation series), the more precise is the the description of the complex system.

781

782 This thesis explores the Higgs production at LHC; therefore the overview presented  
783 here will be oriented specifically to the production mechanisms after pp collisions at

784 LHC.

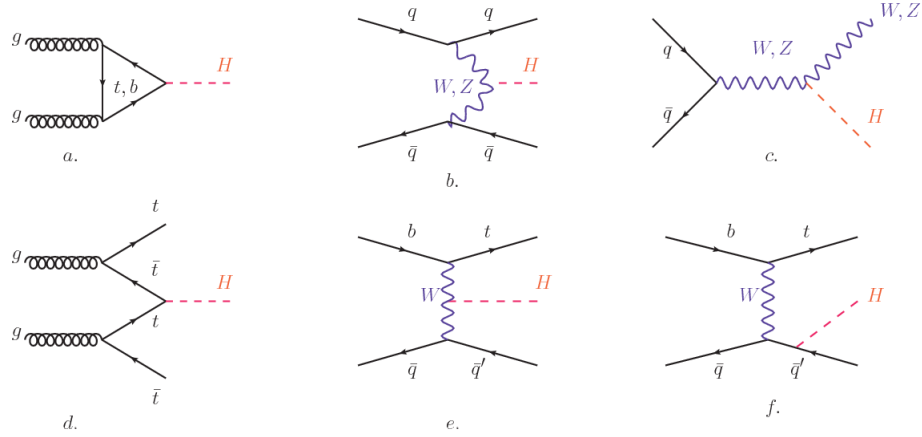


**Figure 2.11:** Main Higgs boson production mechanism Feynman diagrams. a. gluon-gluon fusion, b. vector boson fusion (VBF), c. Higgs-strahlung, d. Associated production with a top or bottom quark pair, e-f. associated production with a single top quark.

785 Figure 2.11 shows the Feynman diagrams for the leading order (first order) Higgs  
 786 production processes at LHC, while the cross section for Higgs production as a func-  
 787 tion of the center of mass-energy ( $\sqrt{s}$ ) for pp collisions is showed in figure 2.12 left.  
 788 The tags NLO (next to leading order), NNLO (next to next to leading order) and  
 789 N3LO (next to next to next to leading order) make reference to the order at which  
 790 the perturbation series have been considered.

791 As shown in eqns 2.47, 2.51 and 2.55, the strength of the Higgs-fermion interaction  
 792 is proportional to the fermion mass while the strength of the Higgs-gauge boson  
 793 interaction is proportional to the square of the gauge boson mass, which implies  
 794 that the Higgs production and decay mechanisms are dominated by couplings  $H -$   
 795  $(W, Z, t, b, \tau)$ .

796 The main production mechanism is the gluon fusion (figure 2.11a and  $pp \rightarrow H$  in figure  
 797 2.12) given that gluons carry the highest fraction of momentum of the protons in pp  
 798 colliders. Since the Higgs boson does not couple to gluons, the mechanism proceeds  
 799 through the exchange of a virtual top-quark loop given that for it the coupling is

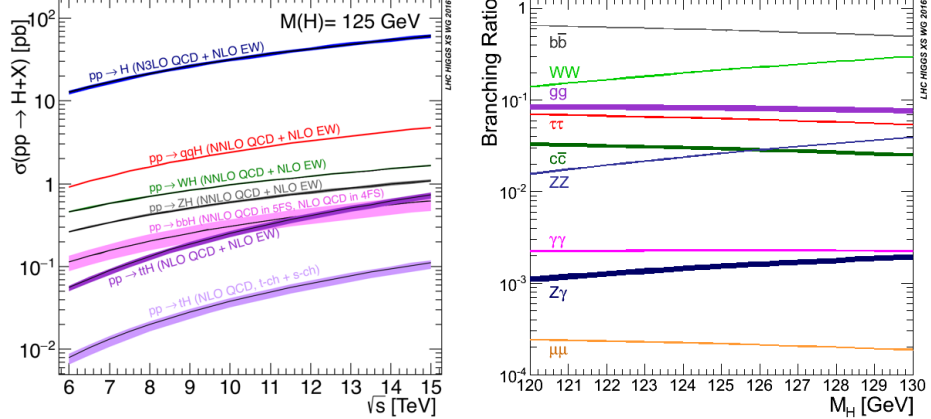


**Figure 2.12:** Higgs boson production cross sections (left) and decay branching ratios (right) for the main mechanisms. The VBF is indicated as  $qqH$  [36].

the biggest. Note that in this process, the Higgs boson is produced alone, which makes this mechanism experimentally clean when combined with the two-photon or the four-lepton decay channels (see section 2.3.7).  
 Vector boson fusion (figure 2.11b and  $pp \rightarrow qqH$  in figure 2.12) has the second largest production cross section. The scattering of two fermions is mediated by a weak gauge boson which later emits a Higgs boson. In the final state, the two fermions tend to be located in a particular region of the detector which is used as a signature when analyzing the datasets provided by the experiments. More details about how to identify events of interest in an analysis will be given in chapter 6.  
 The next production mechanism is Higgs-strahlung (figure 2.11c and  $pp \rightarrow WH, pp \rightarrow ZH$  in figure 2.12) where two fermions annihilate to form a weak gauge boson. If the initial fermions have enough energy, the emergent boson eventually will emit a Higgs boson.  
 The associated production with a top or bottom quark pair and the associated production with a single top quark (figure 2.11d-f and  $pp \rightarrow bbH, pp \rightarrow t\bar{t}H, pp \rightarrow tH$  in figure 2.12) have a smaller cross section than the main three mechanisms above,

816 but they provide a good opportunity to test the Higgs-top coupling. The analysis  
 817 reported in this thesis is developed using these production mechanisms. A detailed  
 818 description of the  $tH$  mechanism will be given in section 2.4.

### 819 2.3.7 Higgs boson decay channels

820 When a particle can decay through several modes, also known as channels, the  
 821 probability of decaying through a given channel is quantified by the “branching ratio  
 822 (BR)” of the decay channel; thus, the BR is defined as the ratio of number of decays  
 823 going through that given channel to the total number of decays. In regard to the  
 824 Higgs boson decay, the BR can be predicted with accuracy once the Higgs mass is  
 825 known [37, 38]. In figure 2.12 right, a plot of the BR as a function of the Higgs mass  
 826 is presented. The largest predicted BR corresponds to the  $b\bar{b}$  pair decay channel (see  
 827 table 2.9).

Decay channel	Branching ratio	Rel. uncertainty
$H \rightarrow b\bar{b}$	$5.84 \times 10^{-1}$	$+3.2\% - 3.3\%$
$H \rightarrow W^+W^-$	$2.14 \times 10^{-1}$	$+4.3\% - 4.2\%$
$H \rightarrow \tau^+\tau^-$	$6.27 \times 10^{-2}$	$+5.7\% - 5.7\%$
$H \rightarrow ZZ$	$2.62 \times 10^{-2}$	$+4.3\% - 4.1\%$
$H \rightarrow \gamma\gamma$	$2.27 \times 10^{-3}$	$+5.0\% - 4.9\%$
$H \rightarrow Z\gamma$	$1.53 \times 10^{-3}$	$+9.0\% - 8.9\%$
$H \rightarrow \mu^+\mu^-$	$2.18 \times 10^{-4}$	$+6.0\% - 5.9\%$

**Table 2.9:** Predicted branching ratios and the relative uncertainty for a SM Higgs boson with  $m_H = 125 GeV/c^2$ . [9]

829 **2.4 Associated production of a Higgs boson and a  
830 single Top quark.**

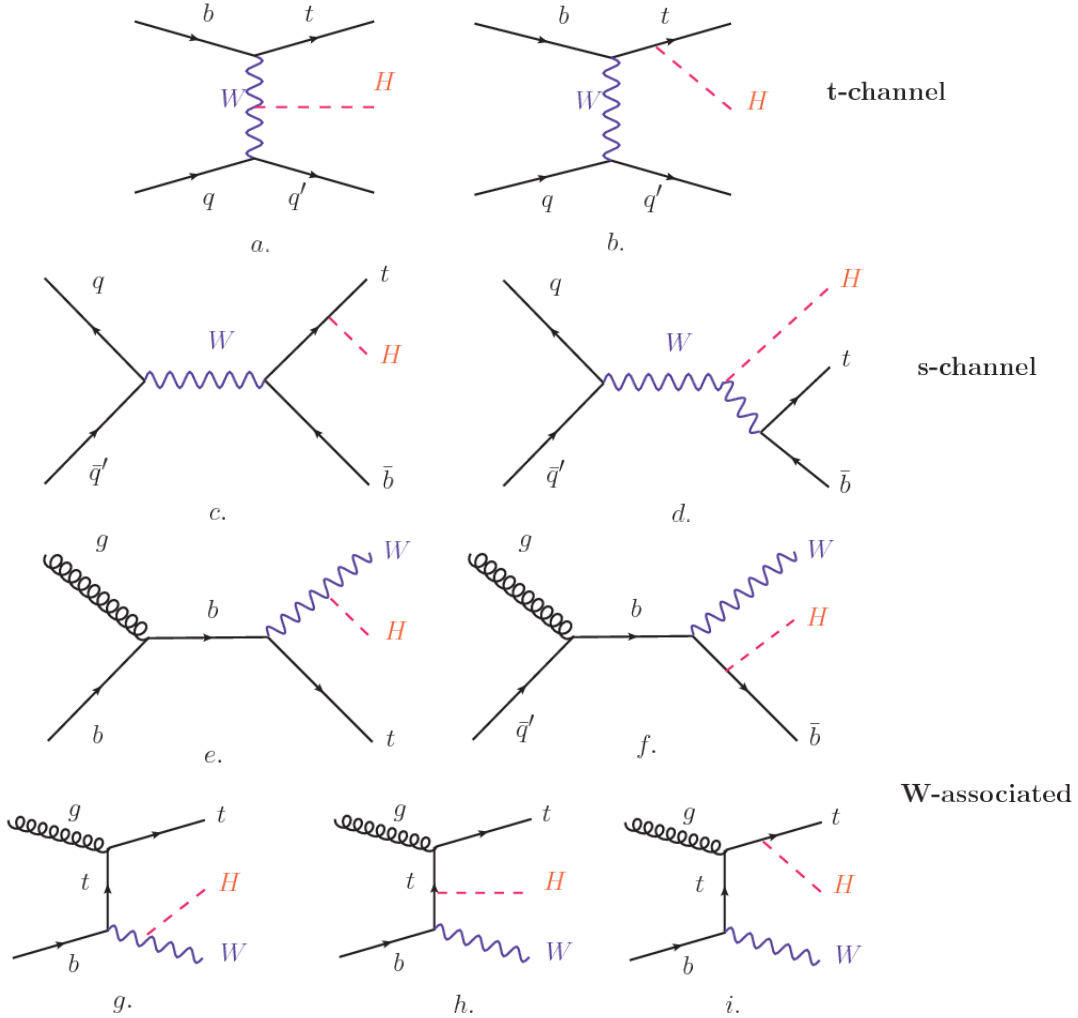


**Figure 2.13:** Associated Higgs boson production mechanism Feynman diagrams. a.,b. t-channel (tHq), c.,d. s-channel (tHb), e-i. W-associated.

831 Associated production of Higgs boson has been extensively studied [39–43]. While  
832 measurements of the main Higgs production mechanisms rates are sensitive to the  
833 strength of the Higgs coupling to W boson or top quark, they are not sensitive to the  
834 relative sign between the two couplings. In this thesis, the Higgs boson production

mechanism explored is the associated production with a single top quark ( $tH$ ) which offers sensitiveness to the relative sign of the Higgs couplings to W boson and to top quark. The description given here is based on the reference [41]

838

839 A process where two incoming particles interact and produce a final state with two  
 840 particles can proceed in three ways also called channels (see, for instance, figure 2.13  
 841 ommiting the red line). The t-channel represents processes where an intermediate  
 842 particle is emitted by one of the incoming particles and absorbed by the other. The  
 843 s-channel represents processes where the two incoming particles merge into an inter-  
 844 mediate particle which eventually will split into the particles in the final state. The  
 845 third channel, u-channel, is similar to the t-channel but the two outgoing particles  
 846 interchange their roles.

847

848 The  $tH$ production, where Higgs boson can be radiated either from the top quark  
 849 or from the W boson, is represented by the leading order Feynman diagrams in  
 850 figure ???. The cross section for the  $tH$ process is calculated, as usual, summing over  
 851 the contributions from the different feynman diagrams; therefore it depends on the  
 852 interference between the contributions. In the SM, the interference for t-channel ( $tHq$   
 853 process) and W-associated ( $tHW$  process) production is destructive [39] resulting in  
 854 the small cross sections presented in table 2.10.

tH production channel	Cross section (fb)
t-channel ( $pp \rightarrow tHq$ )	$70.79^{+2.99}_{-4.80}$
W-associated ( $pp \rightarrow tHW$ )	$15.61^{+0.83}_{-1.04}$
s-channel( $pp \rightarrow tHb$ )	$2.87^{+0.09}_{-0.08}$

**Table 2.10:** Predicted SM cross sections for  $tH$ production at  $\sqrt{s} = 13$  TeV [44, 45].

855

856 While the s-channel contribution can be neglected, it will be shown that a deviation  
 857 from the SM destructive interference would result in an enhancement of the  $tH$  cross  
 858 section compared to that in SM, which could be used to get information about the  
 859 sign of the Higgs-top coupling [41, 42]. In order to describe  $tH$  production processes,  
 860 Feynman diagram 2.13b will be considered; there, the W boson is radiated by a  
 861 quark in the proton and eventually it will interact with the b quark. In the high  
 862 energy regime, the effective W approximation [46] allows to describe the process as  
 863 the emmision of an approximately on-shell W and its hard scattering with the b  
 864 quark; i.e.  $Wb \rightarrow th$ . The scattering amplitude for the process is given by

$$\mathcal{A} = \frac{g}{\sqrt{2}} \left[ (\kappa_t - \kappa_V) \frac{m_t \sqrt{s}}{m_W v} A \left( \frac{t}{s}, \varphi; \xi_t, \xi_b \right) + \left( \kappa_V \frac{2m_W s}{v} \frac{1}{t} + (2\kappa_t - \kappa_V) \frac{m_t^2}{m_W v} \right) B \left( \frac{t}{s}, \varphi; \xi_t, \xi_b \right) \right], \quad (2.57)$$

865 where  $\kappa_V \equiv g_{HVV}/g_{HVV}^{SM}$  and  $\kappa_t \equiv g_{Ht}/g_{Ht}^{SM} = y_t/y_t^{SM}$  are scaling factors that quan-  
 866 tify possible deviations of the couplings, Higgs-Vector boson (H-W) and Higgs-top  
 867 (H-t) respectively, from the SM couplings;  $s = (p_W + p_b)^2$ ,  $t = (p_W - p_H)^2$ ,  $\varphi$  is the  
 868 Higgs azimuthal angle around the  $z$  axis taken parallel to the direction of motion of  
 869 the incoming W; A and B are funtions describing the weak interaction in terms of  
 870 the chiral states of the quarks  $b$  and  $t$ . Terms that vanish in the high energy limit  
 871 have been neglected as well as the Higgs and  $b$  quark masses<sup>8</sup>.

872

873 The scattering amplitude grows with energy like  $\sqrt{s}$  for  $\kappa_V \neq \kappa_t$ , in contrast to  
 874 the SM ( $\kappa_t = \kappa_V = 1$ ), where the first term in 2.57 cancels out and the amplitude  
 875 is constant for large  $s$ ; therefore, a deviation from the SM predictions represents an  
 876 enhancement in the  $tHq$  cross section. In particular, for a SM H-W coupling and a H-t

---

<sup>8</sup> A detailed explanation of the structure and approximations used to derive  $\mathcal{A}$  can be found in reference [41]

877 coupling of inverted sign with respect to the SM ( $\kappa_V = -\kappa_t = 1$ ) the  $tHq$  cross section  
 878 is enhanced by a factor greater 10 as seen in the figure 2.14 taken from reference [41];  
 879 reference [47] has reported similar enhancement results.

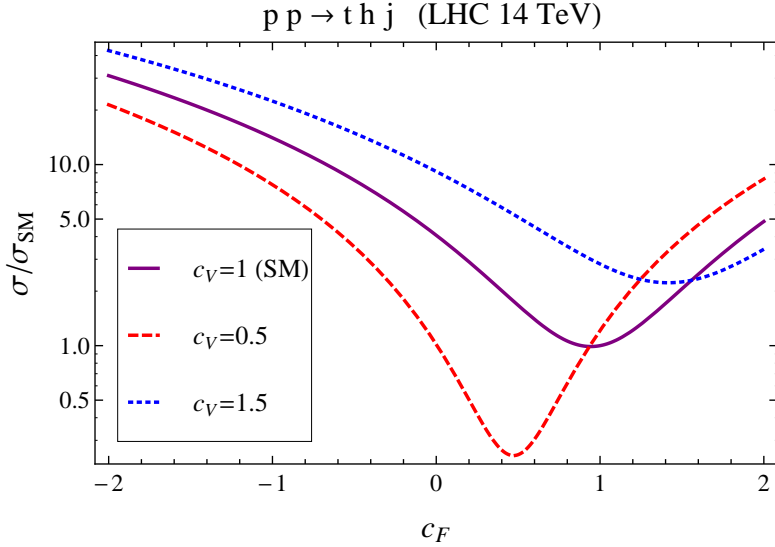


**Figure 2.14:** Cross section for  $tHq$  process as a function of  $\kappa_t$ , normalized to the SM, for three values of  $\kappa_V$ . In the plot  $c_f$  refers to the Higgs-fermion coupling which is dominated by the H-t coupling and represented here by  $\kappa_t$ . Solid, dashed and dotted lines correspond to  $c_V \rightarrow \kappa_V = 1, 0.5, 1.5$  respectively. Note that for the SM ( $\kappa_V = \kappa_t = 1$ ), the destructive effect of the interference is maximal.

880 A similar analysis is valid for the W-associated channel but, in that case, the inter-  
 881 ference is more complicated since there are more than two contributions and an ad-  
 882 ditional interference with the production of Higgs boson and a top pair process( $t\bar{t}H$ ).  
 883 The calculations are made using the so-called Diagram Removal (DR) technique where  
 884 interfering diagrams are removed (or added) from the calculations in order to evaluate  
 885 the impact of the removed contributions. DR1 was defined to neglect  $t\bar{t}H$  interference  
 886 while DR2 was defined to take  $t\bar{t}H$  interference into account [48]. As shown in figure  
 887 2.15, the  $tHW$  cross section is enhanced from about 15 fb (SM:  $\kappa_{Htt} = 1$ ) to about  
 888 150 fb ( $\kappa_{Htt} = -1$ ). Differences between curves for DR1 and DR2 help to gauge the  
 889 impact of the interference with  $t\bar{t}H$ .

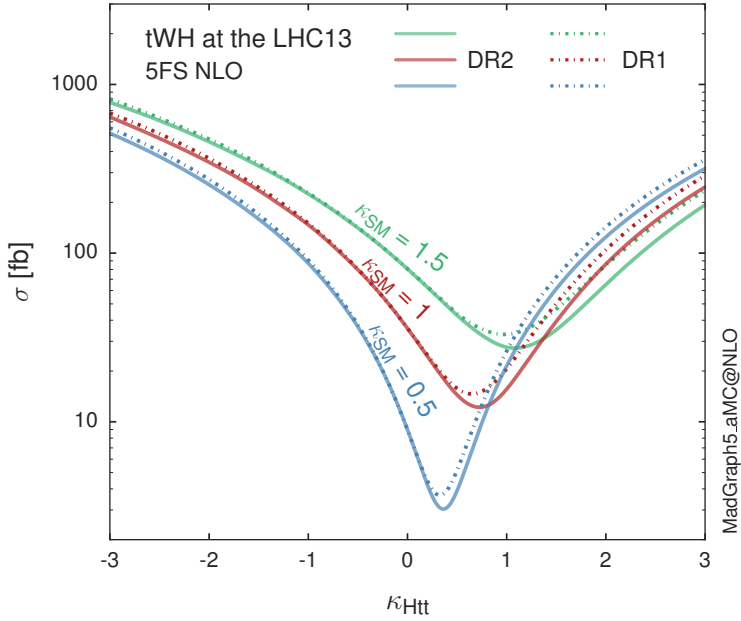


**Figure 2.15:** Cross section for  $tHW$  process as a function of  $\kappa_{Htt}$ , for three values of  $\kappa_{SM}$  at  $\sqrt{s} = 13$  TeV.  $\kappa_{Htt}^2 = \sigma_{Htt}/\sigma_{Htt}^{SM}$  is a simple rescaling of the SM Higgs interactions.

890 Results of the calculations of the  $tHq$  and  $tHW$  cross sections at  $\sqrt{s} = 13$  TeV can be  
 891 found in reference [49] and a summary of the results is presented in table 2.11.

892

## 893 2.5 The CP-mixing in tH processes

894 In addition to the sensitivity to sign of the H-t coupling,  $tHq$  and  $tHW$  processes have  
 895 been proposed as a tool to investigate the possibility of a H-t coupling that does not  
 896 conserve CP [43, 48, 50]. Current experimental results are consistent with SM H-V  
 897 and H-t couplings; however, negative H-t coupling is not excluded completely [53].

898

899 In this thesis, the sensitivity of  $tH$  processes to CP-mixing is also studied in the  
 900 effective field theory framework and based in references [43, 48]; a generic particle

	$\sqrt{s}$ TeV	$\kappa_t = 1$	$\kappa_t = -1$
$\sigma^{LO}(tHq)(fb)$ [41]	8	$\approx 17.4$	$\approx 252.7$
	14	$\approx 80.4$	$\approx 1042$
$\sigma^{NLO}(tHq)(fb)$ [41]	8	$18.28^{+0.42}_{-0.38}$	$233.8^{+4.6}_{-0.0}$
	14	$88.2^{+1.7}_{-0.0}$	$982.8^{+28}_{-0.0}$
$\sigma^{LO}(tHq)(fb)$ [47]	14	$\approx 71.8$	$\approx 893$
$\sigma^{LO}(tHW)(fb)$ [47]	14	$\approx 16.0$	$\approx 139$
$\sigma^{NLO}(tHq)(fb)$ [49]	8	$18.69^{+8.62\%}_{-17.13\%}$	-
	13	$74.25^{+7.48\%}_{-15.35\%}$	$848^{+7.37\%}_{-13.70\%}$
	14	$90.10^{+7.34\%}_{-15.13\%}$	$1011^{+7.24\%}_{-13.39\%}$
$\sigma^{LO}(tHW)(fb)$ [48]	13	$15.77^{+15.91\%}_{-15.76\%}$	-
$\sigma^{NLO}DR1(tHW)(fb)$ [48]	13	$21.72^{+6.52\%}_{-5.24\%}$	$\approx 150$
$\sigma^{NLO}DR2(tHW)(fb)$ [48]	13	$16.28^{+7.34\%}_{-15.13\%}$	$\approx 150$

**Table 2.11:** Predicted enhancement of the  $tHq$  and  $tHW$  cross sections at LHC for  $\kappa_V = 1$  and  $\kappa_t = \pm 1$  at LO and NLO; the cross section enhancement of more than a factor of 10 is due to the flippling in the sign of the H-t coupling with respect to the SM one.

901 ( $X_0$ ) of spin-0 and a general CP violating interaction with the top quark, can couple  
 902 to scalar and pseudoscalar fermionic densities. The H-W interaction is assumed to  
 903 be SM-like. The Lagrangian modeling the H-t interaction is given by

$$\mathcal{L}_0^t = -\bar{\psi}_t (c_\alpha \kappa_{Htt} g_{Htt} + i s_\alpha \kappa_{Att} g_{Att} \gamma_5) \psi_t X_0, \quad (2.58)$$

904 where  $\alpha$  is the CP-mixing phase,  $c_\alpha \equiv \cos \alpha$  and  $s_\alpha \equiv \sin \alpha$ ,  $\kappa_{Htt}$  and  $\kappa_{Att}$  are real  
 905 dimensionless rescaling parameters<sup>9</sup>,  $g_{Htt} = g_{Att} = m_t/v = y_t/\sqrt{2}$  and  $v \sim 246$  GeV is  
 906 the Higgs vacuum expectation value. In this parametrization, it is easy to recover  
 907 three special cases

908 • CP-even coupling  $\rightarrow \alpha = 0^\circ$

909 • CP-odd coupling  $\rightarrow \alpha = 90^\circ$

910 • SM coupling  $\rightarrow \alpha = 0^\circ$  and  $\kappa_{Htt} = 1$

---

<sup>9</sup> analog to  $\kappa_t$  and  $\kappa_V$

911 The loop induced  $X_0$  coupling to gluons can also be described in terms of the  
 912 parametrization above, according to

$$\mathcal{L}_0^g = -\frac{1}{4} \left( c_\alpha \kappa_{Hgg} g_{Hgg} G_{\mu\nu}^a G^{a,\mu\nu} + s_\alpha \kappa_{Agg} g_{Agg} G_{\mu\nu}^a \tilde{G}^{a,\mu\nu} \right) X_0. \quad (2.59)$$

913 where  $g_{Hgg} = -\alpha_s/3\pi v$  and  $g_{Agg} = \alpha_s/2\pi v$ . Under the assumption that the top quark  
 914 dominates the gluon-fusion process at LHC energies,  $\kappa_{Hgg} \rightarrow \kappa_{Htt}$  and  $\kappa_{Agg} \rightarrow \kappa_{Att}$ ,  
 915 so that the ratio between the gluon-gluon fusion cross section for  $X_0$  and for the SM  
 916 Higgs prediction can be written as

$$\frac{\sigma_{NLO}^{gg \rightarrow X_0}}{\sigma_{NLO,SM}^{gg \rightarrow H}} = c_\alpha^2 \kappa_{Htt}^2 + s_\alpha^2 \left( \kappa_{Att} \frac{g_{Agg}}{g_{Hgg}} \right)^2. \quad (2.60)$$

917 If the rescaling parameters are set to

$$\kappa_{Htt} = 1, \quad \kappa_{Att} = \left| \frac{g_{Hgg}}{g_{Agg}} \right| = \frac{2}{3}. \quad (2.61)$$

918 the gluon-fusion SM cross section is reproduced for every value of the CP-mixing  
 919 angle  $\alpha$ ; therefore, by imposing that condition to the Lagrangian density 2.58, the  
 920 CP-mixing angle is not constrained by current data. Figure 2.16 shows the NLO cross  
 921 sections for t-channel  $tX_0$  (blue) and  $t\bar{t}X_0$  (red) associated production processes as  
 922 a function of the CP-mixing angle  $\alpha$ .  $X_0$  is a generic spin-0 particle with top quark  
 923 CP-violating coupling. Rescaling factors  $\kappa_{Htt}$  and  $\kappa_{Att}$  have been set to reproduce  
 924 the SM gluon-fusion cross sections.

925 It is interesting to notice that the  $tX_0$  cross section is enhanced, by a factor of  
 926 about 10, when a continuous rotation in the scalar-pseudoscalar plane is applied; this  
 927 enhancement is similar to the enhancement produced when the H-t coupling is flipped  
 928 in sign with respect to the SM ( $y_t = -y_{t,SM}$  in the plot), as showed in section 2.4. In

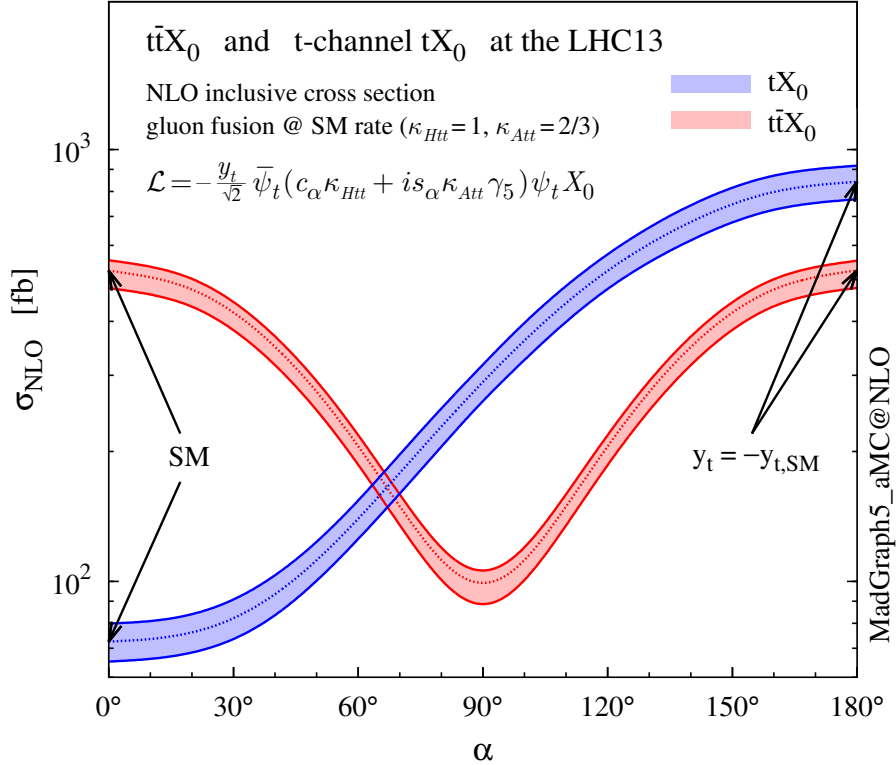


**Figure 2.16:** NLO cross sections for t-channel  $tX_0$ (blue) and  $t\bar{t}X_0$  (red) associated production processses as a function of the CP-mixing angle  $\alpha$ .  $X_0$  is a generic spin-0 particle with top quark CP-violating coupling [43].

929 contrast, the degeneracy in the  $t\bar{t}X_0$  cross section is still present given that it depends  
 930 quadratically on the H-t coupling, but more insteresting is to notice that  $t\bar{t}X_0$  cross  
 931 section is exceeded by  $tX_0$  cross section after  $\alpha \sim 60^\circ$ .

932 A similar parametrization can be used to investigate the  $tHW$ process sensitivity to  
 933 CP-violating H-t coupling. As said in 2.4, the interference in the W-associated chan-  
 934 nel is more complicated because there are more than two contributions and also there  
 935 is interference with the  $t\bar{t}H$  production process.

936

937 Figure 2.17 shows the NLO cross sections for t-channel  $tX_0$ (blue),  $t\bar{t}X_0$  (red) asso-  
 938 ciated production and for the combined  $tWX_0 + t\bar{t}X_0 +$  interference (orange) as a

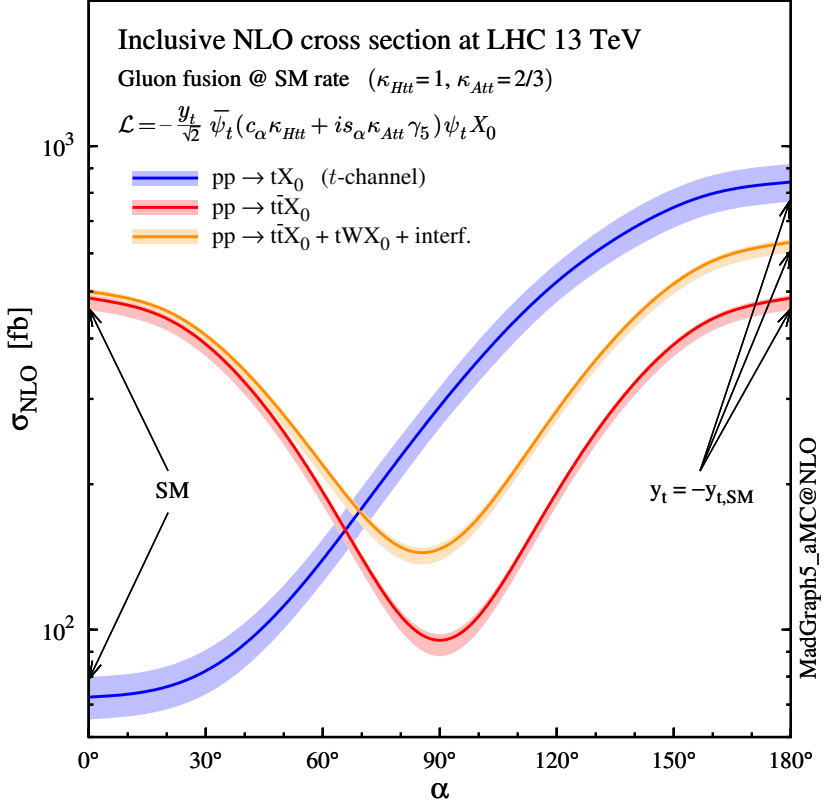


**Figure 2.17:** NLO cross sections for t-channel  $tX_0$  (blue),  $t\bar{t}X_0$  (red) associated production processes and combined  $tWX_0 + t\bar{t}X_0$  (including interference) production as a function of the CP-mixing angle  $\alpha$  [43].

function of the CP-mixing angle. It is clear that the effect of the interference in the combined case is the lifting of the degeneracy present in the  $t\bar{t}X_0$  production. The constructive interference enhances the cross section from about 500 fb at SM ( $\alpha = 0$ ) to about 600 fb ( $\alpha = 180^\circ \rightarrow y_t = -y_{t,SM}$ ).  
 An analysis combining  $tHq$  and  $tHW$  processes will be made in this thesis taking advantage of the sensitivity improvement.

945 **2.6 Experimantal status of the anomalous**  
 946 **Higg-fermion coupling.**

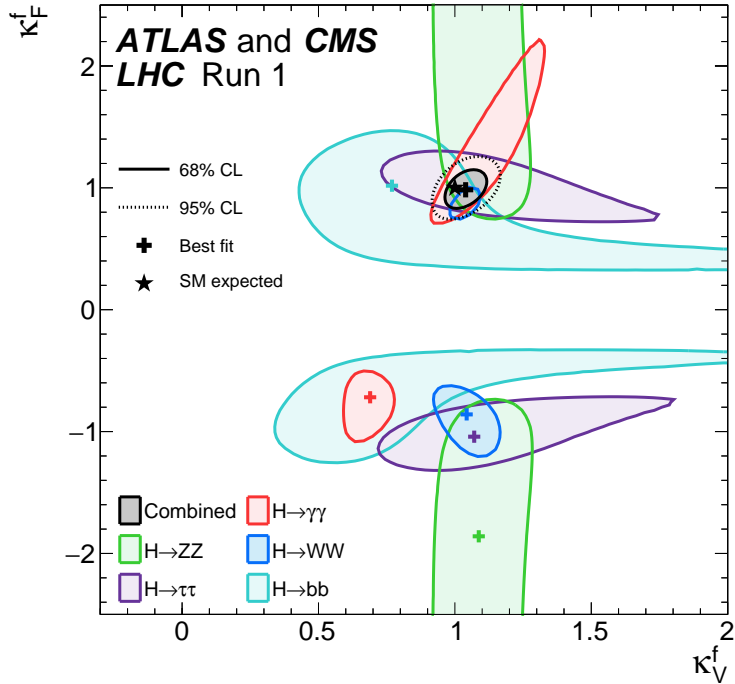


**Figure 2.18:** Combination of the ATLAS and CMS fits for coupling modifiers  $\kappa_t$ - $\kappa_V$ ; also shown the individual decay channels combination and their global combination. No assumptions have been made on the sign of the coupling modifiers [53].

947 ATLAS and CMS have performed analysis of the anomalous H-f coupling by making  
 948 likelihood scans for the two coupling modifiers,  $\kappa_t$  and  $\kappa_V$ , under the assumption that  
 949  $\kappa_Z = \kappa_W = \kappa_V$  and  $\kappa_t = \kappa_\tau = \kappa_b = \kappa_f$ . Figure 2.18 shows the result of the combination  
 950 of ATLAS and CMS fits; also the individual decay channels combination and the  
 951 global combination results are shown.

952 While all the channels are compatible for positive values of the modifiers, for negative  
 953 values of  $\kappa_t$  there is no compatibility. The best fit for individual channels is compatible  
 954 with negative values of  $\kappa_t$  except for the  $H \rightarrow bb$  channel which is expected to be the

955 most sensitive channel; therefore, the best fit for the global fit yields  $\kappa_t \geq 0$ . Thus,  
956 the anomalous H-t coupling cannot be excluded completely.

957 **Chapter 3**

958 **The CMS experiment at the LHC**

959 **3.1 Introduction**

960 Located on the Swiss-French border, the European Council for Nuclear Research  
961 (CERN) is the largest scientific organization leading the particle physics research.  
962 About 13000 people in a broad range of fields including users, students, scientists,  
963 engineers, among others, contribute to the data taking and analysis, with the goal  
964 of unveiling the secrets of nature and revealing the fundamental structure of the  
965 universe. CERN is also the home of the Large Hadron Collider (LHC), the largest  
966 circular particle accelerator around the world, where protons (or heavy ions) traveling  
967 close to the speed of light, are made to collide. These collisions open a window  
968 to investigate how particles (and their constituents if they are composite) interact  
969 with each other, providing clues about the laws of nature. This chapter presents an  
970 overview of the LHC structure and operation. A detailed description of the CMS  
971 detector is offered, given that the data used in this thesis have been taken with this  
972 detector.

## 973 3.2 The LHC

974 With 27 km of circumference, the LHC is currently the largest and most powerful  
 975 circular accelerator in the world. It is installed in the same tunnel where the Large  
 976 Electron-Positron (LEP) collider was located, taking advantage of the existing infras-  
 977 tructure. The LHC is also the larger accelerator in the CERN's accelerator complex  
 978 and is assisted by several successive accelerating stages before the particles are in-  
 979 jected into the LHC ring where they reach their maximum energy (see Figure 3.1).

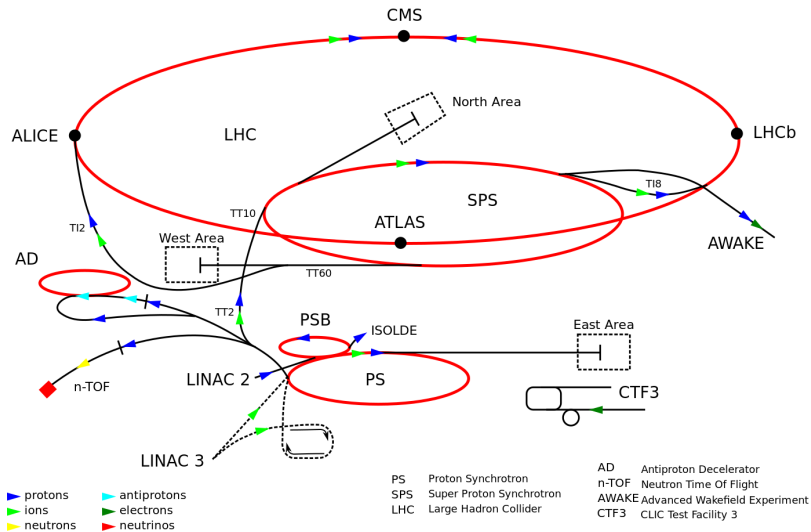


**Figure 3.1:** CERN accelerator complex. Blue arrows show the path followed by protons along the acceleration process [54].

980 LHC runs in three modes depending on the particles being accelerated

- 981     • Proton-Proton collisions ( $pp$ ) for multiple physics experiments.  
 982     • Lead-Lead collisions ( $Pb-Pb$ ) for heavy ion experiments.  
 983     • Proton-Lead collisions ( $p-Pb$ ) for quark-gluon plasma experiments.

984 In this thesis only  $pp$  collisions will be considered.

985

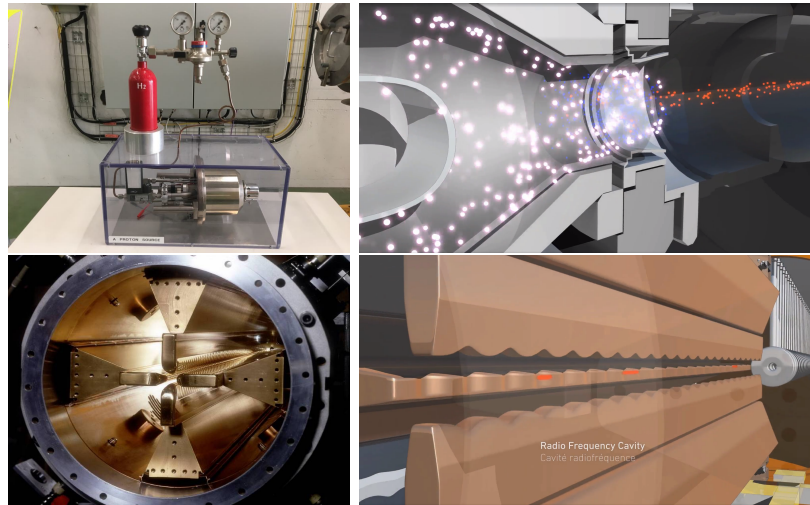


**Figure 3.2:** LHC protons source and the first acceleration stage. Top: the bottle contains hydrogen gas (white dots) which is injected into the metal cylinder to be broken down into electrons (blue dots) and protons (red dots); Bottom: the obtained protons are directed towards the radio frequency quadrupole which perform the first acceleration, focus the beam and create the bunches of protons. [58, 59]

986 Collection of protons starts with hydrogen atoms taken from a bottle, containing hy-  
 987 drogen gas, and injecting them in a metal cylinder; hydrogen atoms are broken down  
 988 into electrons and protons by an intense electric field (see Figure 3.2 top). The re-  
 989 sulting protons leave the metal cylinder towards a radio frequency quadrupole (RFQ)  
 990 that focus the beam, accelerates the protons and creates the packets of protons called  
 991 bunches. In the RFQ, an electric field is generated by a RF wave at a frequency that  
 992 matches the resonance frequency of the cavity where the electrodes are contained.  
 993 The beam of protons traveling on the RFQ axis experiences an alternating electric  
 994 field gradient that generates the focusing forces.

995

996 In order to accelerate the protons, a longitudinal time-varying electric field component  
 997 is added to the system; it is done by giving the electrodes a sinus-like profile as shown  
 998 in Figure 3.2 bottom. By matching the speed and phase of the protons with the  
 999 longitudinal electric field the bunching is performed; protons synchronized with the

1000 RFQ (synchronous proton) do not feel an accelerating force, but those protons in the  
 1001 beam that have more (or less) energy than the synchronous proton (asynchronous  
 1002 protons) will feel a decelerating (accelerating) force; therefore, asynchronous protons  
 1003 will oscillate around the synchronous ones forming bunches of protons [56]. From the  
 1004 RFQ protons emerge with energy 750 keV in bunches of about  $1.15 \times 10^{11}$  protons [57].

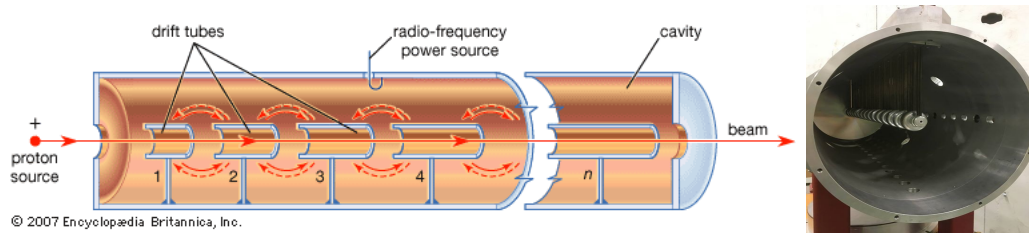


**Figure 3.3:** The LINAC2 accelerating system at CERN. Electric fields generated by radio frequency (RF) create acceleration and deceleration zones inside the cavity; deceleration zones are blocked by drift tubes where quadrupole magnets focus the proton beam. [60]

1005 Proton bunches coming from the RFQ go to the linear accelerator 2 (LINAC2) where  
 1006 they are accelerated to reach 50 MeV energy. In the LINAC2 stage, acceleration  
 1007 is performed using electric fields generated by radio frequency which create zones  
 1008 of acceleration and deceleration as shown in Figure 3.3. In the deceleration zones,  
 1009 the electric field is blocked using drift tubes where protons are free to drift while  
 1010 quadrupole magnets focus the beam.

1011

1012 The beam coming from LINAC2 is injected into the proton synchrotron booster  
 1013 (PSB) to reach 1.4 GeV in energy. The next acceleration is provided at the pro-  
 1014 ton synchrotron (PS) up to 26 GeV, followed by the injection into the super proton  
 1015 synchrotron (SPS) where protons are accelerated to 450 GeV. Finally, protons are  
 1016 injected into the LHC where they are accelerated to the target energy of 6.5 TeV.  
 1017 PSB, PS, SPS and LHC accelerate protons using the same RF acceleration technique  
 1018 described before.

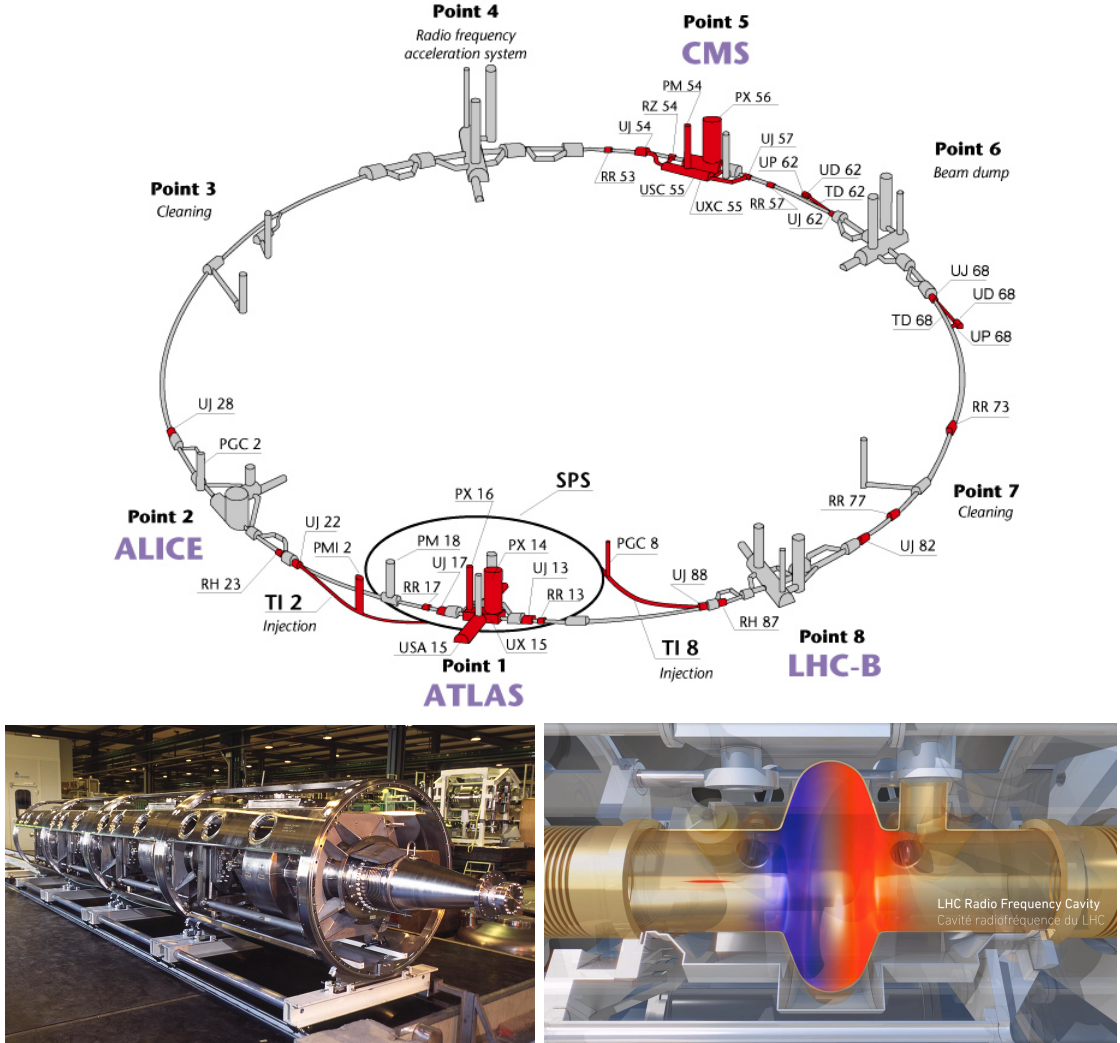


**Figure 3.4:** Top: LHC layout. The red zones indicate the infrastructure additions to the LEP installations, built to accommodate the ATLAS and CMS experiments which exceed the size of the former experiments located there [55]. Bottom: LHC RF cavities. A module accommodates 4 cavities that accelerate protons and preserve the bunch structure of the beam. [59, 61]

1019 LHC has a system of 16 RF cavities located in the so-called point 4, as shown in  
 1020 Figure 3.4 top, tuned at a frequency of 400 MHz and the protons are carefully timed,  
 1021 so in addition to the acceleration effect the bunch structure of the beam is preserved.  
 1022 Bottom side of Figure 3.4 shows a picture of a RF module composed of 4 RF cavities  
 1023 working in a superconducting state at 4.5 K; also is showed a representation of the

1024 accelerating electric field that accelerates the protons in the bunch.

1025

1026 While protons are accelerated in one section of the LHC ring, where the RF cavities  
 1027 are located, in the rest of their path they have to be kept in the curved trajectory  
 1028 defined by the LHC ring. Technically, LHC is not a perfect circle; RF, injection, beam  
 1029 dumping, beam cleaning and sections before and after the experimental points where  
 1030 protons collide are all straight sections. In total, there are 8 arcs 2.45 Km long each  
 1031 and 8 straight sections 545 m long each. In order to curve the proton's trajectory in  
 1032 the arc sections, superconducting dipole magnets are used.

1033

1034 Inside the LHC ring, there are two proton beams traveling in opposite directions in  
 1035 two separated beam pipes; the beam pipes are kept at ultra-high vacuum ( $\sim 10^{-9}$   
 1036 Pa) to ensure that there are no particles that interact with the proton beams. The  
 1037 superconducting dipole magnets used in LHC are made of a NbTi alloy, capable of  
 1038 transporting currents of about 12000 A when cooled at a temperature below 2K using  
 1039 liquid helium (see Figure 3.5).

1040

1041 Protons in the arc sections of LHC feel a centripetal force exerted by the dipole  
 1042 magnets which is perpendicular to the beam trajectory; The magnitude of magnetic  
 1043 field needed can be found assuming that protons travel at  $v \approx c$ , using the standard  
 1044 values for proton mass and charge and the LHC radius, as

$$F_m = \frac{mv^2}{r} = qBv \quad \rightarrow B = 8.33T \quad (3.1)$$

1045 which is about 100000 times the Earth's magnetic field. A representation of the mag-  
 1046 netic field generated by the dipole magnets is shown on the bottom left side of Figure

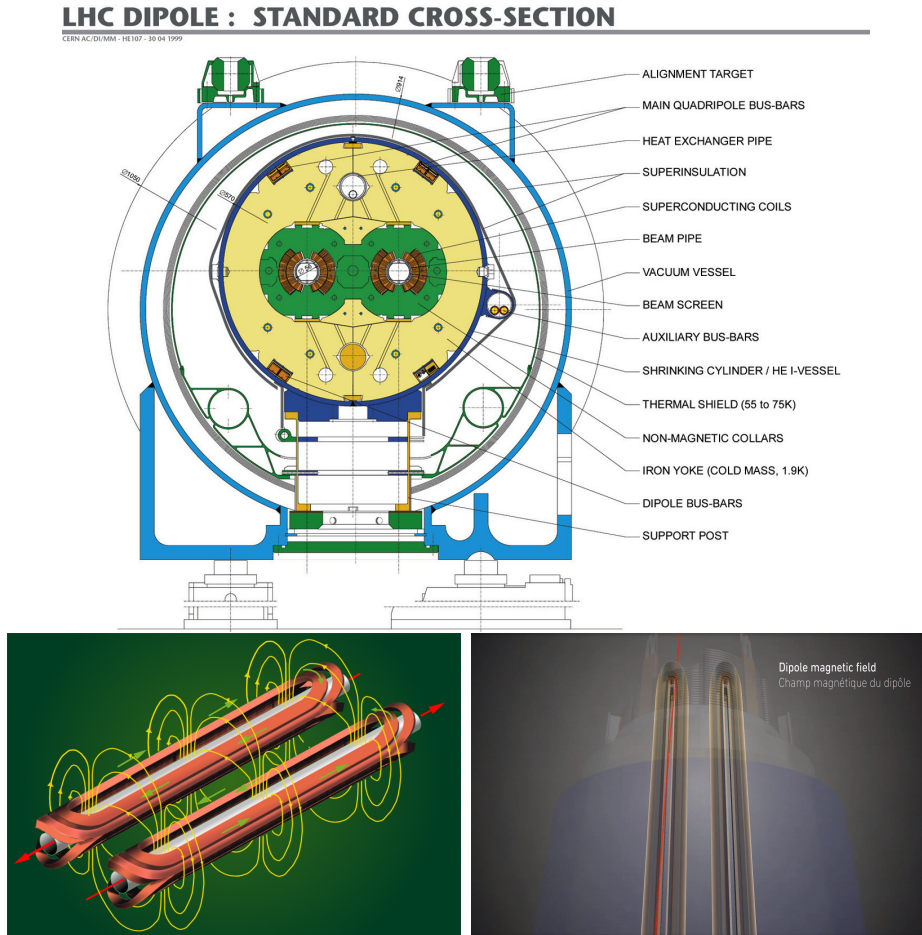


**Figure 3.5:** Top: LHC dipole magnet transverse view; cooling, shielding and mechanical support are indicated. Bottom left: Magnetic field generated by the dipole magnets; note that the direction of the field inside one beam pipe is opposite with respect to the other beam pipe which guarantee that both proton beams are curved in the same direction towards the center of the ring. The effect of the dipole magnetic field on the proton beam is represented on the bottom right side [59, 62, 63].

1047 3.5. The bending effect of the magnetic field on the proton beam is shown on the  
 1048 bottom right side of Figure 3.5. Note that the dipole magnets are not curved; the  
 1049 arc section of the LHC ring is composed of straight dipole magnets of about 15 m.  
 1050 In total there are 1232 dipole magnets along the LHC ring.

1051

1052 In addition to bending the beam trajectory, the beam has to be focused so it stays

1053 inside the beam pipe. The focusing is performed by quadrupole magnets installed in  
 1054 a different straight section; in total 858 quadrupole magnets are installed along the  
 1055 LHC ring. Other effects like electromagnetic interaction among bunches, interaction  
 1056 with electron clouds from the beam pipe, the gravitational force on the protons, dif-  
 1057 ferences in energy among protons in the same bunch, among others, are corrected  
 1058 using sextupole and other magnetic multipoles.

1059

1060 The two proton beams inside the LHC ring are made of bunches with a cylindrical  
 1061 shape of about 7.5 cm long and about 1 mm in diameter; when bunches are close  
 1062 to the collision point (CP), the beam is focused up to a diameter of about 16  $\mu\text{m}$  in  
 1063 order to maximize the number of collisions per unit area and per second, known as  
 1064 luminosity ( $L$ ). Luminosity can be calculated using

$$L = fn \frac{N_1 N_2}{4\pi\sigma_x\sigma_y} \quad (3.2)$$

1065 where  $f$  is the revolution frequency,  $n$  is the number of bunches per beam,  $N_1$  and  
 1066  $N_2$  are the numbers of protons per bunch ( $1.5 \times 10^{11}$ ),  $\sigma_x$  and  $\sigma_y$  are the gaussian  
 1067 transverse sizes of the bunches. The expected luminosity is about

$$f = \frac{v}{2\pi r_{LHC}} \approx \frac{3 \times 10^8 \text{ m/s}}{27 \text{ km}} \approx 11.1 \text{ kHz},$$

$$n = 2808$$

$$N_1 = N_2 = 1.5 \times 10^{11}$$

$$\sigma_x = \sigma_y = 16 \mu\text{m}$$

1068

$$L = 1.28 \times 10^{34} \text{ cm}^{-2} \text{ s}^{-1} = 1.28 \times 10^{-5} \text{ fb}^{-1} \text{ s}^{-1} \quad (3.3)$$

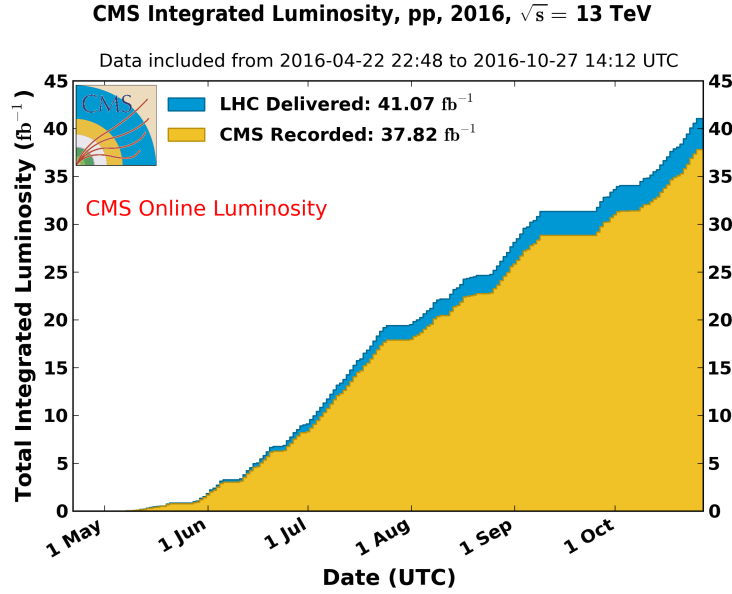


**Figure 3.6:** Integrated luminosity delivered by LHC and recorded by CMS during 2016. The difference between the delivered and the recorded luminosity is due to fails and issues occurred during the data taking in the CMS experiment [64].

1069 Luminosity is a fundamental aspect of LHC given that the bigger luminosity the  
 1070 bigger number of collisions, which means that for processes with a very small cross  
 1071 section the number of expected occurrences is increased and so the chances of being  
 1072 detected. The integrated luminosity, i.e., the total luminosity, collected by the CMS  
 1073 experiment during 2016 is shown in Figure 3.6; the data analyzed in this thesis cor-  
 1074 responds to an integrated luminosity of  $35.9 \text{ fb}^{-1}$  at a center of mass-energy  $\sqrt{s} = 13$   
 1075 TeV.

1076

1077 A way to increase  $L$  is increasing the number of bunches in the beam. Currently, the  
 1078 separation between two consecutive bunches in the beam is 7.5 m which corresponds  
 1079 to a time separation of 25 ns. In the full LHC ring the allowed number of bunches is  
 1080  $n = 27\text{km}/7.5\text{m} = 3600$ ; however, there are some gaps in the bunch pattern intended  
 1081 for preparing the dumping and injection of the beam, thus, the proton beams are

1082 composed of 2808 bunches.

1083

1084 Once the proton beams reach the desired energy, they are brought to cross each other  
 1085 producing proton-proton collisions. The bunch crossing happens in precise places  
 1086 where the four LHC experiments are located, as seen in the top of Figure 3.7. In  
 1087 2008, the first set of collisions involved protons with  $\sqrt{s} = 7$  TeV; the energy was  
 1088 increased to 8 TeV in 2012 and to 13 TeV in 2015.

1089

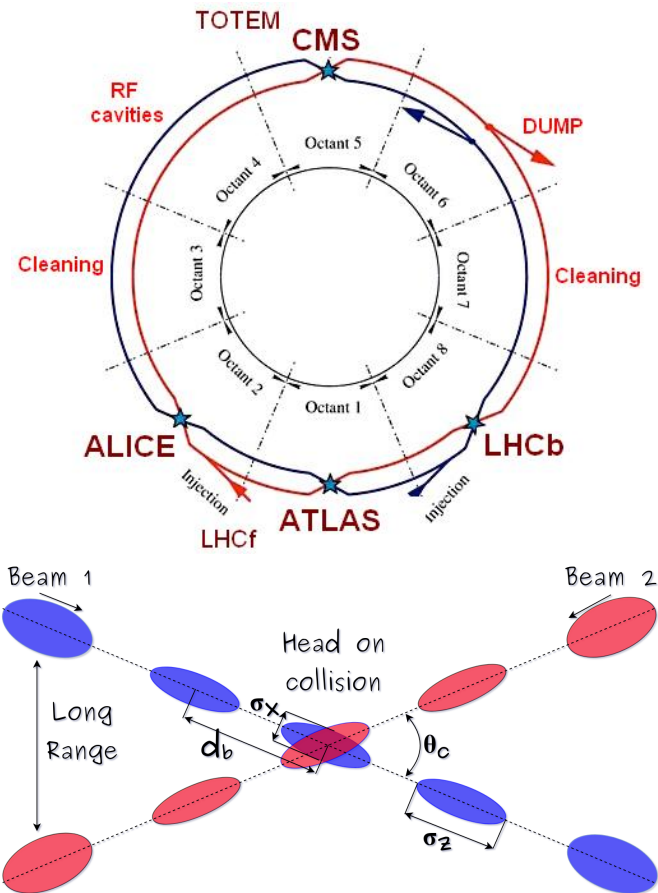


**Figure 3.7:** Top: LHC interaction points. Bunch crossing occurs where the LHC experiments are located [65]. Sections indicated as cleaning are dedicated to collimate the beam in order to protect the LHC ring from collisions with protons in very spreaded bunches. Bottom: bunch crossing scheme. Since the bunch crossing is not perfectly head-on, the luminosity is reduced in a factor of 17%; adapted from Reference [77].

1090 CMS and ATLAS experiments, which are multi-purpose experiments, are enabled  
 1091 to explore physics in any of the collision modes. LHCb experiment is optimized  
 1092 to explore bottom quark physics, while ALICE is optimized for heavy ion collisions  
 1093 searches; TOTEM and LHCf are dedicated to forward physics studies; MoEDAL (not  
 1094 indicated in the Figure) is intended for monopoles or massive pseudo stable particles  
 1095 searches.

1096

1097 At the CP there are two interesting details that need to be addressed. The first one  
 1098 is that the bunch crossing does not occur head-on but at a small crossing angle  $\theta_c$   
 1099 (280  $\mu$ rad in CMS and ATLAS) as shown in the bottom side of Figure 3.7, affecting  
 1100 the overlapping between bunches; the consequence is a reduction of about 17% in  
 1101 the luminosity (represented by a factor not included in eqn. 3.2). The second one  
 1102 is the occurrence of multiple  $pp$  collisions in the same bunch crossing; this effect is  
 1103 called pile-up (PU). A fairly simple estimation of the PU follows from estimating the  
 1104 probability of collision between two protons, one from each of the bunches in course  
 1105 of collision; it depends roughly on the ratio of proton size and the cross section of the  
 1106 bunch in the interaction point, i.e.,

$$P(pp\text{-}collision) \sim \frac{d_{proton}^2}{\sigma_x \sigma_y} = \frac{(1\text{fm})^2}{(16\mu\text{m})^2} \sim 4 \times 10^{-21} \quad (3.4)$$

1107 however, there are  $N = 1.15 \times 10^{11}$  protons in a bunch, thus the estimated number of  
 1108 collisions in a bunch crossing is

$$PU = N^2 * P(pp\text{-}collision) \sim 50 \text{ } pp\text{-}collision \text{ per bunch crossing}, \quad (3.5)$$

1109 about 20 of those  $pp$  collisions are inelastic. Each collision generates a vertex, but  
 1110 only the most energetic is considered as a primary vertex; the rest are considered

as PU vertices. A multiple  $pp$  collision event in a bunch crossing at CMS is showed in Figure 3.8. Unstable particles outgoing from the primary vertex will eventually decay; this decay vertex is known as a secondary vertex.

1114

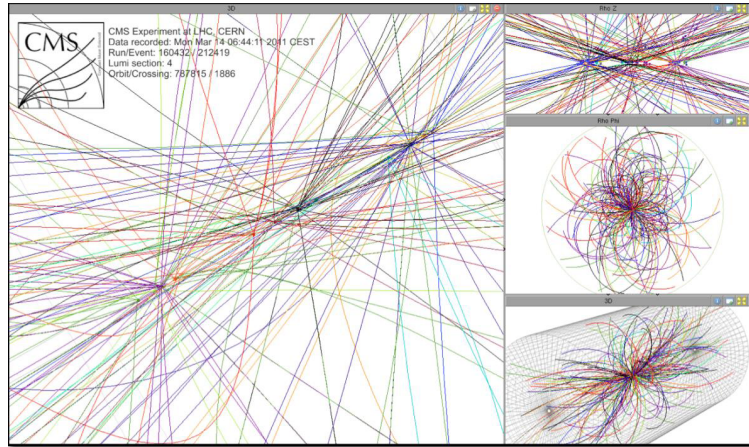


**Figure 3.8:** Multiple  $pp$  collision bunch crossing at CMS. Only the most energetic vertex is considered and the rest are cataloged as PU vertices [66].

1115 Next section presents a description of the CMS detector which it is the detector used  
1116 to collect the data used in this thesis.

### 1117 3.3 The CMS experiment

1118 CMS is a general-purpose detector designed to conduct research in a wide range  
1119 of physics from the standard model to new physics like extra dimensions and dark  
1120 matter. Located at the point 5 in the LHC layout as shown in Figure 3.4, CMS is  
1121 composed of several detection systems distributed in a cylindrical structure; in total,  
1122 CMS weights about 12500 tons in a very compact 21.6 m long and 14.6 m diameter  
1123 cylinder. It was built in 15 separate sections at the ground level and lowered to the  
1124 cavern individually to be assembled. A complete and detailed description of the CMS  
1125 detector and its components is given in Reference [67] on which this section is based

1126 on.

1127

1128 Figure 3.9 shows the layout of the CMS detector. The design is driven by the require-  
 1129 ments on the identification, momentum resolution and unambiguous charge determi-  
 1130 nation of the muons; therefore, a large bending power is provided by the solenoid  
 1131 magnet made of superconducting cable capable to generate a 3.8 T magnetic field.  
 1132 The detection system is composed of (from the innermost to the outermost)

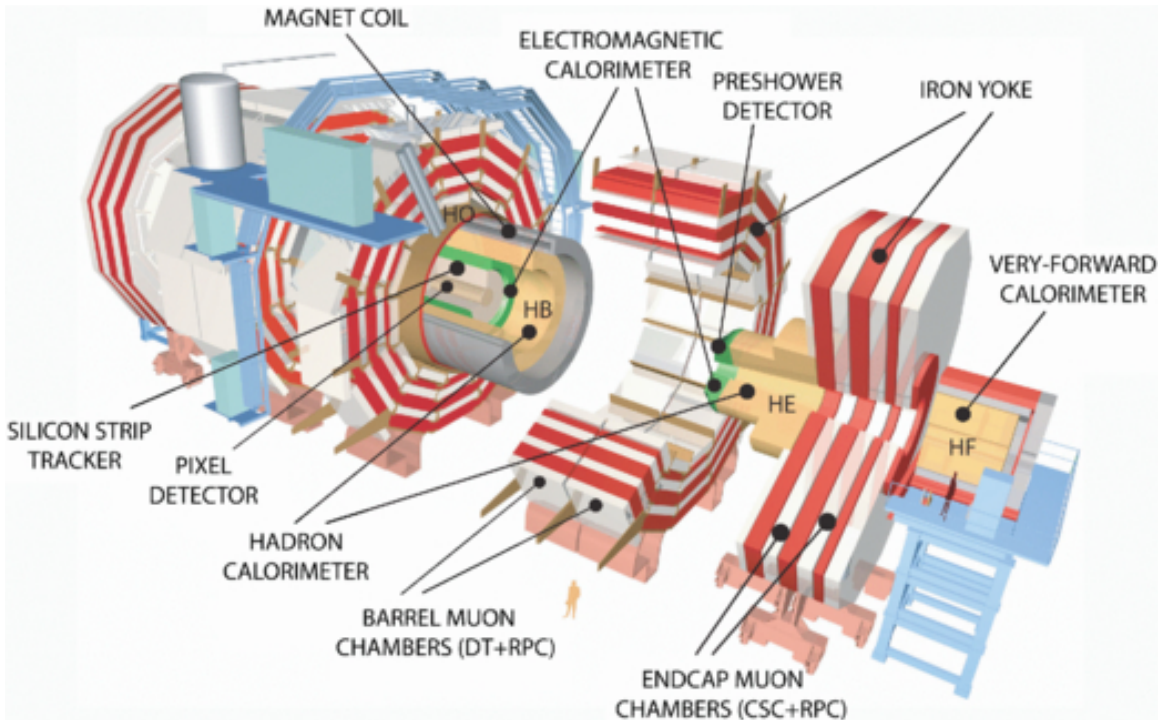


**Figure 3.9:** Layout of the CMS detector. The several subdetectors are indicated. The central region of the detector is referred as the Barrel section while the endcaps are referred as the forward sections. [68].

1133 • Pixel detector.

1134 • Silicon strip tracker.

1135 • Preshower detector.

1136 • Electromagnetic calorimeter.

1137 • Hadronic calorimeter.

1138 • Muon chambers (Barrel and endcap)

1139 The central region of the detector is commonly referred as the barrel section while the  
 1140 endcaps are referred as the forward sections of the detector; thus, each subdetector  
 1141 is composed of a barrel section and a forward section.

### 1142 3.3.1 Coordinate system

1143 The coordinate system used by CMS is centered in the geometrical center of the  
 1144 detector which is the same as the CP as shown in Figure 3.10. The  $z$ -axis is parallel  
 1145 to the beam direction, while the  $Y$ -axis pointing vertically upward, and the  $X$ -axis  
 1146 pointing radially inward toward the center of the LHC.

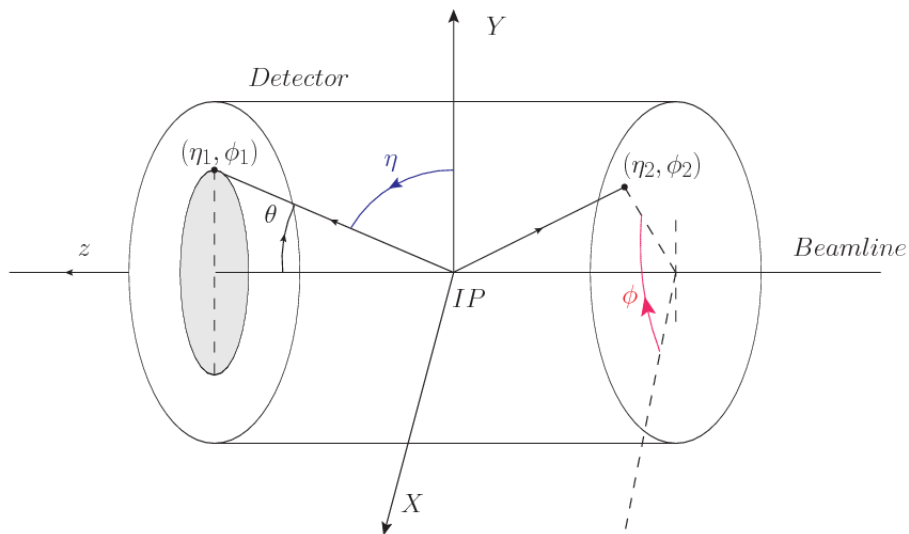


**Figure 3.10:** CMS detector coordinate system.

1147 In addition to the common cartesian and cylindrical coordinate systems, two coor-  
 1148 dinates are of particular utility in particle physics: rapidity ( $y$ ) and pseudorapidity

1149  $(\eta)$ , defined in connection to the polar angle  $\theta$ , energy and longitudinal momentum  
 1150 component (momentum along the  $z$ -axis) according to

$$y = \frac{1}{2} \ln \frac{E + p_z}{E - p_z} \quad \eta = -\ln \left( \tan \frac{\theta}{2} \right) \quad (3.6)$$

1151 Rapidity is related to the angle between the  $XY$ -plane and the direction in which the  
 1152 products of a collision are emitted; it has the nice property that the difference between  
 1153 the rapidities of two particles is invariant with respect to Lorentz boosts along the  $z$ -  
 1154 axis. Thus, data analysis becomes more simple when based on rapidity; however, it is  
 1155 not simple to measure the rapidity of highly relativistic particles, as those produced  
 1156 after  $pp$  collisions. Under the highly relativistic motion approximation,  $y$  can be  
 1157 rewritten in terms of the polar angle, concluding that rapidity is approximately equal  
 1158 to the pseudorapidity defined above, i.e.,  $y \approx \eta$ . Note that  $\eta$  is easier to measure than  $y$   
 1159 given the direct relationship between the former and the polar angle. Angular distance  
 1160 between two objects in the detector ( $\Delta R$ ) is defined in terms of their coordinates  
 1161  $(\eta_1, \phi_1), (\eta_2, \phi_2)$  as

$$\Delta R = \sqrt{(\Delta\eta)^2 - (\Delta\phi)^2} \quad (3.7)$$

### 1162 3.3.2 Pixels detector

1163 The CMS tracking system is designed to provide a precise measurement of the tra-  
 1164 jectory (*track*) followed by the charged particles created after the  $pp$  collisions; also,  
 1165 the precise reconstruction of the primary and secondary origins (*vertices*) is expected  
 1166 in an environment where, each 25 ns, the bunch crossing produce about 20 inelastic  
 1167 collisions and about 1000 particles. An increment in the luminosity is ongoing which  
 1168 implies that the PU will increase accordingly.

1170 The pixel detector was replaced during the 2016-2017 extended year-end technical  
1171 stop, due to the increasingly challenging operating conditions like the higher particle  
1172 flow and more radiation harsh environment, among others. The new one is responding  
1173 as expected, reinforcing its crucial role in the successful way to fulfill the new LHC  
1174 physics objectives after the discovery of the Higgs boson. The last chapter of this  
1175 thesis is dedicated to describe my contribution to the *Forward Pixel Phase 1 upgrade*.

1176

1177 The current pixel detector is composed of 1856 silicon pixel detector modules orga-  
1178 nized in four-barrel layers in the central region and three disks in the forward region;  
1179 it is designed to record efficiently and with high precision, up to  $10\mu\text{m}$  in the  $XY$ -  
1180 plane and  $20\mu\text{m}$  in the  $z$ -direction, the first four space-points (*hits*) near to the CP  
1181 region (see Figure 3.11 left side) in the range  $|\eta| \leq 2.5$ . The first barrel layer is located  
1182 at a radius of 30 mm from the beamline, while the fourth layer is located at a radius  
1183 of 160 mm closer to the strip tracker inner barrel layer (see Section 3.3.3) in order to  
1184 reduce the rate of fake tracks. The high granularity of the detector is represented in  
1185 its about 123 Mpixels, each of size  $100 \times 150\mu\text{m}^2$ , which is almost twice the channels  
1186 of the old detector. The transverse momentum resolution of tracks can be measured  
1187 with a resolution of 1-2% for muons of  $p_T = 100$  GeV.

1188

1189 Some of the improvements with respect to the previous pixel detector include a higher  
1190 average tracking efficiency and lower average fake rate as well as higher track impact  
1191 parameter resolution which is fundamental in order to increase the efficiency in the  
1192 identification of jets originating from b quarks (b-tagging). A significant source of  
1193 improvement comes from the overall reduction in the material budget of the detector  
1194 which results in fewer photon conversions and less multiple scattering from charged  
1195 particles.

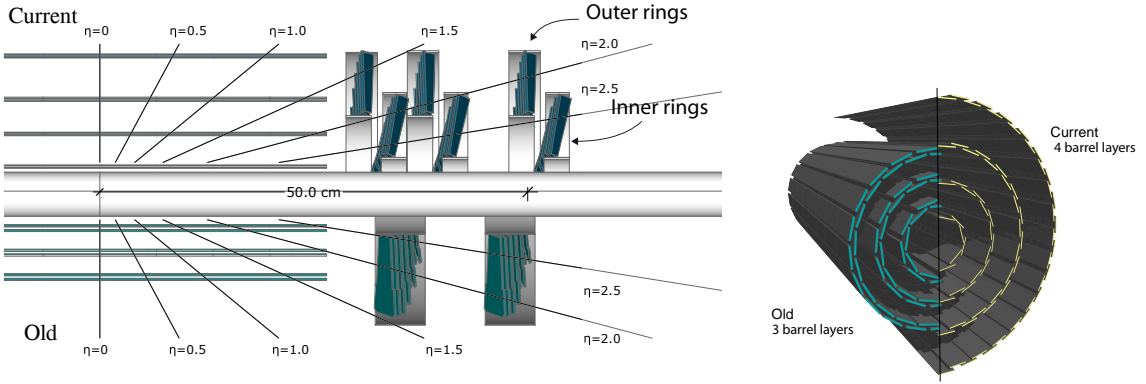


**Figure 3.11:** CMS pixel detector schematic view. Left: layout comparing the layers and disks in the old and current pixel detectors. Right: Transverse-oblique view comparing the pixel barrel layers in the two [70].

### 1196 3.3.3 Silicon strip tracker

1197 The silicon strip tracker (SST) is the second stage in the CMS tracking system. The  
 1198 top side of Figure 3.12 shows a schematic of the SST. The inner tracker region is com-  
 1199 posed of the tracker inner barrel (TIB) and the tracker inner disks (TID) covering the  
 1200 region  $r < 55$  cm and  $|z| < 118$  cm. The TIB is composed of 4 layers while the TID  
 1201 is composed of 3 disks at each end. The silicon sensors in the inner tracker are 320  
 1202  $\mu\text{m}$  thick, providing a resolution of about 13-38  $\mu\text{m}$  in the  $r\phi$  position measurement.  
 1203

1204 The modules indicated in blue in the schematic view of Figure 3.12 are two modules  
 1205 mounted back-to-back and rotated in the plane of the module by a *stereo* angle of  
 1206 100 mrad; the hits from these two modules, known as *stereo hits*, are combined to  
 1207 provide a measurement of the second coordinate ( $z$  in the barrel and  $r$  on the disks)  
 1208 allowing the reconstruction of hit positions in 3-D.

1209

1210 The outer tracker region is composed of the tracker outer barrel (TOB) and the  
 1211 tracker endcaps (TEC). The six layers of the TOB offer coverage in the region  $r > 55$

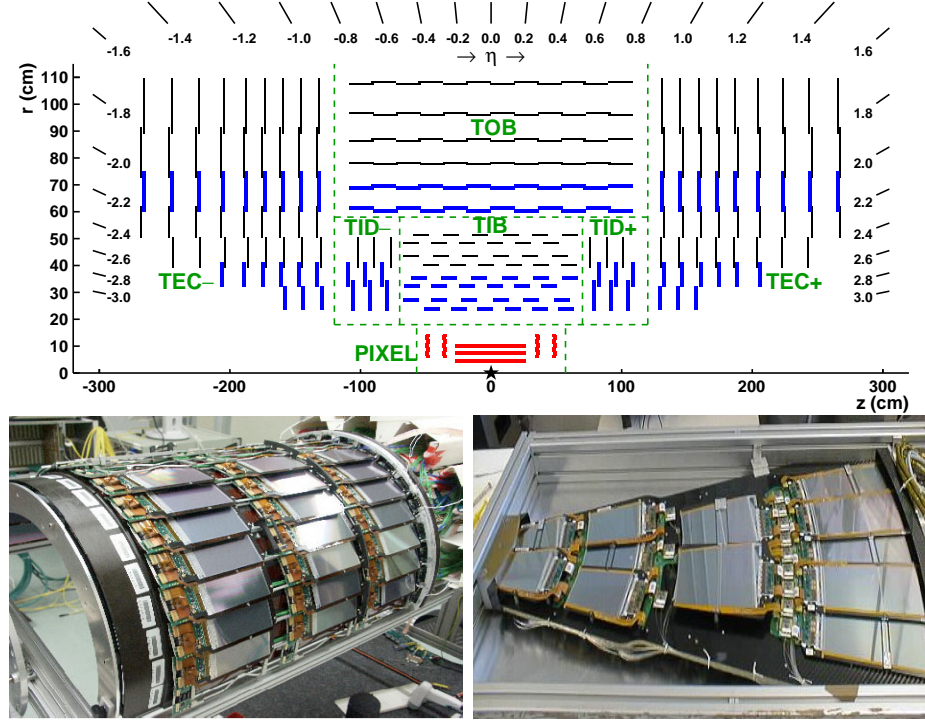


**Figure 3.12:** Top: CMS Silicon Strip Tracker (SST) schematic view. The SST is composed of the tracker inner barrel (TIB), the tracker inner disks (TID), the tracker outer barrel (TOB) and the tracker endcaps (TEC). Each part is made of silicon strip modules; the modules in blue represent two modules mounted back-to-back and rotated in the plane of the module by a stereo angle of 120 mrad in order to provide a 3-D reconstruction of the hit positions. Bottom: pictures of the TIB (left) and TEC (right) modules [71–73].

1212 cm and  $|z| < 118$  cm, while the 9 disks of the TEC cover the region  $124 < |z| < 282$   
 1213 cm. The resolution offered by the outer tracker is about  $13\text{--}38 \mu\text{m}$  in the  $r\phi$  position  
 1214 measurement. The inner four TEC disks use silicon sensors  $320 \mu\text{m}$  thick; those in  
 1215 the TOB and the outer three TEC disks use silicon sensors of  $500 \mu\text{m}$  thickness. The  
 1216 silicon strips run parallel to the  $z$ -axis and the distance between strips varies from 80  
 1217  $\mu\text{m}$  in the inner TIB layers to  $183 \mu\text{m}$  in the inner TOB layers; in the endcaps the  
 1218 wedge-shaped sensors with radial strips, whose pitch range between  $81 \mu\text{m}$  at small  
 1219 radii and  $205 \mu\text{m}$  at large radii.

1220

1221 The whole SST has 15148 silicon modules, 9.3 million silicon strips and cover a total

1222 active area of about  $198 \text{ m}^2$ .

1223 **3.3.4 Electromagnetic calorimeter**

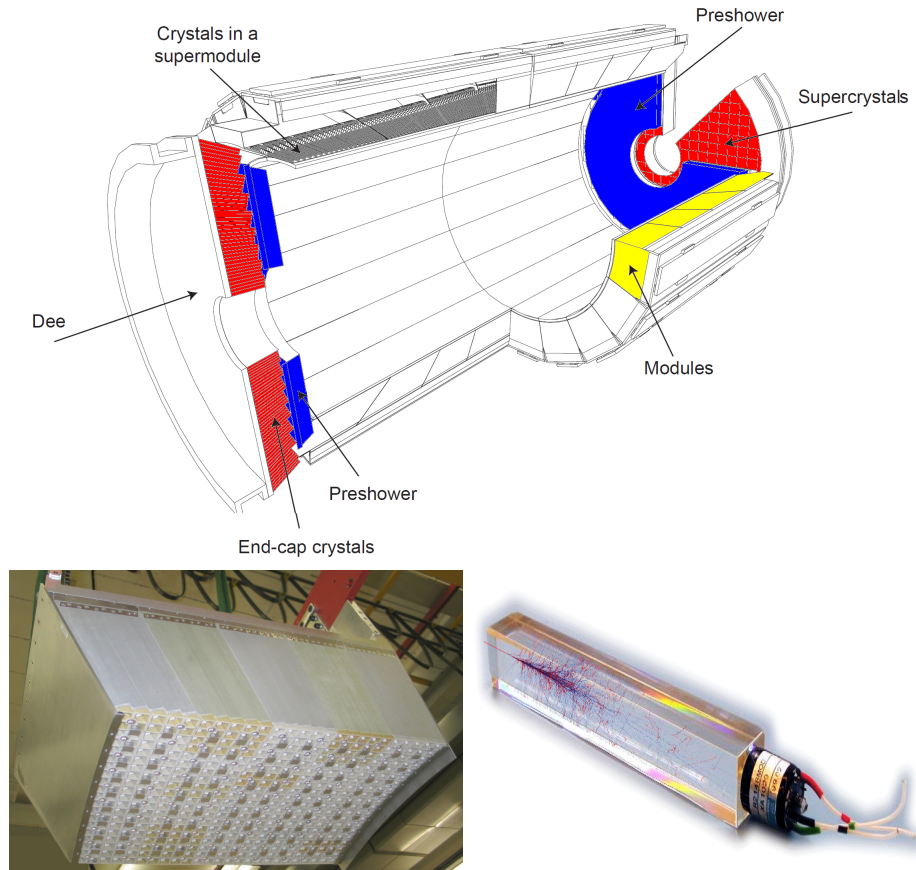


**Figure 3.13:** Top: CMS ECAL schematic view. Bottom: Module equipped with the crystals (left); ECAL crystal(right).

1224 The CMS electromagnetic calorimeter (ECAL) is designed to measure the energy of  
 1225 electrons and photons. It is composed of 75848 lead tungstate crystals which have a  
 1226 short radiation length (0.89 cm) and fast response, since 80% of the light is emitted  
 1227 within 25 ns; however, they are combined with Avalanche photodiodes (APDs) as  
 1228 photodetectors given that crystals themselves have a low light yield ( $30\gamma/\text{MeV}$ ). A

1229 schematic view of the ECAL is shown in Figure 3.13.

1230

1231 Energy is measured when electrons and photons are absorbed by the crystals which  
 1232 generates an electromagnetic *shower*, as seen in bottom right picture of the Figure  
 1233 3.13; the shower is seen as a *cluster* of energy which depending on the amount of en-  
 1234 ergy deposited can involve several crystals. The ECAL barrel (EB) covers the region  
 1235  $|\eta| < 1.479$ , using crystals of depth of 23 cm and  $2.2 \times 2.2 \text{ cm}^2$  transverse section;  
 1236 the ECAL endcap (EE) covers the region  $1.479 < |\eta| < 3.0$  using crystals of depth  
 1237 22 cm and transverse section of  $2.86 \times 2.86 \text{ cm}^2$ ; the photodetectors used are vacuum  
 1238 phototriodes (VPTs). Each EE is divided in two structures called *Dees*.

1239

1240 In front of the EE, it is installed the preshower detector (ES) which covers the region  
 1241  $1.653 < |\eta| < 2.6$ . The ES provides a precise measurement of the position of electro-  
 1242 magnetic showers, which allows to distinguish electrons and photons signals from  $\pi^0$   
 1243 decay signals. The ES is composed of a layer of lead absorber followed by a layer of  
 1244 plastic scintillators

### 1245 3.3.5 Hadronic calorimeter

1246 Hadrons are not absorbed by the ECAL but by the hadron calorimeter (HCAL),  
 1247 which is made of a combination of alternating brass absorber layers and silicon photo-  
 1248 multiplier(SiPM) layers; therefore, particles passing through the scintillator material  
 1249 produce showers, as in the ECAL, as a result of the inelastic scattering of the hadrons  
 1250 with the detector material. Since the particles are not absorbed in the scintillator,  
 1251 their energy is sampled; therefore the total energy is not measured but estimated from  
 1252 the energy clusters, which reduce the resolution of the detector. Brass was chosen

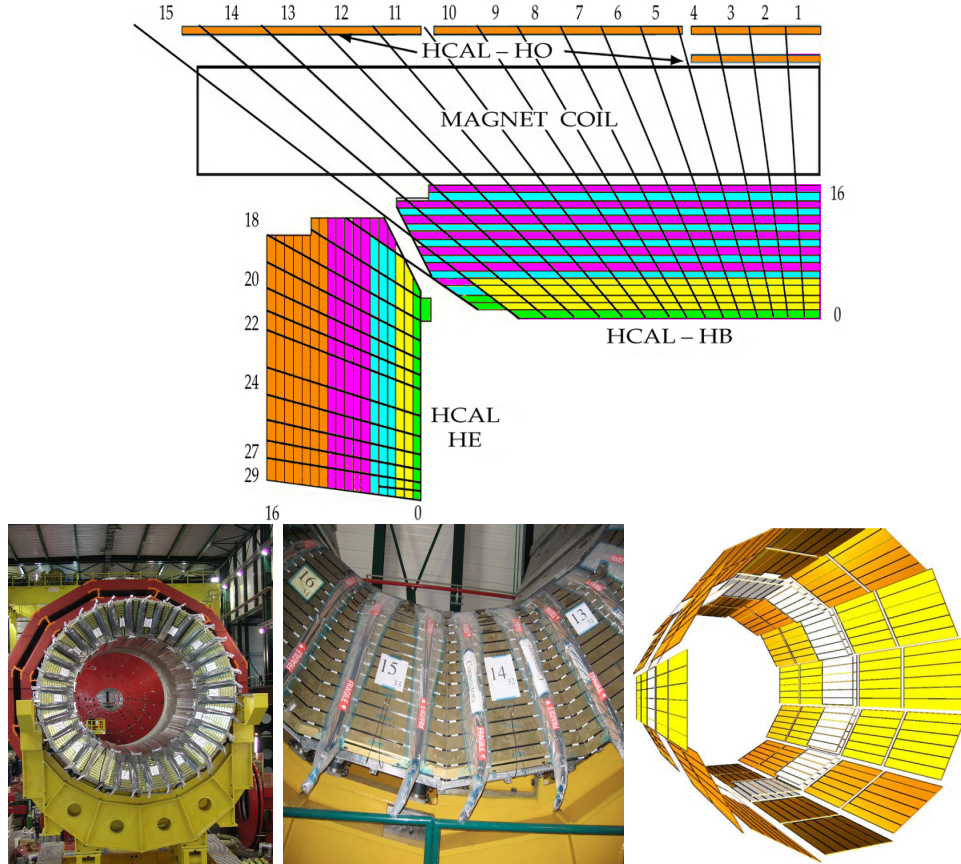


**Figure 3.14:** Top: CMS HCAL schematic view, the colors indicate the layers that are grouped into the same readout channels. Bottom: picture of a section of the HB; the absorber material is the golden region and scintillators are placed in between the absorber material (left and center). Schematic view of the HO (right). [74,75]

as the absorber material due to its short interaction length ( $\lambda_I = 16.42\text{cm}$ ) and its non-magnetivity. Figure 3.14 shows a schematic view of the CMS HCAL.

1255

1256 The HCAL is divided into four sections; the Hadron Barrel (HB), the Hadron Outer  
 1257 (HO), the Hadron Endcap (HE) and the Hadron Forward (HF) sections. The HB  
 1258 covers the region  $0 < |\eta| < 1.4$ , while the HE covers the region  $1.3 < |\eta| < 3.0$ . The HF,  
 1259 made of quartz fiber scintillator and steel as absorption material, covers the forward  
 1260 region  $3.0 < |\eta| < 5.2$ . Both the HB and HF are located inside the solenoid. The HO

is placed outside the magnet as an additional layer of scintillators with the purpose of measure the energy tails of particles passing through the HB and the magnet (see Figure 3.14 top and bottom right). The upgrades made to the HCAL during the technical stop 2016-2017 consisted in the replacement of the photo transducer, in order to improve the efficiency.

### 3.3.6 Superconducting solenoid magnet

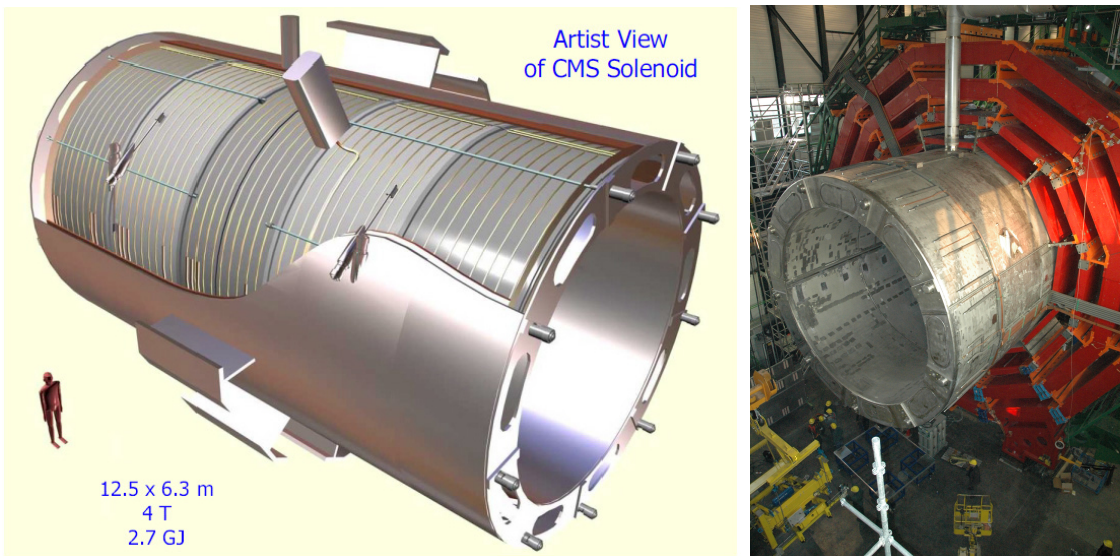


**Figure 3.15:** Artistic representation of the CMS solenoid magnet(left). The magnet is supported on an iron yoke (right) which also serves as the house of the muon detector and as mechanical support for the whole CMS detector [69].

The superconducting magnet installed in the CMS detector is designed to provide an intense and highly uniform magnetic field in the central part of the detector. In fact, the tracking system takes advantage of the bending power of the magnetic field to measure with precision the momentum of the particles that traverse it; the unambiguous determination of the sign for high momentum muons was a driven principle during the design of the magnet. The magnet has a diameter of 6.3 m, a length of 12.5 m and a cold mass of 220 t; the generated magnetic field reaches a strength of 3.8T.

1274 Since it is made of Ni-Tb superconducting cable it has to operate at a temperature  
 1275 of 4.7 K by using a helium cryogenic system; the current circulating in the cables  
 1276 reaches 18800 A under normal running conditions. The left side of Figure 3.15 shows  
 1277 an artistic view of the CMS magnet, while the right side shows a transverse view of  
 1278 the cold mass where the winding structure is visible.

1279

1280 The yoke (see Figure 3.15), composed of 5 barrel wheels and 6 endcap disks made  
 1281 of iron, serves not only as the media for magnetic flux return but also provides the  
 1282 house for the muon detector system and structural stability to the full detector.

### 1283 3.3.7 Muon system

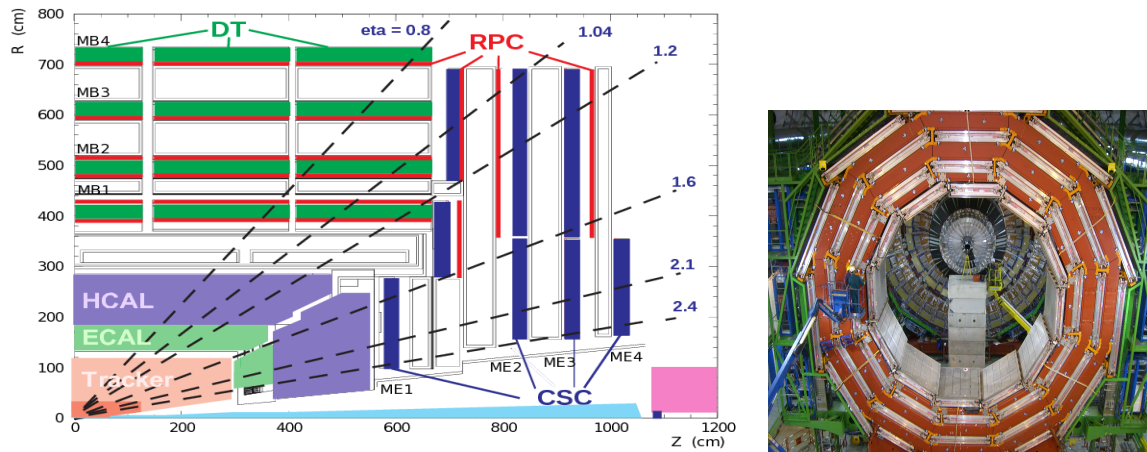


**Figure 3.16:** Left: CMS muon system schematic view; Right: one of the yoke rings with the muon DTs and RPCs installed; in the back it is possible to see the muon endcap [76].

1284 Muons are the only charged particles able to pass through all the CMS detector due  
 1285 to their low ionization energy loss; thus, muons can be separated easily from the  
 1286 high amount of particles produced in a  $pp$  collision. Also, muons are expected to be  
 1287 produced in the decay of several new particles; therefore, a good detection of muons

1288 was on the leading principles when designing the CMS detector.

1289

1290 The CMS muon detection system (muon spectrometer) is embedded in the return  
1291 yoke as seen in Figure 3.16. It is composed of three different detector types, the drift  
1292 tube chambers (DT), Cathode strip chambers (CSC), and resistive plate chambers  
1293 (RPC); DT are located in the central region  $\eta < 1.2$  arranged in four layers of drift  
1294 chambers filled with an Ar/CO<sub>2</sub> gas mixture.

1295

1296 The muon endcaps are made of CSCs covering the region  $\eta < 2.4$  and filled with a  
1297 mixture of Ar/CO<sub>2</sub>/CF<sub>4</sub>. The reason behind using a different detector type lies on  
1298 the different conditions in the forward region like the higher muon rate and higher  
1299 residual magnetic field compared to the central region.

1300

1301 The third type of detector used in the muon system is a set of four disks of RPCs  
1302 working in avalanche mode. The RPCs provide good spatial and time resolutions.  
1303 The track of  $high - p_T$  muon candidates is built combining information from the  
1304 tracking system and the signal from up to six RPCs and four DT chambers.  
1305 The muon tracks are reconstructed from the hits in the several layers of the muon  
1306 system.

### 1307 **3.3.8 CMS trigger system**

1308 Under normal conditions, CMS expects  $pp$  collisions every 25 ns, i.e., an interaction  
1309 rate of 40 MHz for which it is not possible to store the recorded data in full. In order  
1310 to handle this high event rate data, an online event selection, known as triggering, is  
1311 performed; triggering reduce the event rate to 100 Hz for storage and further offline

1312 analysis.

1313

1314 The trigger system starts with a reduction of the event rate to 100 kHz in the so-  
 1315 called *level 1 trigger (L1)*. L1 is based on dedicated programmable hardware like  
 1316 Field Programmable Gate Arrays (FPGAs) and Application Specific Integrated Cir-  
 1317 cuits (ASICs), partly located in the detector itself; another portion is located in the  
 1318 CMS under-ground cavern. Hit patterns information from the muon chambers and  
 1319 the energy deposits in the calorimeter are used to decide if an event is accepted or  
 1320 rejected, according to selection requirements previously defined, which reflect the in-  
 1321 teresting physics processes. Figure 3.17 shows the L1 trigger architecture.

1322

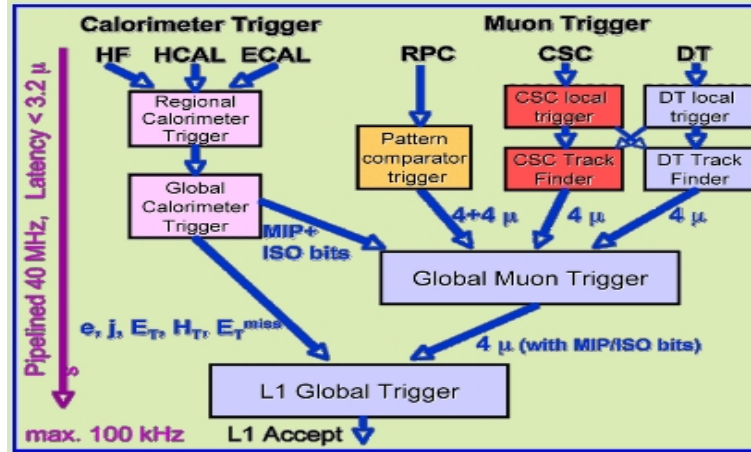


**Figure 3.17:** CMS Level-1 trigger architecture [77].

1323 The second stage in the trigger system is called *high-level trigger (HLT)*; events ac-  
 1324 cepted by L1 are passed to HLT in order to make an initial reconstruction of them.  
 1325 HLT is software based and runs on a dedicated server farm, using selection algo-  
 1326 rithms and high-level object definitions; the event rate at HLT is reduced to 100 Hz.  
 1327 The first HLT stage takes information from the muon detectors and the calorimeters  
 1328 to make the initial object reconstruction; in the next HLT stage, information from

1329 the pixel and strip detectors is used to do first fast-tracking and then full tracking  
1330 online. This initial object reconstruction is used in further steps of the trigger system.

1331

1332 Events and preliminary reconstructed physics objects from HLT are sent to be fully  
1333 reconstructed at the CERN computing center. Again, the pixel detector information  
1334 provides high-quality seeds for the track reconstruction algorithm offline, primary ver-  
1335 tex reconstruction, electron and photon identification, muon reconstruction,  $\tau$  iden-  
1336 tification, and b-tagging. After full reconstruction, data sets are made available for  
1337 offline analyses.

1338

1339 During the 2016-2017 technical stop, the L1 system was updated in order to improve  
1340 the physics object identification by improving the algorithms and accounting for the  
1341 increasing pile-up scenario.

### 1342 **3.3.9 CMS computing**

1343 After the data, coming from the experiment, are processed at several levels, they have  
1344 to be stored and made available for further analysis; in order to cope all the tasks  
1345 implied in the offline data processing, like transfer, simulation, reconstruction and  
1346 reprocessing, among others, a big computing power is required. The CMS computing  
1347 system is based on the distributed architecture concept, where users of the system  
1348 and physical computer centers are distributed worldwide and interconnected by high-  
1349 speed networks.

1350 The worldwide LHC computing grid (WLCG) is the mechanism used to provide that  
1351 distributed environment. WLCG is a tiered structure connecting computing centers  
1352 around the world, which provides the necessary storage and computing facilities. The

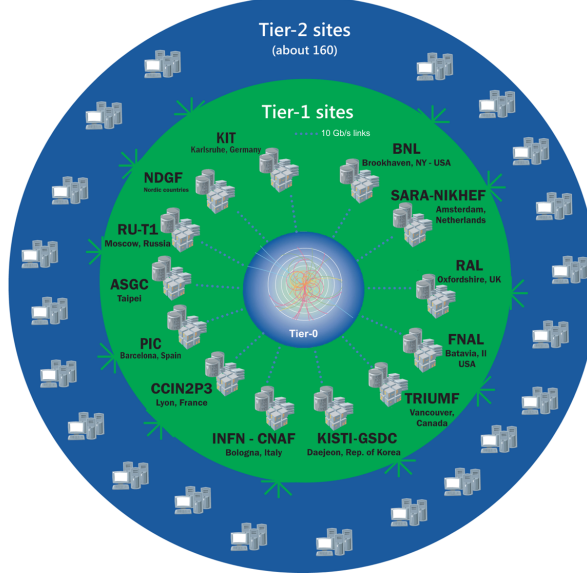


**Figure 3.18:** WLCG structure. The primary computer centers (Tier-0) are located at CERN (data center) and at the Wigner datacenter in Budapest. Tier-1 is composed of 13 centers and Tier-2 is composed of about 160 centers. [78].

1353 primary computing centers of the WLCG are located at the CERN and the Wigner  
 1354 datacenter in Budapest and are known as Tier-0 as shown in Figure 3.18. The main  
 1355 responsibilities for each tier level are [78]

- 1356     • **Tier-0:** initial reconstruction of recorded events and storage of the resulting  
               datasets, the distribution of raw data to the Tier-1 centers.
- 1358     • **Tier-1:** provide storage capacity, support for the Grid, safe-keeping of a pro-  
               portional share of raw and reconstructed data, large-scale reprocessing and safe-  
               keeping of corresponding output, generation of simulated events, distribution  
               of data to Tier 2s, safe-keeping of a share of simulated data produced at these  
               Tier 2s.
- 1363     • **Tier-2:** store sufficient data and provide adequate computing power for specific  
               analysis tasks, provide analysis requirements and proportional share of simu-  
               lated event production and reconstruction.

1366 Aside from the general computing strategy to manage the huge amount of data pro-  
1367 duced by experiments, CMS uses a framework to perform a variety of processing,  
1368 selection and analysis tasks. The central concept of the CMS data model referred to  
1369 as *event data model* (EDM) is the *Event*; therefore, an event is the unit that contains  
1370 the information from a single bunch crossing as well as any data derived from that  
1371 information like the reconstructed objects, the details under which additional data  
1372 are derived.

1373

1374 Events are passed as the input to the *physics modules* that obtain information from  
1375 them and create new one; for instance, *event data producers* add new data into the  
1376 events, *analyzers* produce an information summary from an event set, *filters* perform  
1377 selection and triggering.

1378

1379 CMS uses several event formats with different levels of detail and precision

1380 • **Raw format:** events in this format contain the full recorded information from  
1381 the detector as well as trigger decision and other metadata. An extended version  
1382 of raw data is used to store information from the CMS Monte Carlo simulation  
1383 tools. Raw data are stored permanently, occupying about 2MB/event

1384 • **RECO format:** events in this format correspond to raw data that have been  
1385 submitted to reconstruction algorithms like primary and secondary vertex re-  
1386 construction, particle ID, track-finding. RECO events contain physical objects  
1387 and all the information used to reconstruct them; average size is about 0.5  
1388 MB/event.

1389 • **AOD format:** Analysis Object Data (AOD) is the data format used in the  
1390 physics analyses given that it contains the parameters describing the high-level

1391        physics objects in addition to enough information to allow a kinematic refitting if  
 1392        needed. AOD events are filtered versions of the RECO events to which skimming  
 1393        or other kind processes have been applied. Requires about 100 kB/event.

1394        • **Non-event data** are data needed to interpret and reconstruct events. Some  
 1395        of the non-event data used by CMS contains information about the detector  
 1396        contraction and condition data like calibrations, alignment, and detector status.

1397        Figure 3.19 shows the data flow scheme between CMS detector and hardware tiers.

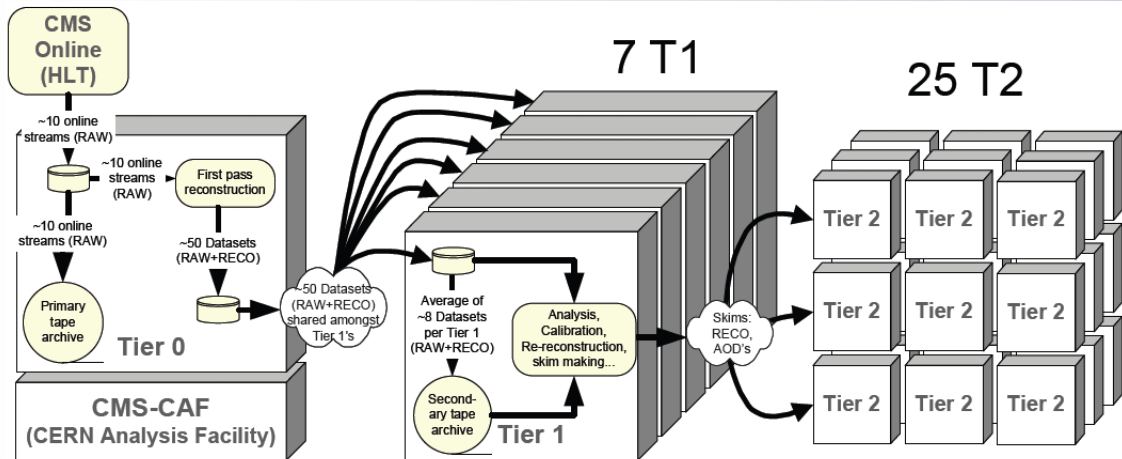


**Figure 3.19:** Data flow from CMS detector through hardware Tiers.

1398        The whole collection of software built as a framework is referred to as *CMSSW*. This  
 1399        framework provides the services needed by the simulation, calibration and alignment,  
 1400        and reconstruction modules that process event data, so that physicists can perform  
 1401        analysis. The CMSSW event processing model is composed of one executable, called  
 1402        cmsRun, and several plug-in modules which contains all the tools (calibration, recon-  
 1403        struction algorithms) needed to process an event. The same executable is used for  
 1404        both detector and Monte Carlo data [79].

1405 **Chapter 4**

1406 **Event generation, simulation and  
1407 reconstruction**

1408 The process of analyzing data recorded by the CMS experiment involves several stages  
1409 where the data are processed in order to interpret the information provided by all  
1410 the detection systems; in those stages, the particles produced after the  $pp$  collision  
1411 are identified by reconstructing their trajectories and measuring their features. In  
1412 addition, the SM provides a set of predictions that have to be compared with the  
1413 experimental results; however, in most of the cases, theoretical predictions are not  
1414 directly comparable to experimental results due to the diverse source of uncertainties  
1415 introduced by the experimental setup and theoretical approximations, among others.

1416

1417 The strategy to face these conditions consists in using statistical methods imple-  
1418 mented in computational algorithms to produce numerical results that can be con-  
1419 trasted with the experimental results. These computational algorithms are commonly  
1420 known as Monte Carlo (MC) methods and, in the case of particle physics, they are  
1421 designed to apply the SM rules and produce predictions about the physical observ-

ables measured in the experiments. Since particle physics is governed by quantum mechanics principles, predictions are not allowed from single events; therefore, a high number of events are *generated* and predictions are produced in the form of statistical distributions for the observables. Effects of the detector presence are included in the predictions by introducing simulations of the detector itself.

1427

1428 This chapter presents a description of the event generation strategy and the tools  
 1429 used to perform the detector simulation and physics objects reconstruction. A com-  
 1430 prehensive review of event generators for LHC physics can be found in Reference [80]  
 1431 on which this chapter is based.

## 1432 4.1 Event generation

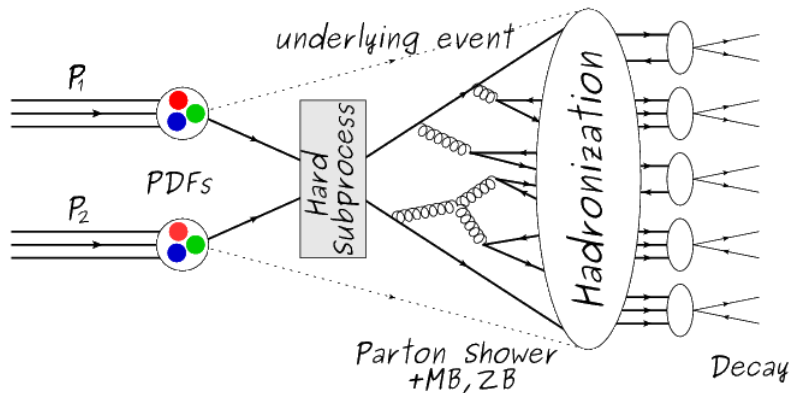


**Figure 4.1:** Event generation process. The actual interaction is generated in the hard subprocess. The parton shower describes the evolution of the partons from the hard subprocess. Modified from Reference [81].

1433 The event generation is intended to create events that mimic the behavior of actual  
 1434 events produced in collisions; they obey a sequence of steps from the particles collision  
 1435 hard process to the decay process into the final state. Figure 4.1 shows a schematic  
 1436 view of the event generation process; the fact that the full process can be treated as

1437 several independent steps is motivated by the QCD factorization theorem.

1438

1439 Generation starts by taking into account the PDFs of the incoming particles. Event  
 1440 generators offer the option to chose from several PDF sets depending on the particu-  
 1441 lar process under simulation<sup>1</sup>; in the following,  $pp$  collisions will be considered. The  
 1442 *hard subprocess* describes the actual interaction between partons from the incoming  
 1443 protons; it is represented by the matrix element connecting the initial and final states  
 1444 of the interaction. Normally, the matrix element can be written as a sum over Feyn-  
 1445 man diagrams and consider interferences between terms in the summation. During  
 1446 the generation of the hard subprocess, the production cross section is calculated.

1447

1448 The order to which the cross section is calculated depends on the order of the Feyn-  
 1449 man diagrams involved in the calculation; therefore, radiative corrections are included  
 1450 by considering a higher order Feynman diagrams where QCD radiation dominates.  
 1451 Currently, cross sections calculated to LO do not offer a satisfactory description of the  
 1452 processes, i.e., the results are only reliable for the shape of distributions; therefore,  
 1453 NLO calculations have to be performed with the implication that the computing time  
 1454 needed is highly increased.

1455

1456 The final parton content of the hard subprocess is subjected to the *parton shower*  
 1457 which generates the gluon radiation. Parton shower evolves the partons, i.e., glouns  
 1458 split into quark-antiquark pairs and quarks with enough energy radiate gluons giv-  
 1459 ing rise to further parton multiplication, following the DGLAP (Dokshitzer-Gribov-  
 1460 Lipatov-Altarelli-Parisi) equations. Showering continues until the energy scale is low  
 1461 enough to reach the non-perturbative limit.

---

<sup>1</sup> Tool in Reference [82] allows to plot different PDF sets under customizable conditions.

1462

1463 In the simulation of LHC processes that involve  $b$  quarks, like the single top quark  
 1464 or Higgs associated production, it is needed to consider that the  $b$  quark is heavier  
 1465 than the proton; hence, the QCD interaction description is made in two different  
 1466 schemes [83]

1467 • four-flavor (4F) scheme.  $b$  quarks appear only in the final state because they  
 1468 are heavier than the proton and therefore they can be produced only from the  
 1469 splitting of a gluon into pairs or singly in association with a  $t$  quark in high  
 1470 energy-scale interactions; furthermore, during the simulation, the  $b$ -PDFs are set  
 1471 to zero. Calculations in this scheme are more complicated due to the presence  
 1472 of the second  $b$  quark but the full kinematics is considered already at LO and  
 1473 therefore the accuracy of the description is better.

1474 • five-flavor (5F) scheme.  $b$  quarks are considered massless, therefore they can  
 1475 appear in both initial and final states since they can now be part of the proton;  
 1476 thus, during the simulation  $b$ -PDFs are not set to zero. In this scheme, calcu-  
 1477 lations are simpler than in the 4F scheme and possible logarithmic divergences  
 1478 are absorbed by the PDFs through the DGLAP evolution.

1479 In this thesis, the  $tHq$  events are generated using the 4F scheme in order to reduce  
 1480 uncertainties, while the  $tHW$  events are generated using the 5F scheme to eliminate  
 1481 LO interference with  $t\bar{t}H$  process [48].

1482

1483 Partons involved in the  $pp$  collision are the focus of the simulation, however, the rest  
 1484 of the partons inside the incoming protons are also affected because the remnants are  
 1485 colored objects; also, multiple parton interactions can occur. The hadronization of  
 1486 the remnants and multiple parton interactions are known as *underlying event* and it

1487 has to be included in the simulation. In addition, multiple  $pp$  collisions in the same  
 1488 bunch crossing (pile-up mentioned in 3.2) occurs, actually in two forms

- 1489     • *in-time PU* which refers to multiple  $pp$  collision in the bunch crossing but that  
 1490       are not considered as primary vertices.
- 1491     • *Out-of-time PU* which refers to overlapping  $pp$  collisions from consecutive bunch  
 1492       crossings; this can occur due to the time-delays in the detection systems where  
 1493       information from one bunch crossing is assigned to the next or previous one.

1494 While the underlying event effects are included in generation using generator-specific  
 1495 tools, PU effects are added to the generation by overlaying Minimum-bias (MB) and  
 1496 Zero-bias (ZB) events to the generated events. MB events are inelastic events se-  
 1497 lected by using a loose trigger with as little bias as possible, therefore accepting a  
 1498 large fraction of the overall inelastic event; ZB events correspond to random events  
 1499 recorded by the detector when collisions are likely. MB models in-time PU and ZB  
 1500 models out-of-time PU.

1501

1502 The next step in the generation process is called *hadronization*. Since particles with  
 1503 a net color charge are not allowed to exits isolated, they have to recombine to form  
 1504 bound states. This is precisely the process by which the partons resulting from the  
 1505 parton shower arrange themselves as color singlets to form hadrons. At this step, the  
 1506 energy-scale is low and the strong coupling constant is large, therefore hadronization  
 1507 process is non-perturbative and the evolution of the partons is described using phe-  
 1508 nomenological models. Most of the baryons and mesons produced in the hadronization  
 1509 are unstable and hence they will decay in the detector.

1510

1511 The last step in the generation process corresponds to the decay of the unstable  
 1512 particles generated during hadronization; it is also simulated in the hadronization  
 1513 step, based on the known branching ratios.

1514 **4.2 Monte Carlo Event Generators.**

1515 The event generation described in the previous section has been implemented in  
 1516 several software packages for which a brief description is given.

1517 • **PYTHIA 8.** It is a program designed to perform the generation of high energy  
 1518 physics events which describes the collisions between particles such as electrons  
 1519 and protons. Several theories and models are implemented in it, in order to  
 1520 describe physical aspects like hard and soft interaction, parton distributions,  
 1521 initial and final-state parton showers, multiple parton interactions, beam rem-  
 1522 nants, hadronization<sup>2</sup> and particle decay. Thanks to extensive testing, several  
 1523 optimized parametrizations, known as *tunings*, have been defined in order to  
 1524 improve the description of actual collisions to a high degree of precision; for  
 1525 analysis at  $\sqrt{s} = 13$  TeV, the underline event CUETP8M1 tune is employed [85].  
 1526 The calculation of the matrix element is performed at LO which is not enough  
 1527 for the current required level of precision; therefore, pythia is often used for  
 1528 parton shower, hadronization and decays, while other event generators are used  
 1529 to generate the matrix element at NLO.

1530 • **MadGraph5\_aMC@NLO.** MadGraph is a matrix element generator which  
 1531 calculates the amplitudes for all contributing Feynman diagrams of a given pro-  
 1532 cess but does not provide a parton shower while MC@NLO incorporates NLO

---

<sup>2</sup> based in the Lund string model [84]

1533 QCD matrix elements consistently into a parton shower framework; thus, Mad-  
 1534 Graph5\_aMC@NLO, as a merger of the two event generators MadGraph5 and  
 1535 aMC@NLO, is an event generator capable to calculate tree-level and NLO cross  
 1536 sections and perform the matching of those with the parton shower. It is one of  
 1537 the most frequently used matrix element generators; however, it has the partic-  
 1538 ular feature of the presence of negative event weights which reduce the number  
 1539 of events used to reproduce the properties of the objects generated [86].

1540

1541 • **POWHEG.** It is an NLO matrix element generator where the hardest emis-  
 1542 sion of color charged particles is generated in such a way that the negative event  
 1543 weights issue of MadGraph5\_aMC@NLO is overcome; however, the method re-  
 1544 quires an interface with  $p_T$ -ordered parton shower or a parton shower generator  
 1545 where this highest emission can be vetoed in order to avoid double counting of  
 1546 this highest-energetic emission. PYTHIA is a commonly matched to POWHEG  
 1547 event generator [87].

1548 Events resulting from the whole generation process are known as MC events.

### 1549 4.3 CMS detector simulation.

1550 After generation, MC events contain the physics of the collisions but they are not  
 1551 ready to be compared to the events recorded by the experiment since these recorded  
 1552 events correspond to the response of the detection systems to the interaction with  
 1553 the particles traversing them. The simulation of the CMS detector has to be applied  
 1554 on top of the event generation; it is simulated with a MC toolkit for the simulation  
 1555 of particles passing through matter called Geant4 which is also able to simulate the

1556 electronic signals that would be measured by all detectors inside CMS.

1557

1558 The simulation takes the generated particles contained in the MC events as input,  
1559 makes them pass through the simulated geometry, and models physics processes that  
1560 particles experience during their passage through matter. The full set of results from  
1561 particle-matter interactions corresponds to the simulated hit which contains informa-  
1562 tion about the energy loss, momentum and position. Particles of the input event are  
1563 called *primary*, while the particles originating from GEANT4-modeled interactions of  
1564 a primary particle with matter are called a *secondary*. Simulated hits are the input  
1565 of subsequent modules that emulate the response of the detector readout system and  
1566 triggers. The output from the emulated detection systems and triggers is known as  
1567 digitization [88,89].

1568

1569 The modeling of the CMS detector corresponds to the accurate modeling of the  
1570 interaction among particles, the detector material, and the magnetic field. This  
1571 simulation procedure includes the following standard steps

1572 • Modeling of the Interaction Region.

1573 • Modeling of the particle passage through the hierarchy of volumes that compose  
1574 CMS detector and of the accompanying physics processes.

1575 • Modeling of the effect of multiple interactions per beam crossing and/or the  
1576 effect of events overlay ( Pile-Up simulation).

1577 • Modeling of the detector's electronics response, signal shape, noise, calibration  
1578 constants (digitization).

1579 In addition to the full simulation, i.e., a detailed detector simulation, a faster simu-  
 1580 lation (FastSim) have been developed, that may be used where much larger statistics  
 1581 are required. In FastSim, detector material effects are parametrized and included in  
 1582 the hits; those hits are used as input of the same higher-level algorithms<sup>3</sup> used to an-  
 1583 alyze the recorded events. In this way, comparisons between fast and full simulations  
 1584 can be performed [91].

1585

1586 After the full detector simulation, the output events can be directly compared to  
 1587 events actually recorded in the CMS detector. The collection of MC events that  
 1588 reproduces the expected physics for a given process is known as MC sample.

## 1589 **4.4 Event reconstruction.**

1590 The CMS experiment use the *particle-flow event reconstruction algorithm (PF)* to do  
 1591 the reconstruction of particles produced in  $pp$  collisions. Next sections will present  
 1592 a basic description of the *Elements* used by PF (tracker tracks, energy clusters, and  
 1593 muon tracks), based in the References [92, 93] where more detailed descriptions can  
 1594 be found.

### 1595 **4.4.1 Particle-Flow Algorithm.**

1596 Each of the several sub detection systems of the CMS detector is dedicated to identify  
 1597 a specific type of particles, i.e., photons and electrons are absorbed by the ECAL  
 1598 and their reconstruction is based on ECAL information; hadrons are reconstructed  
 1599 from clusters in the HCAL while muons are reconstructed from hits in the muon

---

<sup>3</sup> track fitting, calorimeter clustering, b tagging, electron identification, jet reconstruction and calibration, trigger algorithms which will be considered in the next sections

1600 chambers. PF is designed to correlate signals from all the detector layers (tracks and  
 1601 energy clusters) in order to reconstruct and identify each final state particle and its  
 1602 properties as sketched in Figure 4.2.

1603

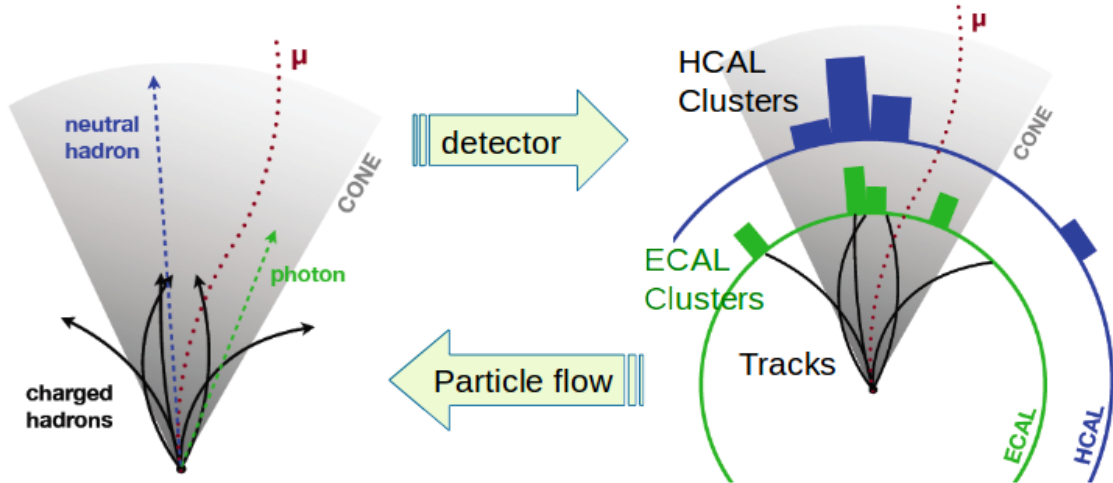


**Figure 4.2:** Particle flow algorithm. Information from the several CMS detection systems is provided as input to the algorithm which then combine it to identify and reconstruct all the particles in the final state and their properties. Reconstruction of simulated events is also performed by providing information from MC samples, detector and trigger simulation [94].

1604 For instance, a charged hadron is identified by a geometrical connection, known as  
 1605 *link*, between one or more calorimeter clusters and a track in the tracker, provided  
 1606 there are no hits in the muon system; combining several measurements allows a better  
 1607 determination of the energy and charge sign of the charged hadron.

### 1608 Charged-particle track reconstruction.

1609 The strategy used by PF in order to reconstruct tracks is called *Iterative Tracking*  
 1610 which occurs in four steps

- 1611 • Seed generation where initial track candidates are found by looking for a combi-  
 1612 nation of hits in the pixel detector, strip tracker, and muon chambers. In total

1613        ten iterations are performed, each one with a different seeding requirement.  
 1614        Seeds are used to estimate the trajectory parameters and uncertainties at the  
 1615        time of the full track reconstruction. Seeds are also considered track candidates.

- 1616        • Track finding using a tracking software known as Combinatorial Track Finder  
                   (CTF) [95]. The seed trajectories are extrapolated along the expected flight  
                   path of a charged particle, in agreement to the trajectory parameters obtained  
                   in the first step, in an attempt to find additional hits that can be assigned to  
                   the track candidates.
- 1621        • Track-fitting where the found tracks are passed as input to a module which  
                   provides the best estimate of the parameters of each trajectory.
- 1623        • Track selection where track candidates are submitted to a selection which dis-  
                   cards those that fail a set of defined quality criteria.

1625        Iterations differ in the seeding configuration and the final track selection as elaborated  
 1626        in References [92, 93]. In the first iteration, high  $p_T$  tracks and tracks produced near  
 1627        to the interaction region are identified and those hits are masked thereby reducing  
 1628        the combinatorial complexity. Next, iterations search for more complicated tracks,  
 1629        like low  $p_T$  tracks and tracks from b hadron decays, which tend to be displaced from  
 1630        the interaction region.

1631        **Vertex reconstruction.**

1632        During the track reconstruction, an extrapolation toward to the calorimeters is per-  
 1633        formed in order to match energy deposits; that extrapolation is performed also toward  
 1634        the beamline in order to find the origin of the track known as *vertex*. The vertex re-  
 1635        construction is performed by selecting from the available reconstructed tracks, those

1636 that are consistent with being originated in the interaction region where  $pp$  collisions  
 1637 are produced. The selection involves a requirement on the number of tracker (pixel  
 1638 and strip) hits and the goodness of the track fit.

1639

1640 Selected tracks are clustered using a *deterministic annealing algorithm* (DA)<sup>4</sup>. A set  
 1641 of candidate vertices and their associated tracks, resulting from the DA, are then fit-  
 1642 ted with an *adaptive vertex fitter* (AVF) to produce the best estimate of the vertices  
 1643 locations.

1644

1645 The  $p_T$  of the tracks associated to a reconstructed vertex is added, squared and used  
 1646 to organize the vertices; the vertex with the highest squared sum is designated as the  
 1647 *primary vertex* (PV) while the rest are designated as PU vertices.

#### 1648 **Calorimeter clustering.**

1649 After traversing the CMS tracker system, electrons, photons and hadrons deposit their  
 1650 energy in the ECAL and HCAL cells. The PF clustering algorithm aims to provide  
 1651 a high detection efficiency even for low-energy particles and an efficient distinction  
 1652 between close energy deposits. The clustering runs independently in the ECAL barrel  
 1653 and endcaps, HCAL barrel and endcaps, and the two preshower layers, following two  
 1654 steps

- 1655     ● cells with an energy larger than a given seed threshold and larger than the energy  
       1656       of the neighboring cells are identified as cluster seeds. The neighbor cells are  
       1657       those that either share a side with the cluster seed candidate, or the eight closest  
       1658       cells including cells that only share a corner with the seed candidate.

---

<sup>4</sup> DA algorithm and AVF are described in detail in References [97, 98]

1659       • cells with at least a corner in common with a cell already in the cluster seed  
 1660           and with an energy above a cell threshold are grouped into topological clusters.

1661     Clusters formed in this way are known as *particle-flow clusters*. With this clustering  
 1662   strategy, it is possible to detect and measure the energy and direction of photons and  
 1663   neutral hadrons as well as differentiate these neutral particles from the charged hadron  
 1664   energy deposits. In cases involving charged hadrons for which the track parameters  
 1665   are not determined accurately, for instance, low-quality and high- $p_T$  tracks, clustering  
 1666   helps in the energy measurements.

1667 **Electron track reconstruction.**

1668   Although the charged-particle track reconstruction described above works for elec-  
 1669   trons, they lose a significant fraction of their energy via bremsstrahlung photon radi-  
 1670   ation before reaching the ECAL; thus, the reconstruction performance depends on the  
 1671   ability to measure also the radiated energy. The reconstruction strategy, in this case,  
 1672   requires information from the tracking system and from the ECAL. Bremsstrahlung  
 1673   photons are emitted at similar  $\eta$  values to that of the electron but at different values  
 1674   of  $\phi$ ; therefore, the radiated energy can be recovered by grouping ECAL clusters in a  
 1675    $\eta$  window over a range of  $\phi$  around the electron direction. The group is called ECAL  
 1676   supercluster.

1677

1678   Electron candidates from the track-seeding and ECAL super clustering are merged  
 1679   into a single collection which is submitted to a full electron tracking fit with a  
 1680   Gaussian-sum filter (GSF) [96]. The electron track and its associated ECAL su-  
 1681   percluster form a *particle-flow electron*.

1682 **Muon track reconstruction.**

1683 Given that the CMS detector is equipped with a muon spectrometer capable to iden-  
 1684 tify and measure the momentum of the muons traversing it, the muon reconstruction  
 1685 is not specific to PF; therefore, three different muon types are defined

- 1686     • *Standalone muon.* A clustering on the DTs or CSCs hits is performed to form  
   1687       track segments; those segments are used as seeds for the reconstruction in the  
   1688       muon spectrometer. All DTs, CSCs, and RPCs hits along the muon trajectory  
   1689       are combined and fitted to form the full track. The fitting output is called a  
   1690       *standalone-muon track*.
- 1691     • *Tracker muon.* Each track in the inner tracker with  $p_T$  larger than 0.5 GeV and  
   1692       a total momentum  $p$  larger than 2.5 GeV is extrapolated to the muon system.  
   1693       A *tracker muon track* corresponds to a extrapolated track that matches at least  
   1694       one muon segment.
- 1695     • *Global muon.* When tracks in the inner tracker (inner tracks) and standalone-  
   1696       muon tracks are matched and turn out being compatibles, their hits are com-  
   1697       bined and fitted to form a *global-muon track*.

1698 Global muons sharing the same inner track with tracker muons are merged into a  
 1699 single candidate. PF muon identification uses the muon energy deposits in ECAL,  
 1700 HCAL, and HO associated with the muon track to improve the muon identification.

1701 **Particle identification and reconstruction.**

1702 PF elements are connected by a linker algorithm that tests the connection between any  
 1703 pair of elements; if they are found to be linked, a geometrical distance that quantifies  
 1704 the quality of the link is assigned. Two elements may be linked indirectly through

1705 common elements. Linked elements form *PF blocks* and each PF block may contain  
 1706 elements originating in one or more particles. Links can be established between  
 1707 tracks, between calorimeter clusters, and between tracks and calorimeter clusters.  
 1708 The identification and reconstruction start with a PF block and proceed as follows

1709 • Muons. An *isolated global muon* is identified by evaluating the presence of  
 1710 inner track and energy deposits close to the global muon track in the  $(\eta, \phi)$   
 1711 plane, i.e., in a particular point of the global muon track, inner tracks and  
 1712 energy deposits are sought within a radius of  $\Delta R = 0.3$  (see eqn. 3.7) from the  
 1713 muon track; if they exit and the  $p_T$  of the found track added to the  $E_T$  of the  
 1714 found energy deposit does not exceed 10% of the muon  $p_T$  then the global muon  
 1715 is an isolated global muon. This isolation condition is stringent enough to reject  
 1716 hadrons misidentified as muons.

1717 *Non-isolated global muons* are identified using additional selection requirements  
 1718 on the number of track segments in the muon system and energy deposits along  
 1719 the muon track. Muons inside jets are identified with more stringent criteria  
 1720 in isolation and momentum as described in Reference [99]. The PF elements  
 1721 associated with an identified muon are masked from the PF block.

1722 • Electrons are identified and reconstructed as described above plus some addi-  
 1723 tional requirements on fourteen variables like the amount of energy radiated,  
 1724 the distance between the extrapolated track position at the ECAL and the po-  
 1725 sition of the associated ECAL supercluster, among others, which are combined  
 1726 in an specialized multivariate analysis strategy that improves the electron iden-  
 1727 tification. Tracks and clusters used to identify and reconstruct electrons are  
 1728 masked in the PF block.

- 1729     ● Isolated photons are identified from ECAL superclusters with  $E_T$  larger than 10  
 1730       GeV, for which the energy deposited at a distance of 0.15, from the supercluster  
 1731       position on the  $(\eta,\phi)$  plane, does not exceed 10% of the supercluster energy;  
 1732       note that this is an isolation requirement. In addition, there must not be links  
 1733       to tracks. Clusters involved in the identification and reconstruction are masked  
 1734       in the PF block.
  
- 1735     ● Bremsstrahlung photons and prompt photons tend to convert to electron-positron  
 1736       pairs inside the tracker, therefore, a dedicated finder algorithm is used to link  
 1737       tracks that seem to originate from a photon conversion; in case those two tracks  
 1738       are compatible with the direction of a bremsstrahlung photon, they are also  
 1739       linked to the original electron track. Photon conversion tracks are also masked  
 1740       in the PF block.
  
- 1741     ● The remaining elements in the PF block are used to identify hadrons. In the  
 1742       region  $|\eta| \leq 2.5$ , neutral hadrons are identified with HCAL clusters not linked  
 1743       to any track while photons from neutral pion decays are identified with ECAL  
 1744       clusters without links to tracks. In the region  $|\eta| > 2.5$  ECAL clusters linked to  
 1745       HCAL clusters are identified with a charged or neutral hadron shower; ECAL  
 1746       clusters with no links are identified with photons. HCAL clusters not used yet,  
 1747       are linked to one or more unlinked tracks and to an unlinked ECAL in order to  
 1748       reconstruct charged-hadrons or a combination of photons and neutral hadrons  
 1749       according to certain conditions on the calibrated calorimetric energy.
  
- 1750     ● Charged-particle tracks may be liked together when they converge to a *sec-  
 1751       ondary vertex (SV)* displaced from the interaction point where the PV and PU  
 1752       vertices are reconstructed; at least three tracks are needed in that case, of which  
 1753       at most one has to be an incoming track with hits in tracker region between a

1754 PV and the SV.

1755

1756 The linker algorithm, as well as the whole PF algorithm, has been validated and  
 1757 commissioned; results from that validation are presented in the Reference [92].

1758 **Jet reconstruction.**

1759 Quarks and gluons may be produced in the  $pp$  collisions, therefore, their hadronization  
 1760 will be seen in the detector as a shower of hadrons and their decay products in the  
 1761 form of a *jet*. The anti- $k_t$  algorithm [100] is used to perform the jet reconstruction  
 1762 by clustering those PF particles within a cone (see Figure 4.3); previously, isolated  
 1763 electrons, isolated muons, and charged particles associated with other interaction  
 1764 vertices are excluded from the clustering.

1765 The anti- $k_t$  algorithm proceeds in a sequential recombination of PF particles; the  
 1766 distance between particles  $i$  and  $j$  ( $d_{ij}$ ) and the distance between particles and the  
 1767 beam are defined as

$$d_{ij} = \min\left(\frac{1}{k_{ti}^2}, \frac{1}{k_{tj}^2}\right) \frac{\Delta_{ij}^2}{R^2}$$

$$d_{iB} = \frac{1}{k_{ti}^2} \quad (4.1)$$

1768 where  $\Delta_{ij}^2 = (y_i - y_j)^2 + (\phi_i - \phi_j)^2$ ,  $k_{ti}, y_i$  and  $\phi_i$  are the transverse momentum, ra-  
 1769 pidity and azimuth of particle  $i$  respectively and  $R$  is the called jet radius. For all  
 1770 the remaining PF particles, after removing the isolated ones,  $d_{ij}$  and  $d_{iB}$  are calcu-  
 1771 lated<sup>5</sup> and the smallest is identified; if it is a  $d_{ij}$ , particles  $i$  and  $j$  are replaced with

---

<sup>5</sup> Notice that this is a combinatorial calculation.

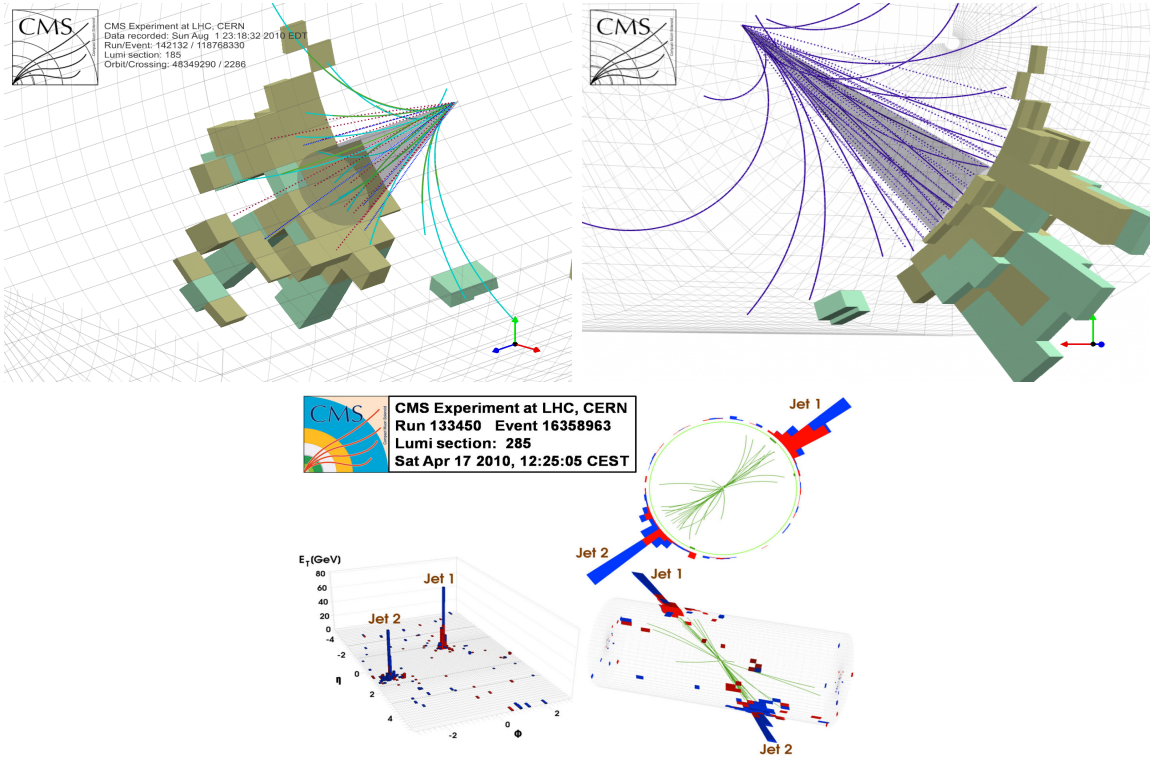


**Figure 4.3:** Jet reconstruction performed by the anti- $k_t$  algorithm. Top: Two different views of a CMS recorded event are presented. Continuous lines correspond to tracks left by charged particles in the tracker while dotted lines are the imaginary paths followed by neutral particles. The green cubes represent the ECAL cells while the blue ones represent the HCAL cells; in both cases, the height of the cube represent the amount of energy deposited in the cells [101]. Bottom: Reconstruction of a recorded event with two jets [102].

1772 a new object whose momentum is the vectorial sum of the combined particles. If the  
 1773 smallest distance is a  $d_{iB}$  the clustering process ends, the object  $i$  (which at this stage  
 1774 should be a combination of several PF particles) is declared as a *Particle-flow-jet* (PF  
 1775 jet) and all the associated PF particles are removed from the detector. The clustering  
 1776 process is repeated until no PF particles remain.

1777 Even though jets can be reconstructed efficiently, there are some effects that are not in-  
 1778 cluded in the reconstruction and that lead to discrepancies between the reconstructed  
 1779 results and the predicted results; in order to overcome these discrepancies, a factor-  
 1780 ized model has been designed in the form of jet energy corrections (JEC) [103, 104]

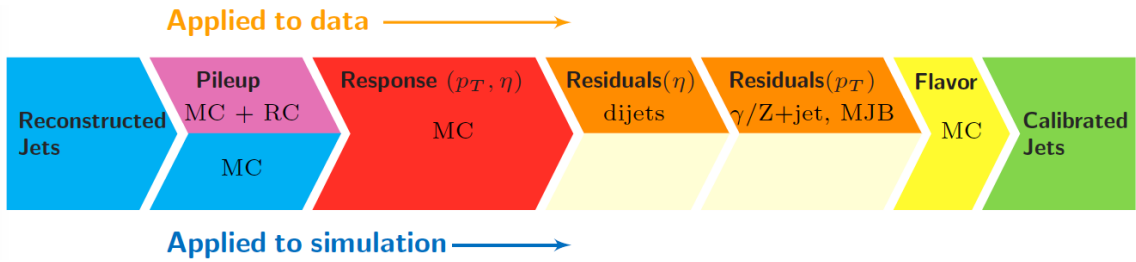


**Figure 4.4:** Jet energy correction diagram. Correction levels are applied sequentially in the indicated fixed order [104].

1781 applied sequentially as shown in the diagram of Figure 4.4.

1782 At each level, the jet four-momentum is multiplied by a scaling factor based on jet  
1783 properties, i.e.,  $\eta$ , flavor, etc.

1784 • Level 1 correction removes the energy coming from pile-up. The scale factor is  
1785 determined using a MC sample of QCD dijet (2 jets) events with and without  
1786 pileup overlay; it is parametrized in terms of the offset energy density  $\rho$ , jet  
1787 area  $A$ , jet  $\eta$  and jet  $p_T$ . Different corrections are applied to data and MC due  
1788 to the detector simulation.

1789 • MC-truth correction accounts for differences between the reconstructed jet en-  
1790 ergy and the MC particle-level energy. The correction is determined on a QCD  
1791 dijet MC sample and is parametrized in terms of the jet  $p_T$  and  $\eta$ .

1792 • Residuals correct remaining small differences within jet response in data and  
1793 MC. The Residuals  $\eta$ -dependent correction compares jets of similar  $p_T$  in the  
1794 barrel reference region. The Residuals  $p_T$ -dependent correct the jet absolute  
1795 scale (JES vs  $p_T$ ).

1796 • Jet-flavor corrections are derived in the same way as MC-truth corrections but  
1797 using QCD pure flavor samples.

1798 ***b*-tagging of jets.**

1799 A particular feature of the hadrons containing bottom quarks (*b*-hadrons) is that  
 1800 their lifetime is long enough to travel some distance before decaying, but it is not as  
 1801 long as those of light quark hadrons; therefore, when looking at the hadrons produced  
 1802 in  $pp$  collisions, *b*-hadrons decay typically inside the tracker rather than reaching the  
 1803 calorimeters as some light-hadrons do. As a result, a *b*-hadron decay gives rise to a  
 1804 displaced vertex (secondary vertex) with respect to the primary vertex as shown in  
 1805 Figure 4.5; the SV displacement is in the order of a few millimeters. A jet resulting  
 1806 from the decay of a *b*-hadron is called *b* jet; other jets are called light jets.

1807

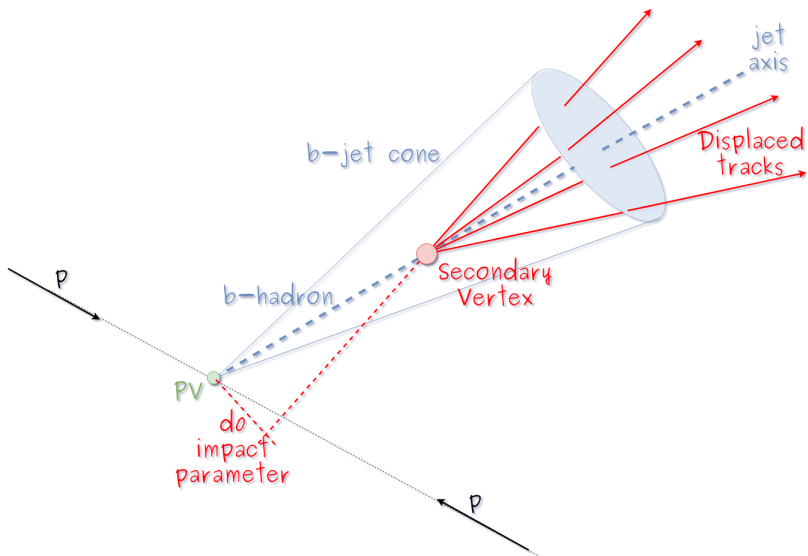


**Figure 4.5:** Secondary vertex in a *b*-hadron decay.

1808 Several methods to identify *b*-jets (*b*-tagging) have been developed; the method used  
 1809 in this thesis is known as *Combined Secondary Vertex* algorithm in its second version  
 1810 (CSVv2) [105]. By using information of the impact parameter, the reconstructed  
 1811 secondary vertices, and the jet kinematics as input in a multivariate analysis that  
 1812 combines the discrimination power of each variable in one global discriminator vari-

able, three working points (references): loose, medium and tight, are defined which quantify the probabilities of mistag jets from light quarks as jets from  $b$  quarks; 10, 1 and 0.1 % respectively. Although the mistagging probability decreases with the working point strength, the efficiency to correctly tag  $b$ -jets also decreases as 83, 69 and 49 % for the respective working point; therefore, a balance needs to be achieved according to the specific requirements of the analysis.

#### 4.4.1.1 Missing transverse energy.

The fact that proton bunches carry momentum along the  $z$ -axis implies that for each event it is expected that the momentum in the transverse plane is balanced. Imbalances are quantified by the missing transverse energy (MET) and are attributed to several sources including particles escaping undetected through the beam pipe, neutrinos produced in weak interactions processes which do not interact with the detector and thus escaping without leaving a sign, or even undiscovered particles predicted by models beyond the SM.

1827

1828 The PF algorithm assigns the negative sum of the momenta of all reconstructed PF  
1829 particles to the *particle-flow MET* according to

$$\vec{E}_T = - \sum_i \vec{p}_{T,i} \quad (4.2)$$

1830 JEC are propagated to the calculation of the  $\vec{E}_T$  as described in the Reference [106].

1831

1832 **4.4.2 Event reconstruction examples**

1833 Figures 4.6-4.8 show the results of the reconstruction performed on 3 recorded events.

1834 Descriptions are taken directly from the source.

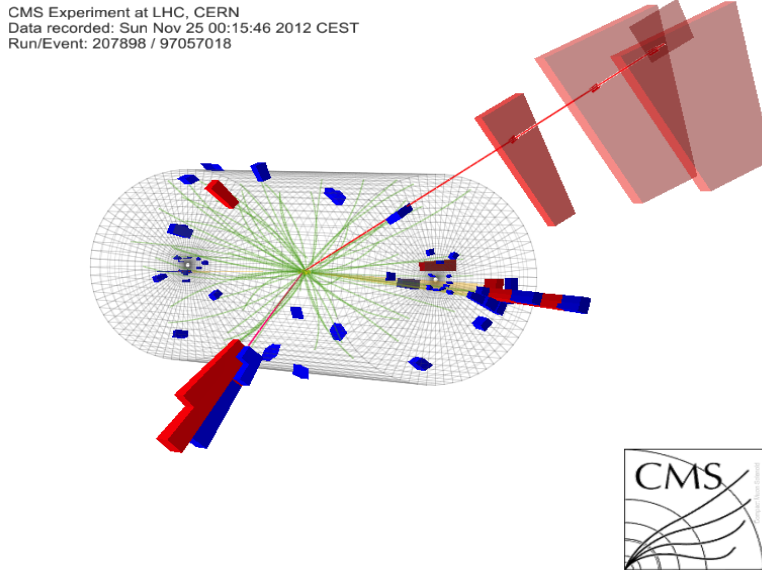


**Figure 4.6:** HIG-13-004 Event 1 reconstruction results; “HIG-13-004 Event 1: Event recorded with the CMS detector in 2012 at a proton-proton center-of-mass energy of 8 TeV. The event shows characteristics expected from the decay of the SM Higgs boson to a pair of  $\tau$  leptons. Such an event is characterized by the production of two forward-going jets, seen here in opposite endcaps. One of the  $\tau$  decays to a muon (red lines on the right) and neutrinos, while the other  $\tau$  decays into a charged hadron and a neutrino.” [107].

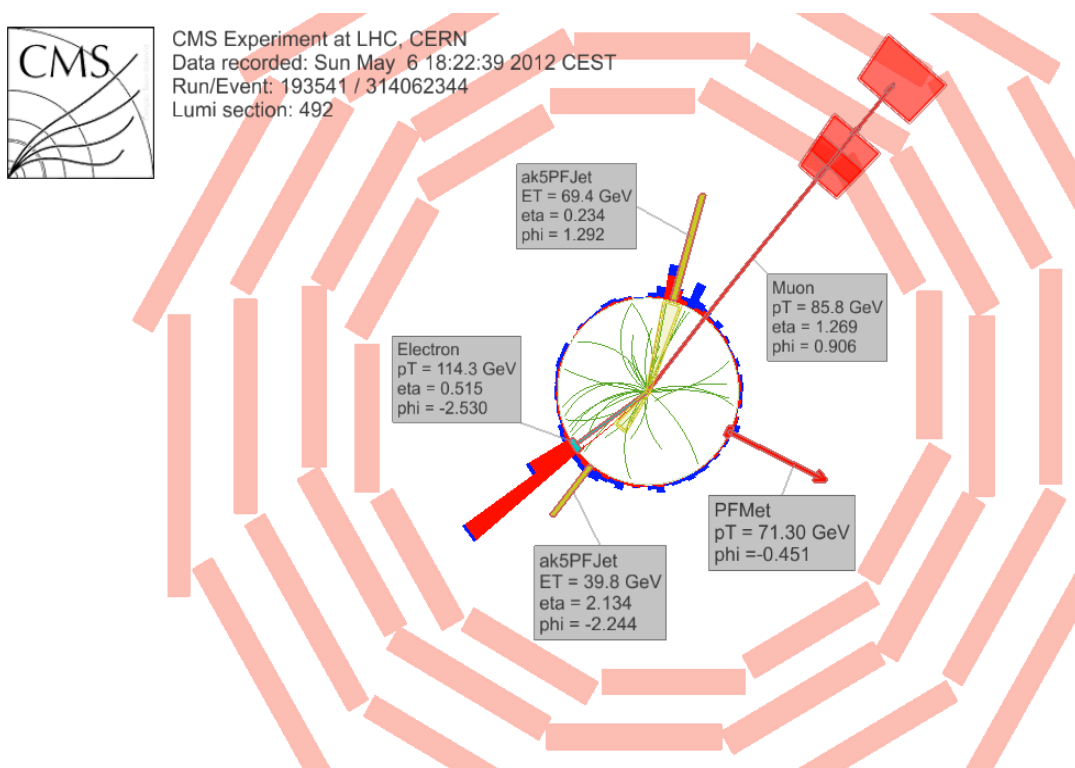


**Figure 4.7:**  $e\mu$  event reconstruction results; “An  $e\mu$  event candidate selected in 8 TeV data, as seen from the direction of the proton beams. The kinematics of the main objects used in the event selection are highlighted: two isolated leptons and two particle-flow jets. The reconstructed missing transverse energy is also displayed for reference” [108].

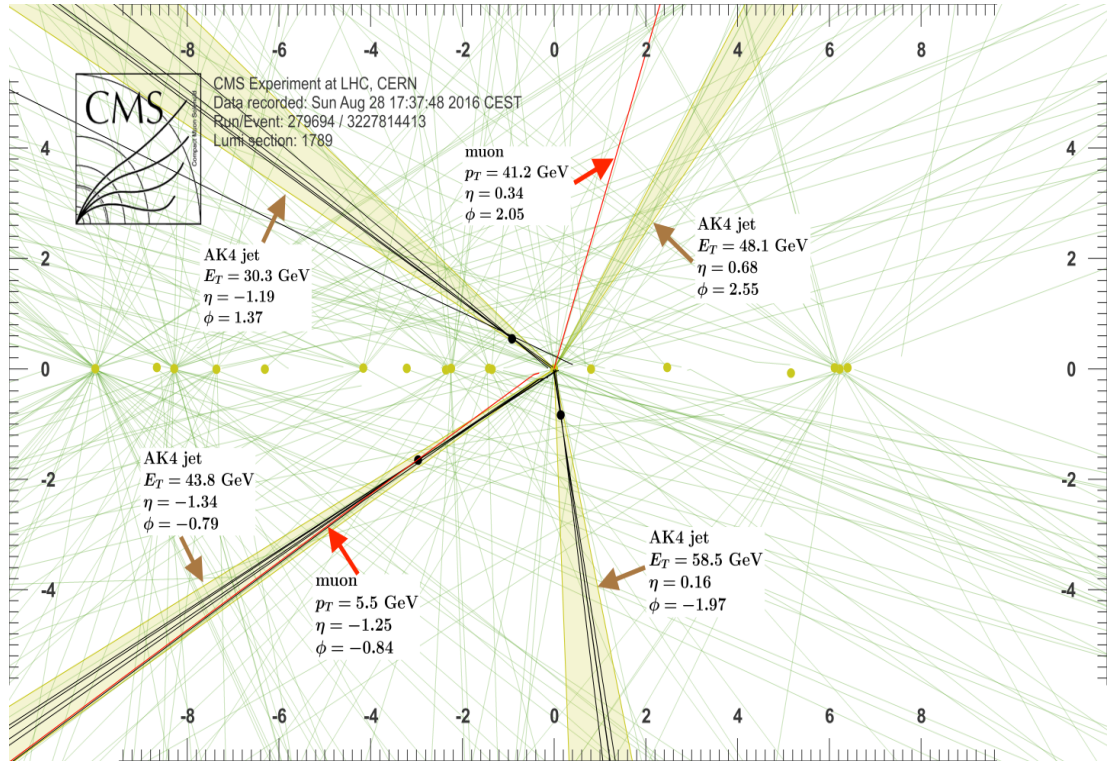


**Figure 4.8:** Recorded event reconstruction results;“Recorded event ( $\rho$ - $z$  projection) with three jets with  $p_T > 30$  GeV with one displaced muon track in 2016 data collected at 13 TeV. Each of the three jets has a displaced reconstructed vertex. The jet with  $p_T(j) = 43.8$  GeV,  $\eta(j) = -1.34$ ,  $\phi(j) = -0.79$  contains muon with  $p_T(\mu) = 5.5$  GeV,  $\eta(\mu) = -1.25$ ,  $\phi(\mu) = -0.84$ . Event contains reconstructed isolated muon with  $p_T(\mu) = 41.2$  GeV,  $\eta(\mu) = 0.34$ ,  $\phi(\mu) = 2.05$  and MET with  $p_T = 72.5$  GeV,  $\phi = -0.32$ . Jet candidates for a  $b$ -jet from top quark leptonic and hadronic decays are tagged by CSVv2T algorithm. One of the other two jets is tagged by CharmT algorithm. Tracks with  $p_T > 0.5$  GeV are shown. The number of reconstructed primary vertices is 18. Reconstructed  $m_T(W)$  is 101.8 GeV. Beam spot position correction is applied. Reconstructed primary vertices are shown in yellow color, while reconstructed displaced vertices and associated tracks are presented in black color. Dimensions are given in cm” [109].

1835 **Chapter 5**

1836 **Statistical methods**

1837 In the course of analyzing the data sets provided by the CMS experiment and used in  
1838 this thesis, several statistical tools have been employed; in this chapter, a description  
1839 of these tools will be presented, starting with the general statement of the multivariate  
1840 analysis method, followed by the particularities of the Boosted Decision Trees (BDT)  
1841 method and its application to the classification problem. Statistical inference methods  
1842 used will also be presented. This chapter is based mainly on the references [110–112].

1843 **5.1 Multivariate analysis**

1844 Multivariate data analysis (MVA) makes reference to statistical techniques that an-  
1845 alyze data containing information of more than one variable, commonly taking into  
1846 account the effects of all variables on the response of the particular variable under  
1847 investigation, i.e., considering all the correlations between variables. MVA is em-  
1848 ployed in a variety of fields like consumer and market research, quality control and  
1849 process optimization. From a MVA it is possible to identify the dominant patterns  
1850 in the data, like groups, outliers and trends, and determine to which group a set of

1851 values belong; in the particle physics context, MVA methods are used to perform the  
 1852 selection of certain type of events, from a large data set, using a potentially large  
 1853 number of measurable properties for each event.

1854 Processes with small cross section, as the  $tHq$  process, normally are hidden behind  
 1855 more common processes; therefore, the data set results in a subset of events with  
 1856 characteristic features of interest (signal) mixed in randomly with a much larger  
 1857 number of SM events that can mimic these features of interest (background) which  
 1858 implies that it is not possible to say with certainty that a given event is signal or  
 1859 background. In that sense, the problem can be formulated as one where a set of  
 1860 events have to be classified according to some features; these features correspond to  
 1861 the measurements of several parameters like energy or momentum, organized in a  
 1862 set of *input variables*. The measurements for each event can be written in a vector  
 1863  $\mathbf{x} = (x_1, \dots, x_n)$  for which

- 1864     • Signal hypotheses  $\rightarrow f(\mathbf{x}|s)$  is the probability density (*likelihood function*) that  
   1865        $\mathbf{x}$  is the set of measured values given that the events is a signal event.
- 1866     • Background hypotheses  $\rightarrow f(\mathbf{x}|b)$  is the probability density (*likelihood function*)  
   1867       that  $\mathbf{x}$  is the set of measured values given that the event is a background event.

1868     Figure 5.1 shows three ways to perform a classification of events for which mea-  
 1869       surements of two properties, two input variables, have been performed; blue circles  
 1870       represent signal events while red triangles represent background events. The classi-  
 1871       fication on (a) is *cut-based* requiring  $x_1 < c_1$  and  $x_2 < c_2$ ; usually the cut values are  
 1872       chosen according to some knowledge about the event process. In (b), the classification  
 1873       is performed by stating a cut involving a linear function of the input variables and  
 1874       so the boundary, while in (c) the the relationship between the input variables is not  
 1875       linear thus the boundary is not linear either.

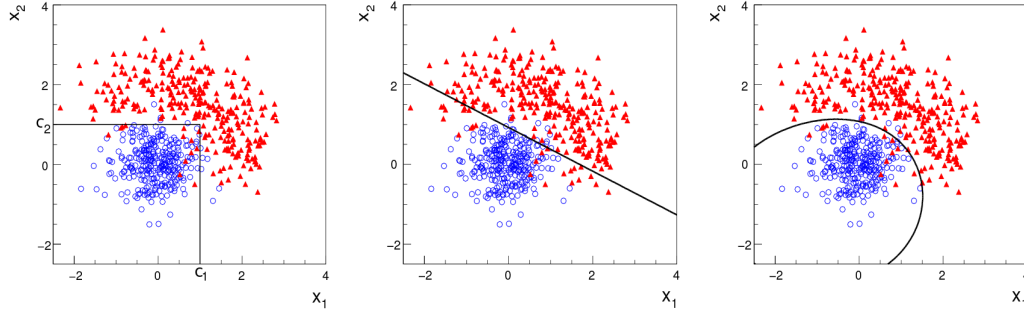


**Figure 5.1:** Scatter plots-MVA event classification. Distribution of two input variables  $x_1$  and  $x_2$  measured for a set of events; blue circles represent signal events and red triangles represent background events. The classification is based on (a) cuts, (b) linear boundary, and (c) nonlinear boundary [110]

1876        The boundary can be parametrized in terms of the input variables such that the  
 1877        cut is set on the parametrization instead of on the variables, i.e.,  $y(\mathbf{x}) = y_{cut}$  with  
 1878         $y_{cut}$  a constant; thus, the acceptance or rejection of an event is based on what side  
 1879        of the boundary is the event located. If  $y(\mathbf{x})$  has functional form, it can be used to  
 1880        determine the probability distribution functions  $p(y|s)$  and  $p(y|b)$  and then perform  
 1881        a scalar test statistic with a single cut on the scalar variable  $y$ .

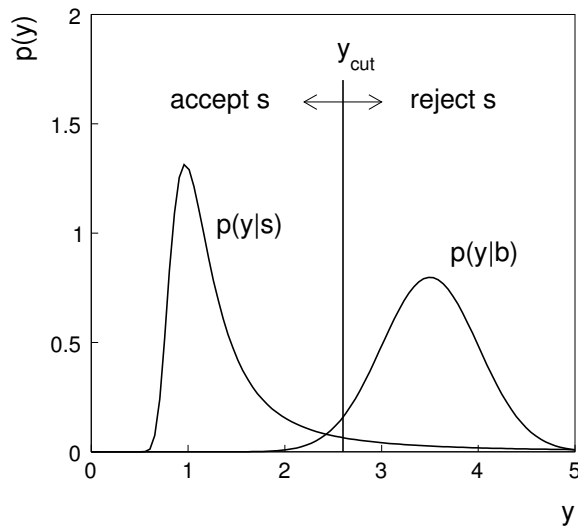


**Figure 5.2:** Distributions of the scalar test statistic  $y(\mathbf{x})$  under the signal and background hypotheses. [110]

1882       Figure 5.2 illustrates what would be the probability distribution functions under  
 1883   the signal and background hypotheses for a scalar test statistic with a cut on the  
 1884   classifier  $y$ . Notice that the tails of the distributions indicate that some signal events  
 1885   fall on the rejection region and some background events fall on the acceptance region;  
 1886   therefore, it is convenient to define the *efficiency* with which events of a given type  
 1887   are accepted, thus, the signal and background efficiencies are given by

$$\varepsilon_s = P(\text{accept event}|s) = \int_A f(\mathbf{x}|s) d\mathbf{x} = \int_{-\infty}^{y_{\text{cut}}} p(y|s) dy , \quad (5.1)$$

$$\varepsilon_b = P(\text{accept event}|b) = \int_A f(\mathbf{x}|b) d\mathbf{x} = \int_{-\infty}^{y_{\text{cut}}} p(y|b) dy , \quad (5.2)$$

1888   where  $A$  is the acceptance region. Under these conditions, the background hypothesis  
 1889   corresponds to the *null hypothesis* ( $H_0$ ), the signal hypothesis corresponds to the  
 1890   *alternative hypothesis* ( $H_1$ ), the background efficiency is the significance level of the  
 1891   test, and signal efficiency is the power of the test; what is sought in an analysis is to  
 1892   maximize the power of the test relative to the significance level.

### 1893 5.1.1 Decision trees

1894   For this thesis, the implementation of the MVA strategy, described above, is per-  
 1895   formed through decision trees by using the TMVA software package [111] included in  
 1896   the the ROOT analysis framework [113]. In a simple picture, a decision tree classifies  
 1897   events according to their input variables values by setting a cut on each input variable  
 1898   and checking which events are on which side of the cut, just as proposed in the MVA  
 1899   strategy, but in addition, as a machine learning algorithm, decision trees offer the  
 1900   possibility to be trained and then perform the classification efficiently.

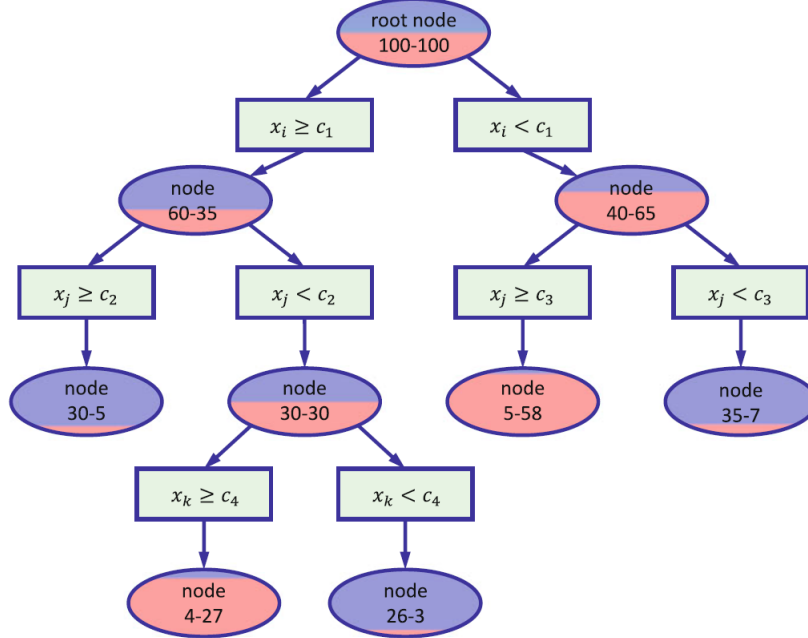


**Figure 5.3:** Example of a decision tree. Each node is fed with a MC sample mixing signal and background events (left-right numbers); nodes colors represent the relative amount of signal/background events [112].

1901        The training or growing of a decision tree is the process that defines the rules for  
 1902        classifying events; this process is represented in figure 5.3 and consist of several steps

1903        • take MC samples of signal and background events and split them into two parts  
 1904        each; first parts form the training sample which will be used in the decision tree  
 1905        training, while the second parts form the test sample which will be used for  
 1906        testing the final classifier obtained from the training. Each event has associated  
 1907        a set of input variables  $\mathbf{x} = (x_1, \dots, x_n)$  which serve to distinguish between signal  
 1908        and background events. The training sample is taken in at the root *node*.

1909        • pick one variable, say  $x_i$   
 1910        • pick one value of  $x_i$ , each event has its own value of  $x_i$ , and split the training  
 1911        sample into two subsamples  $B_1$  and  $B_2$ ;  $B_1$  contains events for which  $x_i < c_1$

1912 while  $B_2$  contains the rest of the training events;

1913 • scan all possible values of  $x_i$  and find the splitting value that provides the *best*  
 1914 classification<sup>1</sup>, i.e.,  $B_1$  is mostly made of signal events while  $B_2$  is mostly made  
 1915 of background events.

1916 • It is possible that variables other than the picked one produce a better classi-  
 1917 fication, hence, all the variables have to be evaluated. Pick the next variable,  
 1918 say  $x_j$ , and repeat the scan over its possible values.

1919 • At the end, all the variables and their values will have been scanned, the *best*  
 1920 variable and splitting value will have been identified, say  $x_1, c_1$ , and there will  
 1921 be two nodes fed with the subsamples  $B_1$  and  $B_2$ .

1922 Nodes are further split by repeating the decision process until: a given number of  
 1923 final nodes is obtained, nodes are largely dominated by either signal or background  
 1924 events, or nodes has too few events to continue. Final nodes are called *leaves* and they  
 1925 are classified as signal or background leaves according to the class of the majority of  
 1926 events in them. Each *branch* in the tree corresponds to a sequence of cuts.

1927 The quality of the classification at each node is evaluated through a separation  
 1928 criteria; there are several of them but the *Gini Index* ( $G$ ) is the one used in the  
 1929 decision trees trained for the analysis in this thesis.  $G$  is written in terms of the  
 1930 purity ( $P$ ), i.e. the fraction of signal events, of the samples after the separation is  
 1931 made; it is given by

$$G = P(1 - P) \quad (5.3)$$

---

<sup>1</sup> Quality of the classification will be treated in the next paragraph.

1932 notice that  $P=0.5$  at the root node while  $G=0$  for pure leaves. For a node  $A$  split  
 1933 into two nodes  $B_1$  and  $B_2$  the G gain is

$$\Delta G = G(A) - G(B_1) - G(B_2) \quad (5.4)$$

1934 the *best* classification corresponds to that for which the gain of G is maximized; hence,  
 1935 the scanning over all event's variables and their values is of capital importance.

1936 In order to provide a numerical output for the classification, events in a sig-  
 1937 nal(background) leaf are assigned an score of 1(-1) each, defining in this way the  
 1938 decision tree *classifier or weak learner* as

$$f(\mathbf{x}) = \begin{cases} 1 & \mathbf{x} \text{ in signal region,} \\ -1 & \mathbf{x} \text{ in background region.} \end{cases}$$

1939 Figure 5.4 shows an example of the classification of a sample of events, containing  
 1940 two variables, performed by a decision tree.

### 1941 5.1.2 Boosted decision trees (BDT).

1942 Event misclassification occurs when a training event ends up in the wrong leaf, i.e., a  
 1943 signal event ends up in a background leaf or a background event ends up in a signal  
 1944 leaf. A way to correct it is to assign a weight to the misclassified events and train  
 1945 a second tree using the reweighted events; the event reweighting is performed by a  
 1946 boosting algorithm, events with increased weight are known as *boosted* events, in such  
 1947 a way that when used in the training of a new decision tree they get correctly classified.  
 1948 The process is repeated iteratively adding a new tree to a forest and creating a set  
 1949 of classifiers which are combined to create the next classifier; the final classifier offers

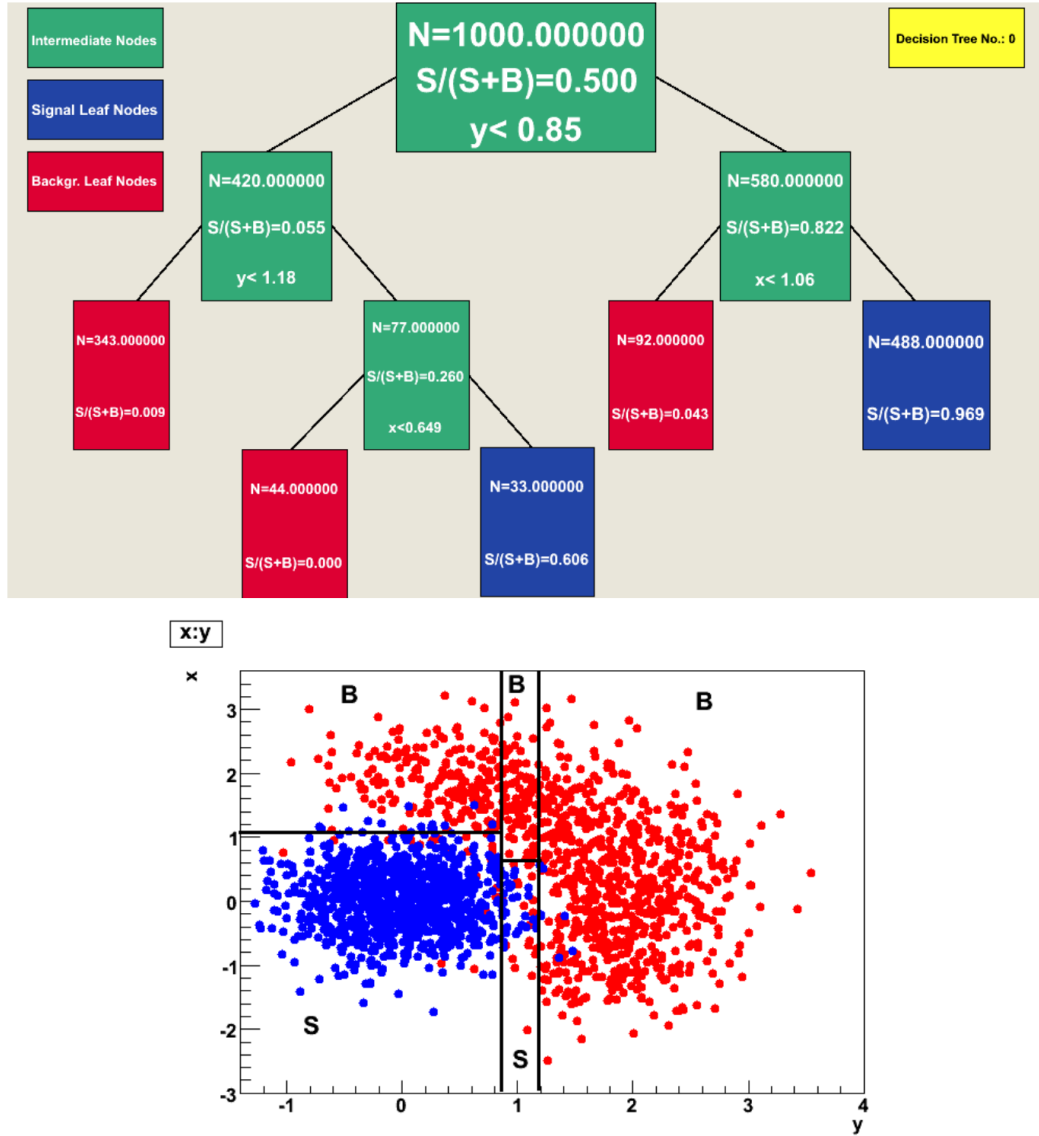


**Figure 5.4:** Example of a decision tree output. Each leaf, blue for signal events and red for background events, represent a region in the variables phase space [114].

1950 more stability<sup>2</sup> and has a smaller misclassification rate than any individual ones. The  
 1951 resulting tree collection is known as a *boosted decision tree (BDT)*.  
 1952 Thus, purity of the sample is generalized to

<sup>2</sup> Decision trees suffer from sensitivity to statistical fluctuations in the training sample which may leads to very different results with an small change in the training samples.

$$P = \frac{\sum_s w_s}{\sum_s w_s + \sum_b w_b} \quad (5.5)$$

1953 where  $w_s$  and  $w_b$  are the weights of the events; the Gini index is also generalized

$$G = \left( \sum_i^n w_i \right) P(1 - P) \quad (5.6)$$

1954 with  $n$  the number of events in the node. The final score of an event, after pass-  
 1955 ing through the forest, is calculated as the renormalized sum of all the individual  
 1956 (possibly weighted) scores; thus, high(low) score implies that the event is most likely  
 1957 signal(background).

1958 The boosting procedure, implemented in the *Gradient boosting* algorithm used  
 1959 in this thesis, produce a classifier  $F(\mathbf{x})$  which is the weighted sum of the individual  
 1960 classifiers obtained after each iteration,i.e.,

$$F(\mathbf{x}) = \sum_{m=1}^M \beta_m f(\mathbf{x}; a_m) \quad (5.7)$$

1961 where M is the number of trees in the forest. The *loss function*  $L(F, y)$  represent the  
 1962 deviation between the classifier  $F(\mathbf{x})$  response and the true value  $y$  obtained from the  
 1963 training sample (1 for signal events and -1 for background event), according to

$$L(F, y) = \ln(1 + e^{-2F(\mathbf{x})y}) \quad (5.8)$$

1964 thus, the reweighting is employed to ensure the minimization of the loss function;  
 1965 a more detailed description of the minimization procedure can be found in reference  
 1966 [115]. The final classifier output is later used as a final discrimination variable, labeled  
 1967 as *BDT output/response*.

1968 **5.1.3 Overtraining.**

1969 Decision trees offer the possibility to have as many nodes as wished in order to  
 1970 reduce the misclassification to zero (in theory); however, when a classifier is too much  
 1971 adjusted to a particular training sample, the classifier response to a slightly different  
 1972 sample may leads to a completely different classification results; this effect is know  
 1973 as *overtraining*.

1974 An alternative to reduce the overtraining in BDTs consist in pruning the tree by  
 1975 removing statistically insignificant nodes after the tree growing is completed but this  
 1976 option is not available for BDTs with gradient boosting in the TMVA-toolkit, there-  
 1977 fore, the overtraining has to be reduced by tuning the algorithm, number of nodes,  
 1978 minimum number of events in the leaves, etc. The overtraining can be evaluated  
 1979 by comparing the responses of the classifier when running over the training and test  
 1980 samples.

1981 **5.1.4 Variable ranking.**

1982 BDTs have the couple of particular advantages related to the input variables; on one  
 1983 side, they are relatively insensitive to the number of input variables used in the vector  
 1984  $\mathbf{x}$ . The ranking of the BDT input variables is determined by counting the number of  
 1985 times a variable is used to split decision tree nodes; in addition, the separation gain-  
 1986 squared achieved in the splitting and the number of events in the node are accounted  
 1987 by applying a weighting to that number. Thus, those variables with small or no power  
 1988 to separate signal and background events are rarely chosen to split the nodes,i.e., are  
 1989 effectively ignored.

1990 On the other side, variables correlations play an important role for some MVA  
 1991 methods like the Fisher discriminant algorithm in which the first step consist of

1992 performing a linear transformation to a phase space where the correlations between  
 1993 variables are removed; in case of BDT algorithm, correlations do not affect the per-  
 1994 formance.

1995 **5.1.5 BDT output example.**

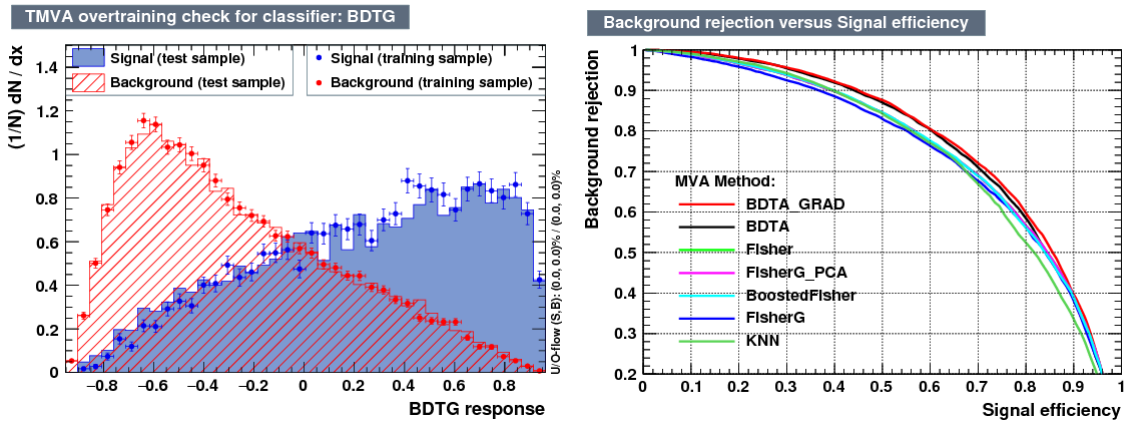


**Figure 5.5:** Left: Output distributions for the gradient boosted decision tree (BDTG) classifier using a sample of signal( $pp \rightarrow tHq$ ) and background( $pp \rightarrow t\bar{t}$ ) events. Right: Background rejection vs signal efficiency (ROC curves) for various MVA classifiers running over the same sample used to produce the plot on the left.

1996 Left side of figure 5.5 shows the BDT output distributions for signal( $pp \rightarrow tHq$ )  
 1997 and background( $pp \rightarrow t\bar{t}$ ) events; this plot is the equivalent to the one showed in  
 1998 figure 5.2. A forest with 800 trees, maximum depth per tree = 3, and gradient  
 1999 boosting have been used as training parameters. The BDTG classifier offers a good  
 2000 separation power; while there is a small overtraining in the signal distribution, the  
 2001 background distribution seems to be well predicted which might indicate that the  
 2002 sample is composed of more background than signal events.

2003 Right side of figure 5.5 shows the background rejection vs signal efficiency curves  
 2004 for several combinations of MVA classifiers-boosting algorithms; these curves are  
 2005 known as ROC curves and give an indication of the performance of the classifier. The

2006 best performance is achieved with the BDTG classifier (BDTA\_GRAD).

## 2007 5.2 Statistical inference.

2008 Once events are classified, the next step consists in finding the parameters that define  
 2009 the likelihood functions  $f(\mathbf{x}|s), f(\mathbf{x}|b)$  for signal and background events respectively.  
 2010 In general, likelihood functions depend not only on the measurements but also on  
 2011 parameters ( $\theta_m$ ) that define their shapes; the process of estimating these *unknown*  
 2012 *parameters* and their uncertainties from the experimental data is called *inference*.  
 2013 The likelihood function for  $N$  the events the in a sample is the combination of all the  
 2014 likelihoods functions

$$L(\boldsymbol{\theta}) = \prod_{i=1}^N f(\mathbf{x}^i | \boldsymbol{\theta}) = \prod_{i=1}^N f(x_1^i, \dots, x_n^i; \theta_1, \dots, \theta_m) \quad (5.9)$$

2015 Thus, the estimation of the unknown parameters from experimental data samples  
 2016 is written in terms of a central value using the notation

$$\theta = \hat{\theta} \pm \delta\theta \quad (5.10)$$

2017 where the interval  $[\hat{\theta} + \delta\theta, \hat{\theta} - \delta\theta]$  is called *confidence interval*; it is usually inter-  
 2018 preted, in the limit of infinite number of experiments, as the interval where the true  
 2019 value of the unknown parameter  $\theta$  is contained with a probability of 0.6827 (if no  
 2020 other convention is stated).

### 2021 5.2.1 Nuisance parameters.

2022 The unknown parameter vector  $\boldsymbol{\theta}$  is made of two types of parameters: on one side,  
 2023 those parameters that provide information about the physical observables of interest

2024 for the experiment (*parameters of interest*); on the other side, the *nuisance parameters*  
 2025 that are not of direct interest for the experiment but that needs to be included in  
 2026 the analysis in order to achieve a satisfactory description of the data. They represent  
 2027 effects of the detector response like the finite resolutions of the detection systems,  
 2028 miscalibrations, and in general any source of uncertainty introduced in the analysis.

2029 In some cases the nuisance parameters are estimated using dedicated data samples,  
 2030 for instance data from test beams for calibration purposes, when MC samples are  
 2031 not suitable. The nuisance parameter uncertainties produce *systematic uncertainties*  
 2032 while the uncertainties associated to fluctuations in data and related to the estimation  
 2033 of the parameters of interest produce *statistical uncertainties*.

### 2034 5.2.2 Maximum likelihood estimation method

2035 The function that produce the estimate of a parameter is called *estimator*, there-  
 2036 fore, estimators are usually constructed using mathematical procedures encoded in  
 2037 algorithms. The estimation method used in this thesis is the *Maximum Likelihood*  
 2038 *Estimation* method (MLE); it is based on the combined likelihood function defined  
 2039 by eqn. 5.9 and the procedure seeks for the parameter set that corresponds to the  
 2040 maximum value of the combined likelihood function, i.e., the *maximum likelihood*  
 2041 *estimator* of the unknown parameter vector  $\boldsymbol{\theta}$  is the function that produce the vec-  
 2042 tor  $\hat{\boldsymbol{\theta}}$  for which the likelihood function  $L(\boldsymbol{\theta})$  evaluated at the measured sample  $\mathbf{x}$  is  
 2043 maximum.

2044 Usually, the logarithm of the likelihood function is used in the numerical algo-  
 2045 rithms implementations in order to avoid underflow the numerical precision of the  
 2046 computers due to the product of low likelihoods. In addition, it is usual minimize the  
 2047 negative logarithm of the likelihood function instead of maximizing the logarithm of

2048 it because in this way the procedure consist of differentiate a sum of therms and set  
 2049 the sum to zero; therefore

$$F(\boldsymbol{\theta}) = -\ln L(\boldsymbol{\theta}) = -\sum_{i=1}^N f(\mathbf{x}^i | \boldsymbol{\theta}). \quad (5.11)$$

2050 The minimization process is performed by the software MINUIT [116] imple-  
 2051 mented in the ROOT analysis framework. In case of large data samples the compu-  
 2052 tational resources needed to calculate the likelihood function are too big; therefore,  
 2053 the parameter estimation is performed using binned distributions of the variables of  
 2054 interest for which the *binned likelihood function* is given by

$$L(data|\mu, \theta) = \prod_{i=1} \frac{(\mu s_i(\theta) + b_i(\theta))^{n_i}}{n_i!} e^{-\mu s_i(\theta) - b_i(\theta)}, \quad (5.12)$$

2055 with  $s_i$  and  $b_i$  the expected number of signal and background yields for bin  $i$  respec-  
 2056 tively,  $n_i$  is the observed number of events in the bin  $i$  and  $\mu = \sigma/\sigma_{SM}$  is the signal  
 2057 strength. Notice that the number of entries per bin follows a Poisson distribution.  
 2058 The analysis presented in this thesis is based on the binned distribution of the ratio  
 2059 signal/background obtained from the BDT outputs.

### 2060 5.2.3 Hypothesis test

2061 The test statistic mentioned in section 5.1 involving  
 2062 ; it is achieved, according to the Neyman-Pearson lemma [117],  
 2063 by defining the acceptance region such that, for  $\mathbf{x}$  inside the region, the likelihood  
 2064 ratio, i.e., the ratio of probability distribution functions for signal and background,

2065 **5.3 exclusion limits**

2066 **5.4 asymptotic limits**

2067 **Chapter 6**

2068 **Search for production of a Higgs**  
2069 **boson and a single top quark in**  
2070 **multilepton final states in pp**  
2071 **collisions at  $\sqrt{s} = 13$  TeV**

2072 **6.1 Introduction**

2073 The Higgs boson discovery, supported on experimental observations and theoretical  
2074 predictions made about the SM, gives the clue of the way in that elementary particles  
2075 acquire mass through the Higgs mechanism; therefore, knowing the Higgs mass, the  
2076 Higgs-boson and Higgs-fermion couplings can be tested. In order to test the Higgs-top  
2077 coupling, several measurements have been performed, as stated in the chapter 2, but  
2078 they are limited to measure the square of the coupling; however, the production of a  
2079 Higgs boson in association with a single top quark ( $tH$ ) not only offers access to the  
2080 sign of the coupling, but also, to the CP phase of the Higgs couplings.

2081 This chapter presents the search for the associated production of a Higgs boson  
 2082 and a single top quark events, focusing on leptonic signatures provided by the Higgs  
 2083 decay modes to  $WW$ ,  $ZZ$ , and  $\tau\tau$ ; the 13 TeV dataset produced in 2016, which  
 2084 corresponds to an integrated luminosity of  $35.9\text{fb}^{-1}$ , is used. Constraints on the sign  
 2085 of the Higgs-top coupling ( $y_t$ ) have been derived from the decay rate of Higgs boson  
 2086 to photon pairs [40] and from the cross section for associated production of Higgs and  
 2087 Z bosons via gluon fusion [118], with recent results disfavoring negative signs of the  
 2088 coupling [51, 53, 119]. It expands previous analyses performed at 8 TeV [120, 121] and  
 2089 searches for associated production of  $t\bar{t}$  pair and a Higgs boson in the multilepton final  
 2090 state channel [122]; it also complements searches in other decay channels targeting  
 2091  $H \rightarrow b\bar{b}$  [123].

2092 As shown in section 2.4, the SM cross section of the associated production of a  
 2093 Higgs boson and a single top quark ( $tHq$ ) process is driven by a destructive interfer-  
 2094 ence between two contributions (see Figure 2.13), where the Higgs couples to either  
 2095 the W boson or the top quark; however, if the sign of the Higgs-top coupling is flipped  
 2096 with respect to the SM prediction, a large enhancement of the cross section occurs,  
 2097 making this analysis sensitive to such deviation. A second process, where the Higgs  
 2098 boson and top quark are accompanied by a W boson ( $tHW$ ) has similar behavior,  
 2099 albeit with a weaker interference pattern and lower contribution to the  $tH$  cross sec-  
 2100 tion, therefore, a combination of both processes would increase the sensitivity; in  
 2101 this analysis both contributions are combined and referred as  $tH$ channel. A third  
 2102 contribution comes from  $t\bar{t}H$  process. The purpose of this analysis is to investigate  
 2103 the exclusion of the presence of the  $tH + t\bar{t}H$  processes under the assumption of the  
 2104 anomalous Higgs-top coupling modifier ( $\kappa_t = -1$ ). The analysis exploits signatures with  
 2105 two leptons of the same sign (*2lss channel*) and three leptons (*3l channel*) in the final  
 2106 state.

2107        The first sections present the characteristic  $tHq$  signature as well as the expected  
 2108   backgrounds. The MC samples, data sets, and the physics object definitions are  
 2109   then defined. Following, the background predictions, the signal extraction, and the  
 2110   statistical treatment of the selected events as well as the systematic uncertainties are  
 2111   described. The final section present the results for the exclusion limits as a function  
 2112   of the ratio of  $\kappa_t$  and the dimensionless modifier of the Higgs-vector boson  $\kappa_V$ .

## 2113   **6.2 $tHq$ signature**

2114   In order to select events of  $tHq$  process, its features are translated into a set of  
 2115   selection rules; figure 6.1 shows the Feynman diagram and an schematic view of the  
 2116    $tHq$  process from the  $pp$  collision to the final state configuration. A single top quark  
 2117   is produced accompanied by a light quark, denoted as  $q$ ; this light quark is produced  
 2118   predominantly in the forward region of the detector. The Higgs boson which can  
 2119   be either emitted by the exchanged  $W$  boson or directly by the singly produced top  
 2120   quark.

2121        The top quark and Higgs boson decay after their production in the detector due to  
 2122   their high masses/low lifetimes. The Higgs boson is required to decay into a  $W$  boson  
 2123   pair<sup>1</sup>. The top quark almost always decays into a bottom quark and a  $W$  boson, as  
 2124   encoded in the CMK matrix. The  $W$  bosons are required to decay hadronically in  
 2125   the 2lss channel case and leptonically in the 3l channel case, while  $\tau$  leptons are not  
 2126   reconstructed separately and only their leptonic decays into either electrons or muons  
 2127   are considered in this analysis.

2128        In summary, the signal process is characterized by a the final state with

- 2129        • one light-flavored forward jet,

---

<sup>1</sup> ZZ and  $\tau\tau$  decays are also include in the analysis but they are not separately reconstructed

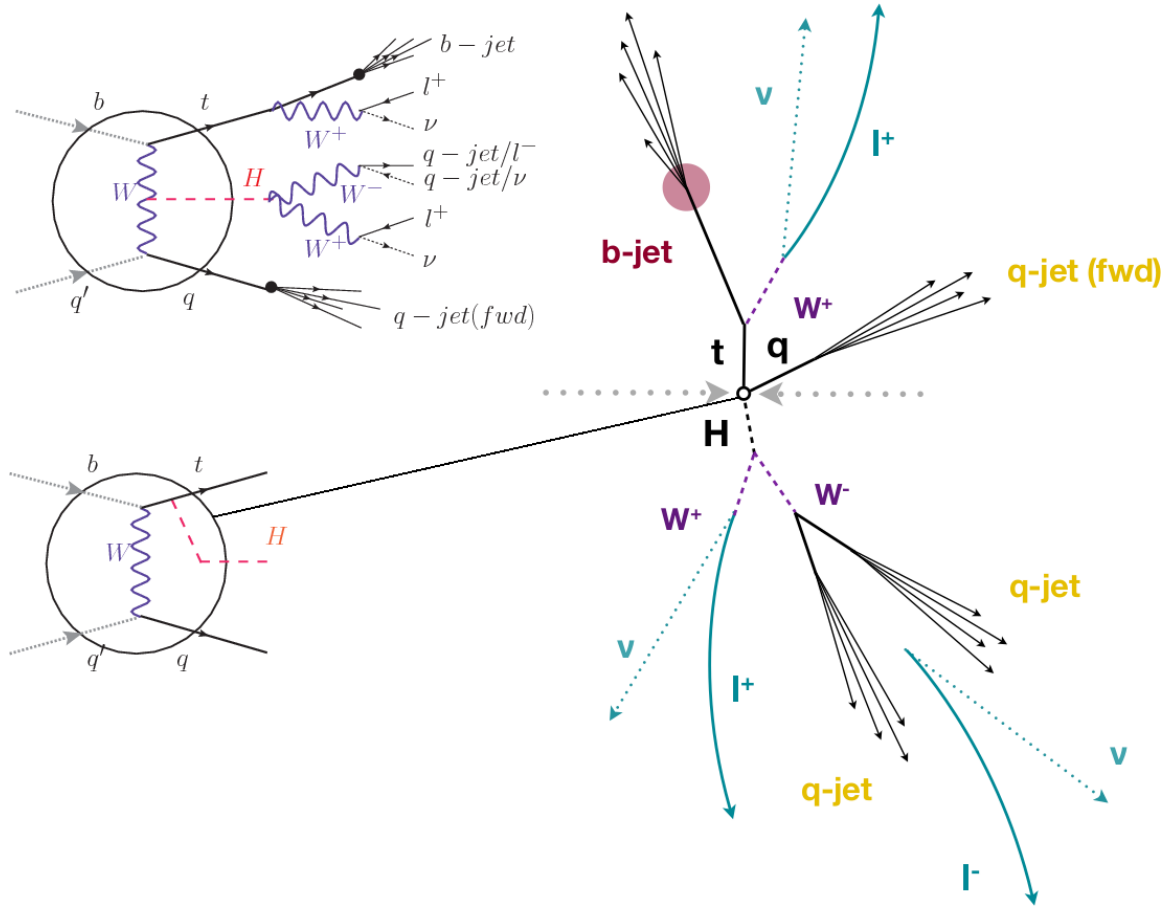


**Figure 6.1:**  $tHq$  event signature. Left: Feynman diagram including the whole evolution up to the final state for the case of the Higgs boson emitted by the  $W$  boson (top); Feynman diagram for the case where the Higgs boson is emitted by the top quark. Right: Schematic view as it would be seen in the detector; the circle in the Feynman diagrams on the left corresponds to the circle in the center of the schematic view as indicated by the line connecting them. In the 2lss channel, one of the  $W$  bosons from the Higgs boson decays to two light-quark jets while in the 3l channel both  $W$  bosons decays to leptons.

- 2130     • one central b-jet,
  - 2131     • 2lss channel  $\rightarrow$  two leptons of the same sign, two neutrinos and two light (often  
2132        soft) jets,
  - 2133     • 3l channel  $\rightarrow$  three leptons, three neutrinos and no central light-flavored jets,
- 2134     The presence of neutrinos is inferred from the presence of MET. The analysis has

2135 been made public by CMS as a Physics Analysis Summary [124] combining the result  
 2136 for the three lepton and two lepton same-sign channels. Currently, an effort to turn  
 2137 the analysis into a paper is ongoing.

2138 **6.3 Background processes**

2139 The background processes are those that can mimic the signal signature or at least  
 2140 can be reconstructed as that as a result of certain circumstances. The backgrounds  
 2141 can be classified as

2142 • Irreducible backgrounds where genuine prompt leptons are produced in on-  
 2143 shell W and Z boson decays; they can be reliably estimated directly from MC  
 2144 simulated events, using higher-order cross sections or data control regions for  
 2145 the overall normalization.

2146 • Reducible backgrounds where at least one of the leptons is *non-prompt*, i.e., pro-  
 2147 duced within a hadronic jet, either a genuine lepton from heavy flavor decays.  
 2148 misreconstructed jets, also known as *mis-ID leptons* or *fake leptons*, are consid-  
 2149 ered non-prompt leptons as well. These non-prompt leptons leave tracks and  
 2150 hits in the detection systems as would a prompt lepton, but correlating those  
 2151 hits with nearby jets could be a way of removing them. Reducible backgrounds  
 2152 are not well predicted by simulation, and are estimated using data-driven meth-  
 2153 ods.

2154 The main sources of background events in the case of  $tHq$  process are  $t\bar{t}$  process  
 2155 and  $t\bar{t} + X(X = W, Z, \gamma)$  processes, here represented together as  $t\bar{t}V$  process. Figure  
 2156 6.2 shows the signature for  $t\bar{t}$  and  $t\bar{t}W$  processes;

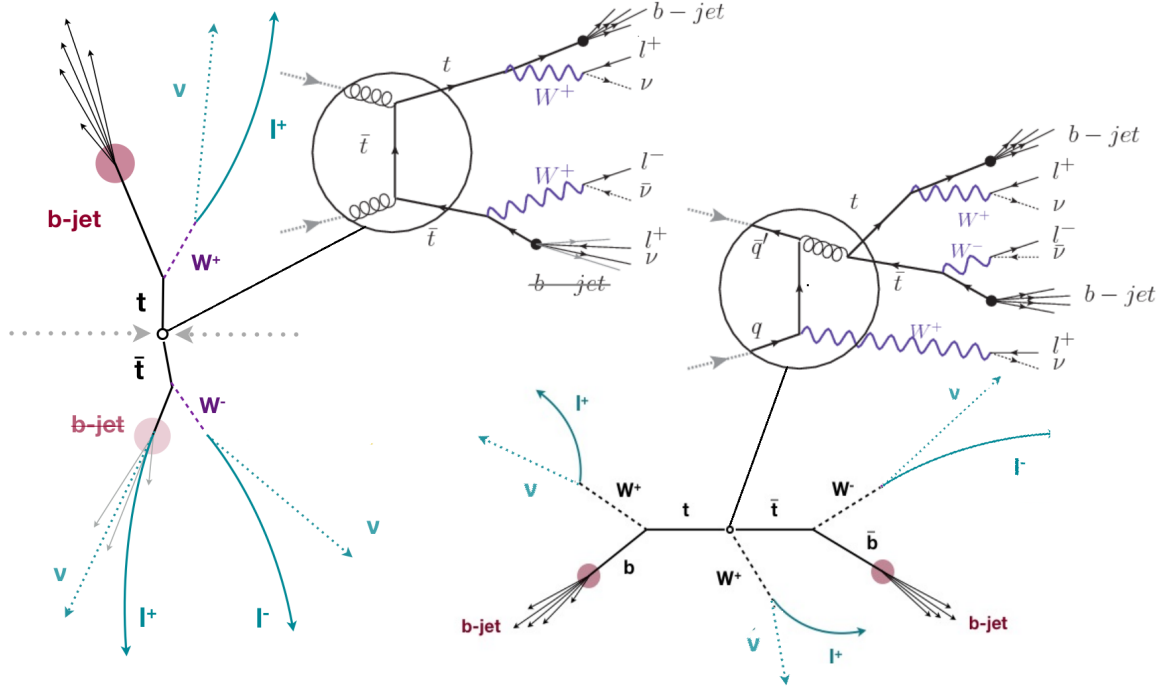


**Figure 6.2:**  $t\bar{t}$  (left) and  $t\bar{t}W$ (right) events signature as they would be seen in the detector; the Feynman diagrams including the whole evolution up to the final state are also showed. The  $t\bar{t}$  process signature is very similar to that of the signal process with one fake lepton and non forward activity. The  $t\bar{t}W$ process present a higher b-jet multiplicity compared to the signal process, a prompt lepton and no forward activity.

2157        The largest contribution to irreducible backgrounds involving prompt leptons  
 2158        comes from  $t\bar{t}W$ ,  $t\bar{t}Z$ , processes for which the number of ( $b-$ )jets (( $b-$ )jet multiplicity)  
 2159        is higher than that of the signal events, while for other contributing background  
 2160        events,  $WZ$ ,  $ZZ$ , and rare SM processes like  $W^\pm W^\pm qq$ ,  $t\bar{t}t\bar{t}$ ,  $tZq$ ,  $tZW$ ,  $WWW$ ,  
 2161         $WWZ$ ,  $WZZ$ ,  $ZZZ$ , the ( $b-$ )jet multiplicity is lower compared to that of the signal  
 2162        events. None of the irreducible backgrounds present activity in the forward region of  
 2163        the detector.

2164        On the side of the reducible backgrounds, the largest contribution comes from the  
 2165         $t\bar{t}$  events which have a very similar signature to the signal events but does no present  
 2166        activity in the forward region of the detector either; A particular feature of the  $t\bar{t}$   
 2167        events is their charge-symmetry which is also a difference with the signal events.

2168        The charge misidentification plays an important role in the the 2lss channel since  
 2169        leptons in processes like  $t\bar{t} + \text{jets}$  or  $Z + \text{jets}$  can be charge misidentified, leading to  
 2170        backgrounds increments. An identification variable have been designed in order to  
 2171        reject this type of background events.

## 2172        6.4 Data and MC Samples

2173        The data considered in this analysis were collected by the CMS experiment dur-  
 2174        ing 2016 and correspond to a total integrated luminosity of  $35.9 fb^{-1}$ . Only periods  
 2175        when the CMS magnet was on were considered when selecting the data samples, that  
 2176        corresponds to the 23 Sep 2016 (Run B to G) and PromptReco (Run H) versions  
 2177        of the datasets. The MC samples used in this analysis correspond to the RunI-  
 2178        ISummer16MiniAODv2 campaign produced with CMSSW 80X. The two signal sam-  
 2179        ples (for  $tHq$  and  $tHW$ ) were produced with MG5\_aMC@NLO (version 5.222), in  
 2180        leading-order order mode, and are normalized to next-to-leading-order cross sections,  
 2181        see Tab. 6.4. Each sample is generated with a set of event weights corresponding to  
 2182        different values of  $\kappa_t$  and  $\kappa_V$  couplings as shown in Tab. 6.5.

### 2183        6.4.1 Full 2016 dataset and MC samples

Sample	$\sigma$ [pb]	BF
/THQ_Hincl_13TeV-madgraph-pythia8_TuneCUETP8M1/	0.7927	0.324
/THW_Hincl_13TeV-madgraph-pythia8_TuneCUETP8M1/	0.1472	1.0

**Table 6.1:** Signal samples and their cross section and branching fraction used in this analysis. See Ref. [133] for more details.

2184        Different MC generators were used to generate the background processes. The  
 2185        dominant sources ( $t\bar{t}$ ,  $t\bar{t}W$ ,  $t\bar{t}Z$ ,  $t\bar{t}H$ ) were produced using AMC@NLO interfaced  
 2186        to PYTHIA8, and are scaled to NLO cross sections. Other processes are simulated

		<i>tHq</i>		<i>tHW</i>		
$\kappa_V$	$\kappa_t$	sum of weights	cross section [pb]	sum of weights	cross section [pb]	LHE weights
1.0	-3.0	35.700022	2.991	11.030445	0.6409	LHEweight_wgt[446]
1.0	-2.0	20.124298	1.706	5.967205	0.3458	LHEweight_wgt[447]
1.0	-1.5	14.043198	1.205	4.029093	0.2353	LHEweight_wgt[448]
1.0	-1.25	11.429338	0.9869	3.208415	0.1876	LHEweight_wgt[449]
1.0	-1.0		0.7927		0.1472	
1.0	-0.75	7.054998	0.6212	1.863811	0.1102	LHEweight_wgt[450]
1.0	-0.5	5.294518	0.4723	1.339886	0.07979	LHEweight_wgt[451]
1.0	-0.25	3.818499	0.3505	0.914880	0.05518	LHEweight_wgt[452]
1.0	0.0	2.627360	0.2482	0.588902	0.03881	LHEweight_wgt[453]
1.0	0.25	1.719841	0.1694	0.361621	0.02226	LHEweight_wgt[454]
1.0	0.5	1.097202	0.1133	0.233368	0.01444	LHEweight_wgt[455]
1.0	0.75	0.759024	0.08059	0.204034	0.01222	LHEweight_wgt[456]
1.0	1.0	0.705305	0.07096	0.273617	0.01561	LHEweight_wgt[457]
1.0	1.25	0.936047	0.0839	0.442119	0.02481	LHEweight_wgt[458]
1.0	1.5	1.451249	0.1199	0.709538	0.03935	LHEweight_wgt[459]
1.0	2.0	3.335034	0.2602	1.541132	0.08605	LHEweight_wgt[460]
1.0	3.0	10.516125	0.8210	4.391335	0.2465	LHEweight_wgt[461]
1.5	-3.0	45.281492	3.845	13.426212	0.7825	LHEweight_wgt[462]
1.5	-2.0	27.606715	2.371	7.809713	0.4574	LHEweight_wgt[463]
1.5	-1.5	20.476088	1.784	5.594971	0.3290	LHEweight_wgt[464]
1.5	-1.25	17.337465	1.518	4.635978	0.2749	LHEweight_wgt[465]
1.5	-1.0	14.483302	1.287	3.775902	0.2244	LHEweight_wgt[466]
1.5	-0.75	11.913599	1.067	3.014744	0.1799	LHEweight_wgt[467]
1.5	-0.5	9.628357	0.874	2.352505	0.1410	LHEweight_wgt[468]
1.5	-0.25	7.627574	0.702	1.789184	0.1081	LHEweight_wgt[469]
1.5	0.0	5.911882	0.5577	1.324946	0.08056	LHEweight_wgt[470]
1.5	0.25	4.479390	0.4365	0.959295	0.05893	LHEweight_wgt[471]
1.5	0.5	3.331988	0.3343	0.692727	0.04277	LHEweight_wgt[472]
1.5	0.75	2.469046	0.2558	0.525078	0.03263	LHEweight_wgt[473]
1.5	1.0	1.890565	0.2003	0.456347	0.02768	LHEweight_wgt[474]
1.5	1.25	1.596544	0.1689	0.486534	0.02864	LHEweight_wgt[475]
1.5	1.5	1.586983	0.1594	0.615638	0.03509	LHEweight_wgt[476]
1.5	2.0	2.421241	0.2105	1.170602	0.06515	LHEweight_wgt[477]
1.5	3.0	7.503280	0.5889	3.467546	0.1930	LHEweight_wgt[478]
0.5	-3.0	27.432685	2.260	8.929074	0.5136	LHEweight_wgt[479]
0.5	-2.0	13.956013	1.160	4.419093	0.2547	LHEweight_wgt[480]
0.5	-1.5	8.924438	0.7478	2.757611	0.1591	LHEweight_wgt[481]
0.5	-1.25	6.835341	0.5726	2.075247	0.1204	LHEweight_wgt[482]
0.5	-1.0	5.030704	0.4273	1.491801	0.08696	LHEweight_wgt[483]
0.5	-0.75	3.510528	0.2999	1.007273	0.05885	LHEweight_wgt[484]
0.5	-0.5	2.274811	0.1982	0.621663	0.03658	LHEweight_wgt[485]
0.5	-0.25	1.323555	0.1189	0.334972	0.01996	LHEweight_wgt[486]
0.5	0.0	0.656969	0.06223	0.147253	0.008986	LHEweight_wgt[487]
0.5	0.25	0.274423	0.02830	0.058342	0.003608	LHEweight_wgt[488]
0.5	0.5	0.176548	0.01778	0.068404	0.003902	LHEweight_wgt[489]
0.5	0.75	0.363132	0.03008	0.177385	0.009854	LHEweight_wgt[490]
0.5	1.0	0.834177	0.06550	0.385283	0.02145	LHEweight_wgt[491]
0.5	1.25	1.589682	0.1241	0.692099	0.03848	LHEweight_wgt[492]
0.5	1.5	2.629647	0.2047	1.097834	0.06136	LHEweight_wgt[493]
0.5	2.0	5.562958	0.4358	2.206057	0.1246	LHEweight_wgt[494]
0.5	3.0	14.843102	1.177	5.609519	0.3172	LHEweight_wgt[495]

**Table 6.2:**  $\kappa_V$  and  $\kappa_t$  combinations generated for the two signal samples and their NLO cross sections. The *tHq* cross section is multiplied by the branching fraction of the enforced leptonic decay of the top quark (0.324). See also Ref. [133].

Sample	$\sigma$ [pb]
TTWJetsToLNu_TuneCUETP8M1_13TeV-amcatnloFXFX-madspin-pythia8	0.2043
TTZToLLNuNu_M-10_TuneCUETP8M1_13TeV-amcatnlo-pythia8	0.2529
tthJetToNonbb_M125_13TeV_amcatnloFXFX_madspin_pythia8_mWCutfix /store/cmst3/group/susy/gpetrucc/13TeV/u/TTLL_m1to10_L0_NoMS_for76X/	0.2151 0.0283
WGToLNuG_TuneCUETP8M1_13TeV-madgraphMLM-pythia8	585.8
ZGTo2LG_TuneCUETP8M1_13TeV-amcatnloFXFX-pythia8	131.3
TGJets_TuneCUETP8M1_13TeV_amcatnlo_madspin_pythia8	2.967
TGJets_TuneCUETP8M1_13TeV_amcatnlo_madspin_pythia8	2.967
TTGJets_TuneCUETP8M1_13TeV-amcatnloFXFX-madspin-pythia8	3.697
WpWpJJ_EWK_QCD_TuneCUETP8M1_13TeV-madgraph-pythia8	0.03711
ZZZ_TuneCUETP8M1_13TeV-amcatnlo-pythia8	0.01398
WWZ_TuneCUETP8M1_13TeV-amcatnlo-pythia8	0.1651
WZZ_TuneCUETP8M1_13TeV-amcatnlo-pythia8	0.05565
WW_DoubleScattering_13TeV-pythia8	1.64
tZq_ll_4f_13TeV-amcatnlo-pythia8_TuneCUETP8M1	0.0758
ST_tWll_5f_LO_13TeV-MadGraph-pythia8	0.01123
TTTT_TuneCUETP8M1_13TeV-amcatnlo-pythia8	0.009103
WZTo3LNu_TuneCUETP8M1_13TeV-powheg-pythia8	4.4296
ZZTo4L_13TeV_powheg_pythia8	1.256
TTJets_SingleLeptFromTbar_TuneCUETP8M1_13TeV-madgraphMLM-pythia8	182.1754
TTJets_SingleLeptFromT_TuneCUETP8M1_13TeV-madgraphMLM-pythia8	182.1754
TTJets_DiLept_TuneCUETP8M1_13TeV-madgraphMLM-pythia8	87.3
DYJetsToLL_M-10to50_TuneCUETP8M1_13TeV-amcatnloFXFX-pythia8	18610
DYJetsToLL_M-50_TuneCUETP8M1_13TeV-madgraphMLM-pythia8	6024
WJetsToLNu_TuneCUETP8M1_13TeV-amcatnloFXFX-pythia8	61526.7
ST_tW_top_5f_inclusiveDecays_13TeV-powheg-pythia8_TuneCUETP8M1	35.6
ST_tW_antitop_5f_inclusiveDecays_13TeV-powheg-pythia8_TuneCUETP8M1	35.6
ST_t-channel_4f_leptonDecays_13TeV-amcatnlo-pythia8_TuneCUETP8M1	70.3144
ST_t-channel_antitop_4f_leptonDecays_13TeV-powheg-pythia8_TuneCUETP8M1	26.2278
ST_s-channel_4f_leptonDecays_13TeV-amcatnlo-pythia8_TuneCUETP8M1	3.68064
WWTo2L2Nu_13TeV-powheg	10.481

**Table 6.3:** List of background samples used in this analysis (CMSSW 80X). In the first section of the table are listed the samples of the processes for which we use the simulation to extract the final yields and shapes, in the second section the samples of the processes we will estimate from data. The MC simulation is used to design the data driven methods and derive the associated systematics.

Sample	$\sigma$ [pb]
ttWJets_13TeV_madgraphMLM	0.6105
ttZJets_13TeV_madgraphMLM	0.5297/0.692

**Table 6.4:** Leading-order  $t\bar{t}W$  and  $t\bar{t}Z$  samples used in the signal BDT training.

2187 using POWHEG interfaced to PYTHIA, or bare PYTHIA (see table 6.6 and [122]  
2188 for more details).

2189 **6.4.2 Triggers**

2190 We consider online-reconstructed events triggered by one, two, or three leptons.  
 2191 Single-lepton triggers are included to boost the acceptance of events where the  $p_T$  of  
 2192 the sub-leading lepton falls below the threshold of the double-lepton triggers. Ad-  
 2193 ditionally, by including double-lepton triggers in the  $\geq 3$  lepton category, as well  
 2194 as single-lepton triggers in all categories, we increase the efficiency, considering the  
 2195 logical “or” of the trigger decisions of all the individual triggers in a given category.  
 2196 Tab. 6.8 shows the lowest-threshold non-prescaled triggers present in the High-Level  
 2197 Trigger (HLT) menus for both Monte-Carlo and data in 2016.

2198 **Trigger efficiency scale factors**

2199 The efficiency of events to pass the trigger is measured in simulation (trivially using  
 2200 generator information) and in the data (using event collected by an uncorrelated  
 2201 MET trigger). Small differences between the data and MC efficiencies are corrected  
 2202 by applying scale factors as shown in Tab. 6.9. The exact procedure and control plots  
 2203 are documented in [127] for the current analysis.

2204 **6.5 Object Identification**

2205 In this section, the specific definitions of the physical objects in terms of the numerical  
 2206 values assigned to the reconstruction parameters are presented; thus, the provided  
 2207 details summarize and complement the descriptions presented in previous chapters.  
 2208 The object reconstruction and selection strategy used in this thesis is inherited from  
 2209 the analyses in references [122, 127], thus, the information provided in this section is  
 2210 extracted from those documents unless other references are stated.

Same-sign dilepton (==2 muons)
HLT_Mu17_TrkIsoVVL_Mu8_TrkIsoVVL_DZ_v*
HLT_Mu17_TrkIsoVVL_TkMu8_TrkIsoVVL_DZ_v*
HLT_IsoMu22_v*
HLT_IsoTkMu22_v*
HLT_IsoMu22_eta2p1_v*
HLT_IsoTkMu22_eta2p1_v*
HLT_IsoMu24_v*
HLT_IsoTkMu24_v*
Same-sign dilepton (==2 electrons)
HLT_Ele23_Ele12_CaloIdL_TrackIdL_IsoVL_DZ_v*
HLT_Ele27_eta2p1_WP Loose_Gsf_v*
HLT_Ele27_WPTight_Gsf_v*
HLT_Ele25_eta2p1_WPTight_Gsf_v*
Same-sign dilepton (==1 muon, ==1 electron)
HLT_Mu23_TrkIsoVVL_Ele8_CaloIdL_TrackIdL_IsoVL_v*
HLT_Mu8_TrkIsoVVL_Ele23_CaloIdL_TrackIdL_IsoVL_v*
HLT_Mu23_TrkIsoVVL_Ele8_CaloIdL_TrackIdL_IsoVL_DZ_v*
HLT_Mu8_TrkIsoVVL_Ele23_CaloIdL_TrackIdL_IsoVL_DZ_v*
HLT_IsoMu22_v*
HLT_IsoTkMu22_v*
HLT_IsoMu22_eta2p1_v*
HLT_IsoTkMu22_eta2p1_v*
HLT_IsoMu24_v*
HLT_IsoTkMu24_v*
HLT_Ele27_WPTight_Gsf_v*
HLT_Ele25_eta2p1_WPTight_Gsf_v*
HLT_Ele27_eta2p1_WP Loose_Gsf_v*
Three lepton and Four lepton
HLT_DiMu9_Ele9_CaloIdL_TrackIdL_v*
HLT_Mu8_DiEle12_CaloIdL_TrackIdL_v*
HLT_TripleMu_12_10_5_v*
HLT_Ele16_Ele12_Ele8_CaloIdL_TrackIdL_v*
HLT_Mu23_TrkIsoVVL_Ele8_CaloIdL_TrackIdL_IsoVL_v*
HLT_Mu23_TrkIsoVVL_Ele8_CaloIdL_TrackIdL_IsoVL_DZ_v*
HLT_Mu8_TrkIsoVVL_Ele23_CaloIdL_TrackIdL_IsoVL_v*
HLT_Mu8_TrkIsoVVL_Ele23_CaloIdL_TrackIdL_IsoVL_DZ_v*
HLT_Ele23_Ele12_CaloIdL_TrackIdL_IsoVL_DZ_v*
HLT_Mu17_TrkIsoVVL_Mu8_TrkIsoVVL_DZ_v*
HLT_Mu17_TrkIsoVVL_TkMu8_TrkIsoVVL_DZ_v*
HLT_IsoMu22_v*
HLT_IsoTkMu22_v*
HLT_IsoMu22_eta2p1_v*
HLT_IsoTkMu22_eta2p1_v*
HLT_IsoMu24_v*
HLT_IsoTkMu24_v*
HLT_Ele27_WPTight_Gsf_v*
HLT_Ele25_eta2p1_WPTight_Gsf_v*
HLT_Ele27_eta2p1_WP Loose_Gsf_v*

**Table 6.5:** Table of high-level triggers that we consider in the analysis.

Category	Scale Factor
ee	$1.01 \pm 0.02$
e $\mu$	$1.01 \pm 0.01$
$\mu\mu$	$1.00 \pm 0.01$
3l	$1.00 \pm 0.03$

**Table 6.6:** Trigger efficiency scale factors and associated uncertainties, shown here rounded to the nearest percent.

### 2211 6.5.1 Jets and $b$ tagging.

2212 In this analysis, jets are reconstructed by clustering PF candidates using the anti- $k_t$   
 2213 algorithm with parameter distance  $\Delta R = 0.4$ ; those charged hadrons that are not  
 2214 consistent with the selected primary vertex are discarded from the clustering. The  
 2215 jet energy is then corrected for the varying response of the detector as a function  
 2216 of transverse momentum  $p_T$  and pseudorapidity  $\eta$ . Jets are selected for use in the  
 2217 analysis only if they have  $p_T > 25$  GeV and are separated from any selected leptons  
 2218 by  $\Delta R > 0.4$ .

2219 Jets coming from the primary vertex and jets coming from pile-up vertices are  
 2220 distinguished using a MVA discriminator based on the differences in the jet shapes,  
 2221 in the relative multiplicity of charged and neutral components, and in the different  
 2222 fraction of transverse momentum which is carried by the hardest components. Jet  
 2223 tracks are also required to be compatible with the primary vertex.

2224 Jets originated from the hadronization of a  $b$  quark are selected using a MVA  
 2225 likelihood discriminant which uses track-based lifetime information and reconstructed  
 2226 secondary vertices (CSV algorithm). Only jets within the CMS tracker acceptance  
 2227 ( $\eta < 2.4$ ) are identified with this tool. Data samples are used to measure the efficiency  
 2228 of the  $b$  tagging and the probability to misidentify jets from light quarks or gluons;  
 2229 in both cases the measurements are parametrized as a function of the jet  $p_T$  and  $\eta$   
 2230 and later used to correct differences between the data and MC simulation in the  $b$

tagging performance, by applying per-jet weights to the simulation, dependent on the jet  $p_T$ ,  $\eta$ ,  $b$  tagging discriminator, and flavor (from simulation truth) [125]. The per-event weight is taken as the product of the per-jet weights, including those of the jets associated to the leptons. The weights are derived on  $t\bar{t}$  and Z+jets events.

Two working points are defined, based on the CSV algorithm output: *loose*' working point ( $\text{CSV} > 0.46$ ) with a  $b$  signal tagging efficiency of about 83% and a mistagging rate of about 8%; and *medium* working point ( $\text{CSV} > 0.80$ ) with  $b$ -tagging efficiency of about 69% and mistagging rate of order 1% [126]. Tagging of jets from charm quarks have efficiencies of about 40% and 18% for loose and medium working points respectively. Separate scale factors are applied to jets originating from bottom/charm quarks and from light quarks in simulated events to match the tagging efficiencies measured in the data.

### 6.5.2 Missing Energy MET.

As stated in section 4.4.1.1, the MET vector is calculated as the negative of the vector sum of transverse momenta of all PF candidates in the event and its magnitude is referred to as  $E_T^{\text{miss}}$ . Due to pile-up interactions, the performance in determining MET is degraded; in order to correct for that, the energy from the selected jets and leptons that compose the event is assigned to the variable  $H_T^{\text{miss}}$ . It is calculated in the same way as  $E_T^{\text{miss}}$  and although it has worse resolution than  $E_T^{\text{miss}}$ , it is more robust in the sense that it does not rely on the soft part of the event. The event selection uses a linear discriminator based on the two variables given by

$$E_T^{\text{miss}} \text{LD} = 0.00397 * E_T^{\text{miss}} + 0.00265 * H_T^{\text{miss}} \quad (6.1)$$

taking advantage of the fact that the correlation between  $E_T^{\text{miss}}$  and  $H_T^{\text{miss}}$  is less

2253 for events with instrumental missing energy than for events with real missing energy.  
 2254 The working point  $E_T^{miss} LD > 0.2$  was chosen to ensure a good signal efficiency while  
 2255 keeping a good background rejection.

### 2256 6.5.3 Lepton reconstruction and identification

2257 Two types of leptons are defined in this analysis: *signal leptons* are those coming from  
 2258  $W, Z$  and  $\tau$  decays which usually are isolated from other particles; *background leptons*  
 2259 are defined as leptons produced in  $b$  hadron decays, light-jets misidentification, and  
 2260 photon conversions.

2261 The process of reconstruction and identification of electron and muon candidates  
 2262 was described in chapter4, hence, the identification variables used in order to retain  
 2263 the highest possible efficiency for signal leptons while maximizing the rejection of  
 2264 background leptons are listed and described in the following sections <sup>2</sup>.

2265 The identification variables include not only observables related directly to the re-  
 2266 constructed leptons themselves, but also to the clustered energy deposits and charged  
 2267 particles in a cone around the lepton direction (jet-related variables); an initial loose  
 2268 preselection of leptons candidates is performed and then an MVA discriminator, re-  
 2269 fered to as *lepton MVA* discriminator, is used to distinguish signal leptons from  
 2270 background leptons.

#### 2271 Muons.

2272 The Physics Objects Groups (POG) at CMS, are in charge of studying and defining  
 2273 the set of selection criteria applied on the course of reconstruction and identification  
 2274 of particles. These selection criteria are implemented in the CMS framework in the

---

<sup>2</sup> the studies performed to optimize the identification are far from the scope of this thesis, therefore, only general descriptions are provided

2275 form of several object identification working points according to the strength of the  
 2276 requirements.

2277 The muon candidates are reconstructed by combining information from the tracker  
 2278 system and the muon detection system of CMS detector and the POG defined three  
 2279 working points for muon identification *MuonID* [128];

2280 • *POG Loose Muon ID* is a particle identified as a muon by the PF event re-  
 2281 construction and also reconstructed either as a global-muon or as an arbitrated  
 2282 tracker-muon. This identification criteria is designed to be highly efficient for  
 2283 prompt muons and for muons from heavy and light quark decays; it can be com-  
 2284 plemented by applying impact parameter cuts in analyses with prompt muon  
 2285 signals.

2286 • *POG Medium Muon ID* is a Loose muon with additional track-quality and  
 2287 muon-quality (spatial matching between the individual measurements in the  
 2288 tracker and the muon system) requirements. This identification criteria is de-  
 2289 signed to be highly efficient in the separation of the muons coming from decay  
 2290 in flight of heavy quarks and muons coming from B meson decays as well as  
 2291 prompt muons. An additional category *MVA Prompt ID* is defined in this iden-  
 2292 tification criteria directed to discriminated muons from B mesons and prompt  
 2293 muons (from W,Z and  $\tau$  decays). The Medium ID provides the same fake rate as  
 2294 the Tight Muon ID but a higher efficiency on prompt and B-decays muons. [129]

2295 • *POG Tight Muon ID* is a global muon with additional muon-quality require-  
 2296 ments Tight Muon ID selects a subset of the PF muons.

2297 Only muons within the muon system acceptance  $|\eta| < 2.4$  and minimum  $p_T$  of 5  
 2298 GeV are considered.

2299 **Electrons.**

2300 Electrons are reconstructed using information from the tracker and from the electro-  
 2301 magnetic calorimeter and identified by an MVA algorithm (*MVA eID* discriminant)  
 2302 using the shape of the calorimetric shower variables like the shape in  $\eta$  and  $\phi$ , the clus-  
 2303 ter circularity, widths along  $\eta$  and  $\phi$ ; track-cluster matching variables like  $E_{tot}/p_{in}$ ,  
 2304  $E_{Ele}/p_{out}$ ,  $\Delta\eta_{in}$ ,  $\Delta\eta_{out}$ ,  $\Delta\phi_{in}$ ,  $1/E - 1/p$ ; and track quality variables like  $\xi^2$  of the  
 2305 GSF tracks, the number of hits used by the GSF filter [130].

2306 A loose selection based on  $\eta$ -dependent cuts on this discriminant is used to prese-  
 2307 lect electron candidates, the full shape of the discriminant is used in the lepton MVA  
 2308 selection to separate signal leptons from background leptons (described in section  
 2309 6.4.3).

2310 In order to reject electrons from photon conversions, electron candidates with  
 2311 missing hits in the pixel tracker layers or matched to a conversion secondary vertex  
 2312 are discarded. Electrons are selected for the analysis if they have  $p_T > 7$  GeV and  
 2313 are located within the tracker system acceptance region ( $|\eta| < 2.5$ ).

2314 **Lepton vertexing and pile-up rejection.**

2315 The impact parameter in the transverse plane  $d_0$ , impact parameter along the z  
 2316 axis  $d_z$ , and the impact parameter significance in the detector space  $SIP_{3D}$ , are  
 2317 considered to perform the identification and rejection of pile-up, misreconstructed  
 2318 tracks, and background leptons from b-hadron decays; pile-up and misreconstructed  
 2319 track mitigation is achieved by imposing loose cuts on the impact parameter variables.  
 2320 The full shape of those variables is used in a lepton MVA classifier to achieve the  
 2321 best separation between the signal and the background leptons.

2322 **Lepton isolation.**

2323 PF is able to recognize leptons from two different sources: on one side, leptons from  
 2324 the decays of heavy particles, such as W and Z bosons, which are normally isolated  
 2325 in space from the hadronic activity in the event; on the other side, leptons from the  
 2326 decays of hadrons and jets misidentified as leptons, which are not isolated as the  
 2327 former. For highly boosted systems, like the lepton and the  $b$ -jet generated in the  
 2328 semileptonic decay of a boosted top, the decay products tend to be more closer and  
 2329 sometimes they even overlap; thus, the PF standard definition of isolation in terms of  
 2330 the separation between the lepton candidates and other PF objects in the  $\eta$ - $\phi$  plane,

$$\Delta R = \sqrt{(\eta^l - \eta^i)^2 + (\phi^l - \phi^i)^2} < 0.3 \quad (6.2)$$

2331 which considers all the neutral, charged hadrons and photons in a cone around the  
 2332 leptons, is refocused to the local isolation of the leptons through the mini-isolation  
 2333  $I_{mini}$  [131] defined as the sum of particle flow candidates  $p_T$  within a cone around  
 2334 the lepton, corrected for the effects of pileup and divided by the lepton  $p_T$

$$I_{mini} = \frac{\sum_R p_T(h^\pm) - \max\left(0, \sum_R p_T(h^0) + p_T(\gamma) - \rho \mathcal{A}\left(\frac{R}{0.3}\right)^2\right)}{p_T(l)} \quad (6.3)$$

2335 where  $\rho$  is the pileup energy density,  $h^\pm, h^0, \gamma, l$ , represent the charged hadron, neutral  
 2336 hadrons, photons, and the lepton, respectively. The radius  $R$  of the cone depends on  
 2337 the  $p_T$  of the lepton according to

$$R = \frac{10\text{GeV}}{\min(\max(p_T(l), 50\text{GeV}), 200\text{GeV})}, \quad (6.4)$$

2338 The  $p_T$  dependence of the cone size allows for greater signal efficiency. Setting a

2339 cut on  $I_{mini}$  below a given threshold ensures that the lepton is locally isolated, even  
 2340 in boosted systems. The effect of pileup is mitigated using the so-called effective area  
 2341 correction  $\mathcal{A}$  listed in Table6.1.

$ \eta $ range	$\mathcal{A}(e)$ neutral/charged	$A(\mu)$ neutral/charged
0.0 - 0.8	0.1607 / 0.0188	0.1322 / 0.0191
0.8 - 1.3	0.1579 / 0.0188	0.1137 / 0.0170
1.3 - 2.0	0.1120 / 0.0135	0.0883 / 0.0146
2.0 - 2.2	0.1228 / 0.0135	0.0865 / 0.0111
2.2 - 2.5	0.2156 / 0.0105	0.1214 / 0.0091

**Table 6.7:** Effective areas, for electrons and muons used to mitigate the effect of pileup by using the so-called effective area correction.

2342 A loose cut on  $I_{mini}$  is applied to pre-select the muon and electron candidates;  
 2343 however, the full shape is used in the lepton MVA discriminator when performing the  
 2344 signal lepton selection.

### 2345 Jet-related variables.

2346 In order to reject misidentified leptons from  $b$ -jets, mostly coming from tt+jets,  
 2347 Drell-Yan+jets, and W+jets events, the vertexing and isolation described in previous  
 2348 sections are complemented with additional variables related to the closest recon-  
 2349 structed jet to the lepton, i.e., the PF jets reconstructed<sup>3</sup> around the leptons with  
 2350  $\Delta R = \sqrt{(\eta^l - \eta^{jet})^2 + (\phi^l - \phi^{jet})^2} < 0.5$ . The identification variables used in the lep-  
 2351 ton MVA discriminator are the ratio  $p_T^l/p_T^{jet}$ , the CSV b-tagging discriminator value  
 2352 of the jet, the number of charged tracks of the jet, and the relative  $p_T$  given by

$$p_T^{rel} = \frac{(\vec{p}_{jet} - \vec{p}_l) \cdot \vec{p}_l}{\|\vec{p}_{jet} - \vec{p}_l\|}. \quad (6.5)$$

---

<sup>3</sup> charged hadrons from PU vertices are not removed prior to the jet clustering.

2353 **LeptonMVA discriminator.**

2354 Electrons and muons passing the basic selection process described above are referred  
 2355 to as *loose leptons*. Additional discrimination between signal leptons and background  
 2356 leptons is crucial considering that the rate of  $t\bar{t}$  production is much larger than the  
 2357 signal, hence, an overwhelming background from  $t\bar{t}$  production. To maximally ex-  
 2358 ploit the available information in each event to that end, the dedicated lepton MVA  
 2359 discriminator, based on a boosted decision tree (BDT) algorithm, has been built so  
 2360 that all the identification variables can be used together.

2361 The lepton MVA discriminator training is performed using simulated signal Loose  
 2362 leptons from the  $t\bar{t}H$  MC sample and fake leptons from the  $t\bar{t}$  + jets MC sample,  
 2363 separately for muons and electrons. The input variables used include vertexing, iso-  
 2364 lation and jet-related variables, the  $p_T$  and  $\eta$  of the lepton, the electron MVA eID  
 2365 discriminator and the muon segment-compatibility variables. An additional require-  
 2366 ment known as *tight-charge* requirement, is imposed by comparing two independent  
 2367 measurement of the charge, one from the ECAL supercluster and the other from the  
 2368 tracker; thus, the consistency in the measurements of the electron charge is ensured  
 2369 so that events with a wrong electron charge assignment are rejected; this variable is  
 2370 particularly used in the 2lss channel to suppress opposite-sign events for which the  
 2371 charge of one of the leptons has been mismeasured. The tight-charge requirement for  
 2372 muons is represented by the requirement of a consistently well measured track trans-  
 2373 verse momentum given by  $\Delta p_T/p_T < 0.2$ . Leptons are selected for the final analysis  
 2374 if they pass a given threshold of the BDT output, and are referred to as *tight leptons*  
 2375 in the following.

2376 The validation of the lepton MVA algorithm and the lepton identification variables  
 2377 is performed using data in various control regions; the details about that validation

2378 are not discussed here but can be found in Reference [127].

2379 **Selection definitions**

2380 Electron and muon object identification is defined in three different sets of selections  
 2381 criteria; the *Loose*, *Fakeable Object*, and *Tight* selection. These three levels of selection  
 2382 are designed to serve for event level vetoes, the fake rate estimation application region,  
 2383 and the final signal selection, respectively. The  $p_T$  of fakeable objects is defined as  
 2384  $0.85 \times p_T(\text{jet})$ , where the jet is the one associated to the lepton object. This mitigates  
 2385 the dependence of the fake rate on the momentum of the fakeable object and thereby  
 2386 improves the precision of the method.

2387 Tables 6.2 and 6.3 list the full criteria for the different selections of muons and  
 2388 electrons.

Cut	Loose	Fakeable object	Tight
$ \eta  < 2.4$	✓	✓	✓
$p_T$	$> 5\text{GeV}$	$> 15\text{GeV}$	$> 15\text{GeV}$
$ d_{xy}  < 0.05$ (cm)	✓	✓	✓
$ d_z  < 0.1$ (cm)	✓	✓	✓
$\text{SIP}_{3D} < 8$	✓	✓	✓
$I_{\text{mini}} < 0.4$	✓	✓	✓
is Loose Muon	✓	✓	✓
jet CSV	—	$< 0.8484$	$< 0.8484$
is Medium Muon	—	—	✓
tight-charge	—	—	✓
lepMVA $> 0.90$	—	—	✓

**Table 6.8:** Requirements on each of the three muon selections. In the cases where the cut values change between the selections, those values are listed in the table. Otherwise, whether the cut is applied is indicated.

2389 In addition to the previously defined requirements for jets, they are required to  
 2390 be separated from any lepton candidates passing the fakeable object selections by  
 2391  $\Delta R > 0.4$ .

Cut	Loose	Fakeable Object	Tight
$ \eta  < 2.5$	✓	✓	✓
$p_T$	$> 7\text{GeV}$	$> 15\text{GeV}$	$> 15\text{GeV}$
$ d_{xy}  < 0.05 \text{ (cm)}$	✓	✓	✓
$ d_z  < 0.1 \text{ (cm)}$	✓	✓	✓
$\text{SIP}_{3D} < 8$	✓	✓	✓
$I_{\text{mini}} < 0.4$	✓	✓	✓
MVA eID $> (0.0, 0.0, 0.7)$	✓	✓	✓
$\sigma_{in\eta} < (0.011, 0.011, 0.030)$	—	✓	✓
$\text{H/E} < (0.10, 0.10, 0.07)$	—	✓	✓
$\Delta\eta_{in} < (0.01, 0.01, 0.008)$	—	✓	✓
$\Delta\phi_{in} < (0.04, 0.04, 0.07)$	—	✓	✓
$-0.05 < 1/E - 1/p < (0.010, 0.010, 0.005)$	—	✓	✓
$p_T^{\text{ratio}}$	—	$> 0.5^\dagger / -$	—
jet CSV	—	$< 0.3^\dagger / < 0.8484$	$< 0.8484$
tight-charge conversion rejection	—	—	✓
Number of missing hits	$< 2$	$== 0$	$== 0$
lepton MVA $> 0.90$	—	—	✓

**Table 6.9:** Criteria for each of the three electron selections. In cases where the cut values change between selections, those values are listed in the table. Otherwise, whether the cut is applied is indicated. In some cases, the cut values change for different  $\eta$  ranges. These ranges are  $0 < |\eta| < 0.8$ ,  $0.8 < |\eta| < 1.479$ , and  $1.479 < |\eta| < 2.5$  and the respective cut values are given in the form (value<sub>1</sub>, value<sub>2</sub>, value<sub>3</sub>). For the two  $p_T^{\text{ratio}}$  and CSV rows, the cuts marked with a  $\dagger$  are applied to leptons that fail the lepton MVA cut, while the loose cut value is applied to those that pass the lepton MVA cut.

## 2392 6.5.4 Lepton selection efficiency

2393 Efficiencies of reconstruction and selecting loose leptons are measured both for muons  
 2394 and electrons using a tag and probe method on both data and MC, using  $Z \rightarrow \ell^+ \ell^-$   
 2395 [132]. The scale factors are derived from the ratio of efficiencies  $\varepsilon_i(p_T, \eta)$  measured  
 2396 for a given lepton in data/MC, according to

$$\rho(p_T, \eta) = \frac{\varepsilon_{\text{data}}(p_T, \eta)}{\varepsilon_{\text{MC}}(p_T, \eta)}. \quad (6.6)$$

2397 The scale factor for each event is used to correct the weight of the event in the

2398 full sample; therefore, the full simulation correction is given by the product of all  
 2399 the individual scale factors. The scale factors used in this thesis are inherited from  
 2400 the reference [127] which in turns inherited them from leptonic SUSY analyses using  
 2401 equivalent lepton selections.

2402 The efficiency of applying the tight selection as defined in Tables 6.2 and 6.3, on the  
 2403 loose leptons are determined by using a tag and probe method on a sample of Drell-  
 2404 Yan enriched events. Figures 6.3 and 6.4 show the efficiencies for the 2lss channel and  
 2405 3l channel respectively. Efficiencies in the 2lss channel have been produced including  
 2406 the tight-charge requirement, while for the 3l channel it is not included. Number

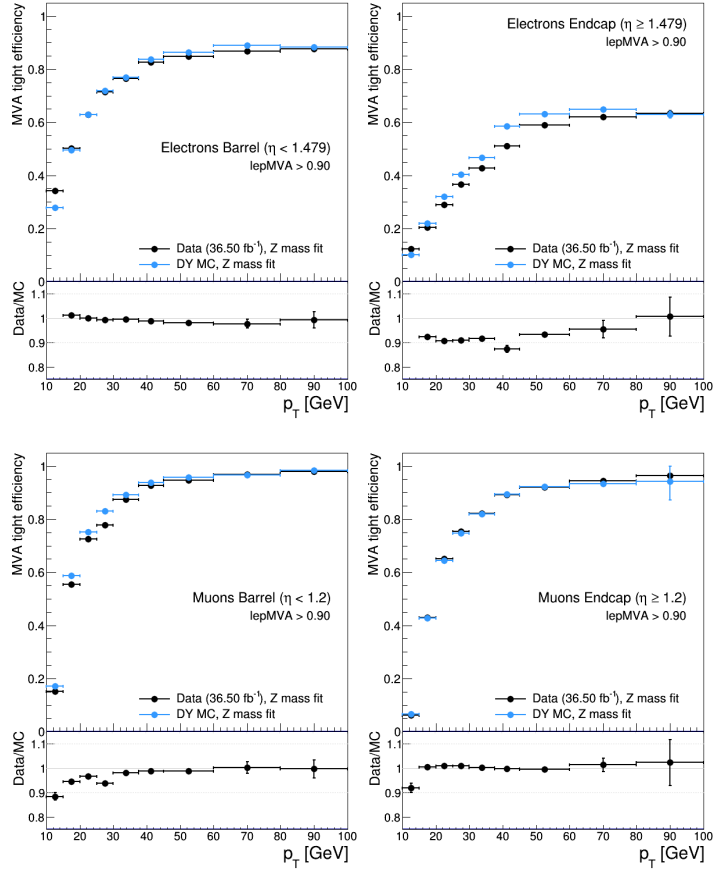


**Figure 6.3:** Tight vs loose selection efficiencies for electrons (top), and muons (bottom), for the 2lss definition, i.e., including the tight-charge requirement.

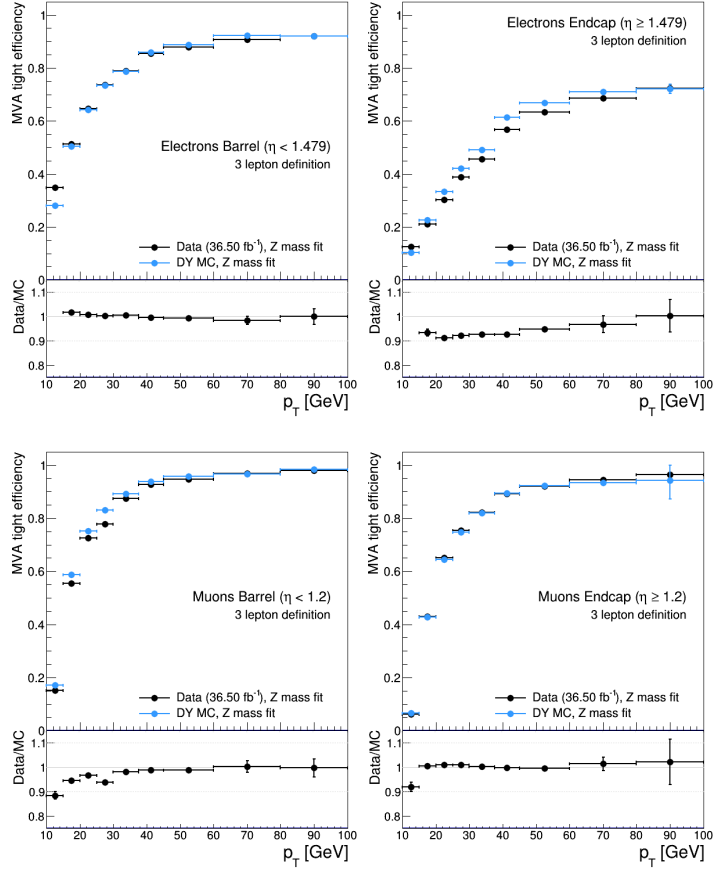


**Figure 6.4:** Tight vs loose selection efficiencies for electrons (top), and muons (bottom), for the 3l channel not including the tight-charge requirement.

of passed and failed probes are determined from a fit to the invariant mass of the dilepton system.

Simulation is corrected using these scale factors; note that they depends on  $\eta$  and  $p_T$ .

## 6.6 Event selection

.

.

2414 .

2415 .

2416 .

2417 .

2418 .

2419 .

2420 .

2421 . . .

2422       The analysis is designed to efficiently identify and select prompt leptons from  
2423 on-shell W and

2424       Z boson decays and to reject non-prompt leptons from b quark decays and spurious  
2425 lepton

2426       signatures from hadronic jets. Events are then selected in the various lepton  
2427 channels, and are

2428       required to contain hadronic jets, some of which must be consistent with b quark  
2429 hadronization. Finally, the signal yield is extracted by simultaneously fitting the  
2430 output of two dedicated

2431       multivariate discriminants (trained to separate the tHq signal from the two dom-  
2432 inant backgrounds) in all categories

2433       . Multivariate techniques are used to discriminate the signal from the dominant  
2434 backgrounds. The analysis yields a 95% confidence level (C.L.) upper limit on the  
2435 combined tH + ttH production cross section times branching ratio of 0.64 pb, with  
2436 an expected limit of 0.32 pb, for a scenario with  $kt = \sqrt{1.0}$  and  $kV = 1.0$ . Values  
2437 of  $kt$  outside the range of  $\sqrt{1.25}$  to  $\sqrt{1.60}$  are excluded at 95% C.L., assuming  $kV$   
2438  $= 1.0$ .

2439       Dont forget to mention previous constrains to ct check reference ?? and references

2440 <https://link.springer.com/content/pdf/10.1007%2FJHEP01%282013%29088.pdf> (para-  
 2441 graph after eq 2)

2442 We selects events with three leptons and a  $b$  tagged jet in the final state. The  $tHq$   
 2443 signal contribution is then determined in a fit of the observed data to two multivariate  
 2444 classifier outputs, each trained to discriminate against one of the two dominant back-  
 2445 grounds of events with non-prompt leptons from  $t\bar{t}$  and of associated production of  $t\bar{t}$   
 2446 and vector bosons ( $t\bar{t}W$ ,  $t\bar{t}Z$ ). The fit result is then used to set an upper limit on the  
 2447 combined  $t\bar{t}H$ ,  $tHq$  and  $tHW$  production cross section, as a function of the relative  
 2448 coupling strengths of Higgs and top quark and Higgs and W boson, respectively.

## 2449 6.7 Background predictions

2450 The modeling of reducible and irreducible backgrounds in this analysis uses the exact  
 2451 methods, analysis code, and ROOT trees used for the  $t\bar{t}H$  multilepton analysis. We  
 2452 give a brief description of the methods and refer to the documentation of that analysis  
 2453 in Refs. [122, 127] for any details.

2454 The backgrounds in three-lepton final states can be split in two broad categories:  
 2455 irreducible backgrounds with genuine prompt leptons (i.e. from on-shell W and Z  
 2456 boson decays); and reducible backgrounds where at least one of the leptons is “non-  
 2457 prompt”, i.e. produced within a hadronic jet, either a genuine lepton from heavy  
 2458 flavor decays, or simply mis-reconstructed jets.

2459 Irreducible backgrounds can be reliably estimated directly from Monte-Carlo sim-  
 2460 ulated events, using higher-order cross sections or data control regions for the overall  
 2461 normalization. This is done in this analysis for all backgrounds involving prompt lep-  
 2462 tons:  $t\bar{t}W$ ,  $t\bar{t}Z$ ,  $t\bar{t}H$ ,  $WZ$ ,  $ZZ$ ,  $W^\pm W^\pm qq$ ,  $t\bar{t}t\bar{t}$ ,  $tZq$ ,  $tZW$ ,  $WWW$ ,  $WWZ$ ,  $WZZ$ ,  
 2463  $ZZZ$ .

2464 Reducible backgrounds, on the other hand, are not well predicted by simulation,  
 2465 and are estimated using data-driven methods. In the case of non-prompt leptons, a  
 2466 fake rate method is used,

2467 Additional identification criteria are applied for electrons with  $p_T$  greater than 30  
 2468 GeV to mimic the identification applied at trigger level in order to ensure consistency  
 2469 between the measurement region and application region of the fake-rate.

2470 where the contribution to the final selection is estimated by extrapolating from  
 2471 a sideband (or “application region”) with a looser lepton definition (the fakeable  
 2472 object definitions in Tabs. 6.2 and 6.3) to the signal selection. The tight-to-loose  
 2473 ratios (or “fake rates”) are measured in several background dominated data events  
 2474 with dedicated triggers, subtracting the residual prompt lepton contribution using  
 2475 MC. Non-prompt leptons in our signal regions are predominantly produced in  $t\bar{t}$   
 2476 events, with a much smaller contribution, from Drell–Yan production. The systematic  
 2477 uncertainty on the normalization of the non-prompt background estimation is on the  
 2478 order of 50%, and thereby one of the dominant limitations on the performance of  
 2479 multilepton analyses in general and this analysis in particular. It consists of several  
 2480 individual sources, such as the result of closure tests of the method using simulated  
 2481 events, limited statistics in the data control regions due to necessary prescaling of  
 2482 lepton triggers, and the uncertainty in the subtraction of residual prompt leptons  
 2483 from the control region.

2484 The fake background where the leptons pass the looser selection are weighted  
 2485 according to how many of them fail the tight criteria. Events with a single failing  
 2486 lepton are weighted with the factor  $f/(1-f)$  for the estimate to the tight selection  
 2487 region, where  $f$  is the fake rate. Events with two failing leptons are given the negative  
 2488 weight  $-f_i f_j / (1-f_i)(1-f_j)$ , and for three leptons the weight is positive and equal  
 2489 to the product of  $f/(1-f)$  factor evaluated for each failing lepton.

2490 Figures 6.5 show the distributions of some relevant kinematic variables, normalized  
 to the cross section of the respective processes and to the integrated luminosity.

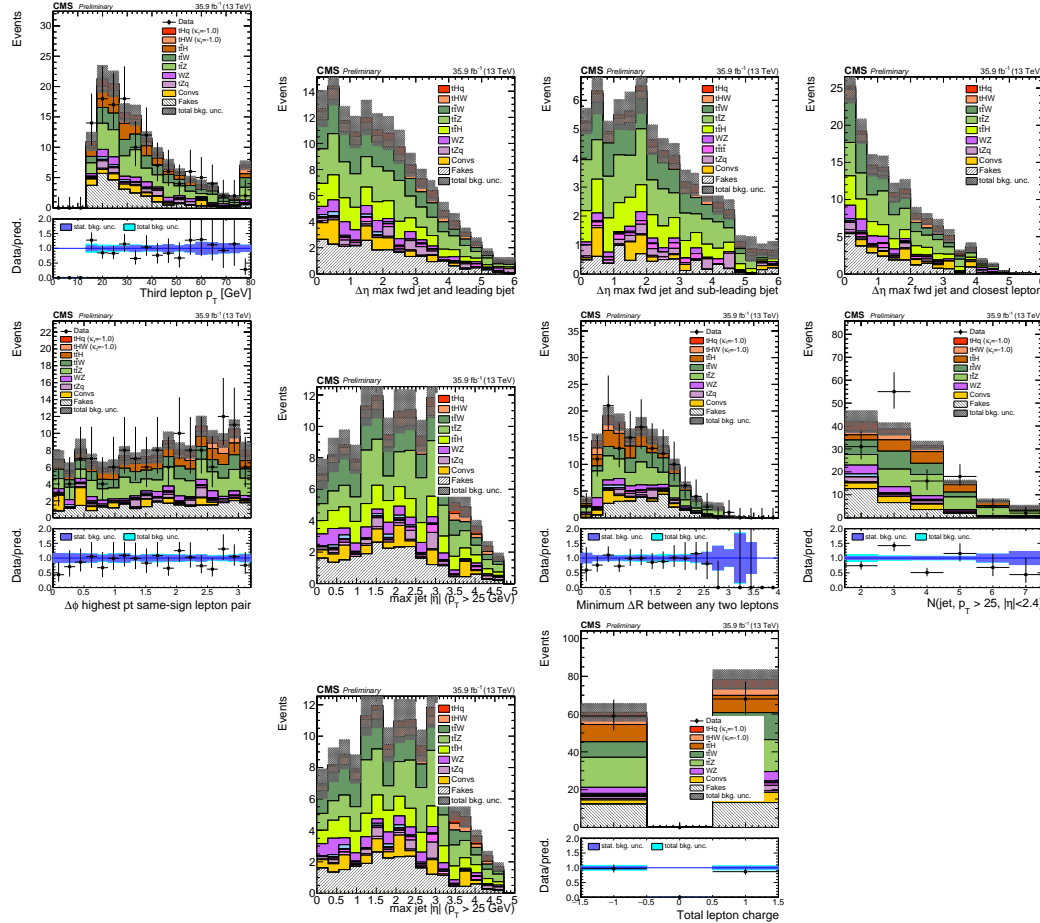


**Figure 6.5:** Distributions of input variables to the BDT for signal discrimination, three lepton channel, normalized to their cross section and to  $35.9 \text{ fb}^{-1}$ .

2491

## 2492 6.8 Signal discrimination

2493 The  $tHq$  signal is separated from the main backgrounds using a boosted decision  
 2494 tree (BDT) classifier, trained on simulated signal and background events. A set  
 2495 of discriminating variables are given as input to the BDT which produces a output  
 2496 distribution maximizing the discrimination power. Table 6.10 lists the input variables

used while Figures 6.6 show their distributions for the relevant signal and background samples, for the three lepton channel. Two BDT classifiers are trained for the two main backgrounds expected in the analysis: events with prompt leptons from  $t\bar{t}W$  and  $t\bar{t}Z$ (also referred to as  $t\bar{t}V$ ), and events with non-prompt leptons from  $t\bar{t}$ . The datasets used in the training are the  $tHq$  signal (see Tab. 6.4), and LO MADGRAPH samples of  $t\bar{t}W$  and  $t\bar{t}Z$ , in an admixture proportional to their respective cross sections (see Tab. 6.7).

Variable name	Description
nJet25	Number of jets with $p_T > 25$ GeV, $ \eta  < 2.4$
MaxEtaJet25	Maximum $ \eta $ of any (non-CSV-loose) jet with $p_T > 25$ GeV
totCharge	Sum of lepton charges
nJetEta1	Number of jets with $ \eta  > 1.0$ , non-CSV-loose
detaFwdJetBJet	$\Delta\eta$ between forward light jet and hardest CSV loose jet
detaFwdJet2BJet	$\Delta\eta$ between forward light jet and second hardest CSV loose jet (defaults to -1 in events with only one CSV loose jet)
detaFwdJetClosestLep	$\Delta\eta$ between forward light jet and closest lepton
dphiHighestPtSSPair	$\Delta\phi$ of highest $p_T$ same-sign lepton pair
minDRll	minimum $\Delta R$ between any two leptons
Lep3Pt/Lep2Pt	$p_T$ of the 3 <sup>rd</sup> lepton (2 <sup>nd</sup> for ss2l)

**Table 6.10:** MVA input discriminating variables

The MVA analysis consist of two stages: first a “training” where the MVA method is trained to discriminate between simulated signal and background events, then a “test” stage where the trained algorithm is used to classify different events from the samples. The sample is obtained from a pre-selection (see Tab. ?? with pre-selection cuts). Figures 6.7 show the input variables distributions as seen by the MVA algorithm. Note that in contrast to the distributions in Fig. 6.6 only the main backgrounds ( $t\bar{t}$  from simulation,  $t\bar{t}V$ ) are included.

Note that splitting the training in two groups reveals that some variables show

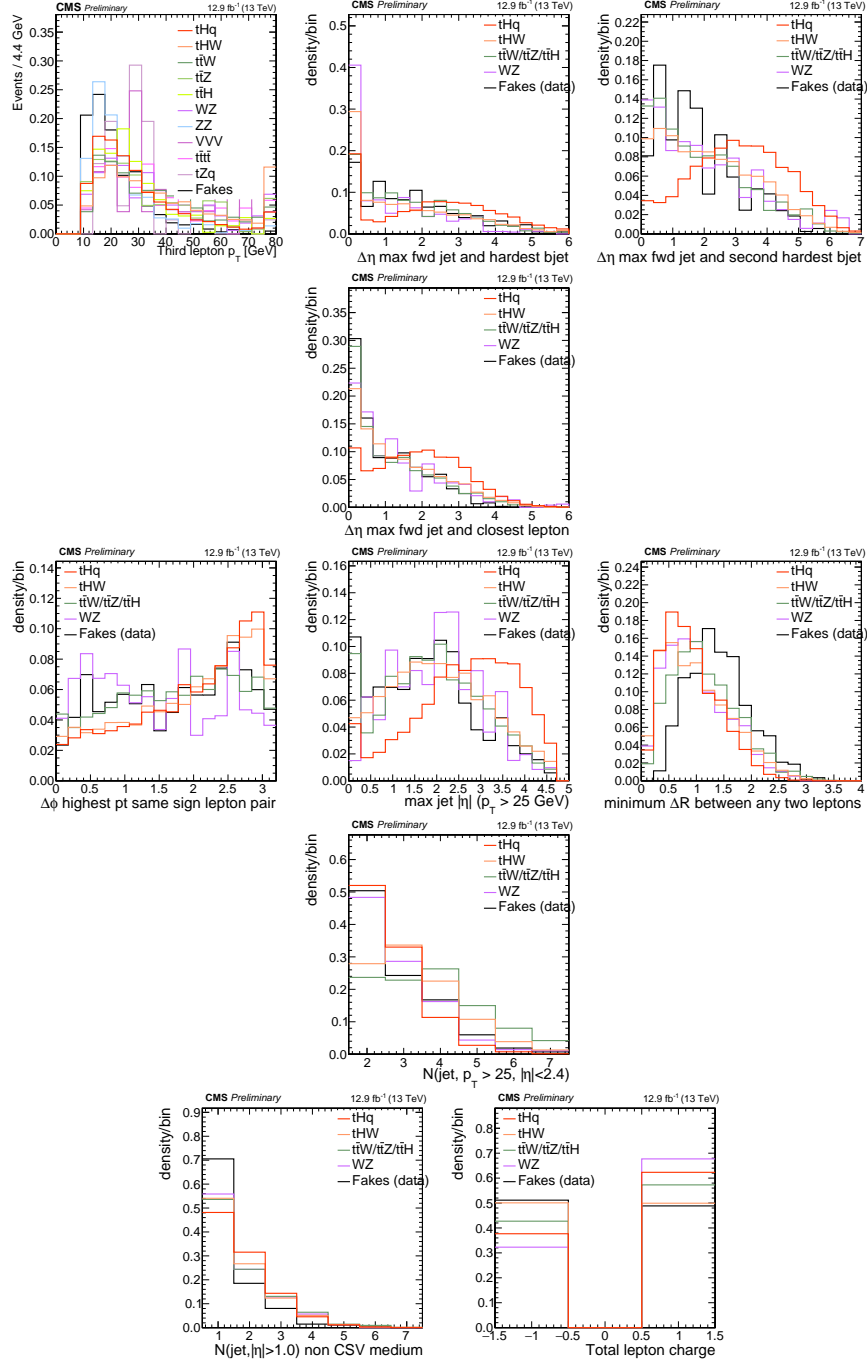


**Figure 6.6:** Distributions of input variables to the BDT for signal discrimination, three lepton channel.

opposite behavior for the two background sources; potentially screening the discrimination power if they were to be used in a single discriminant. For some other variables

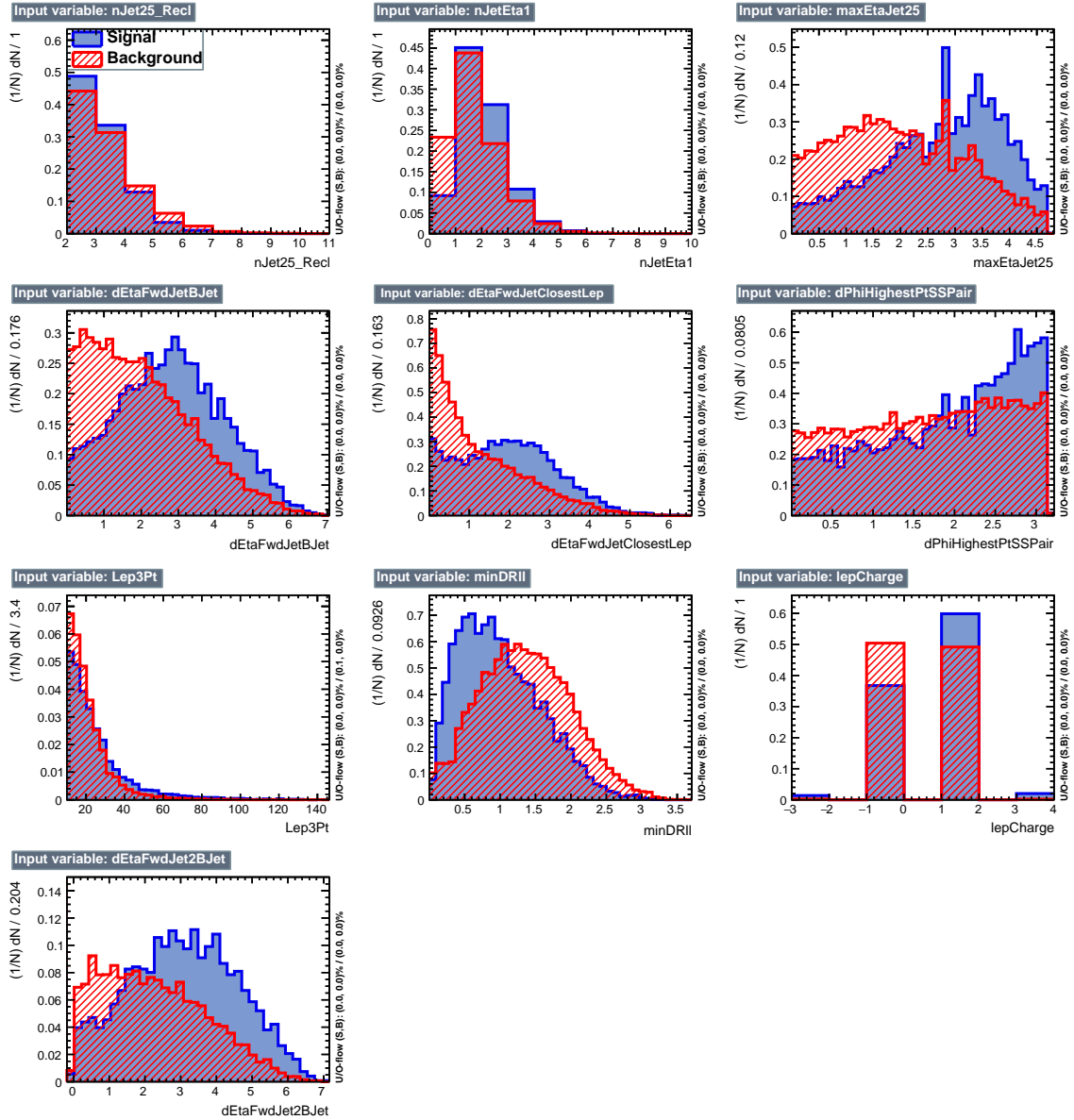


**Figure 6.7:** BDT inputs as seen by TMVA (signal, in blue, is  $tHq$ , background, in red, is  $t\bar{t}$ ) for the three lepton channel, discriminated against  $t\bar{t}$  (fakes) background.

the distributions are similar in both background cases.

From table 6.10, it is clear that the input variables are correlated to some extend. These correlations play an important role for some MVA methods like the Fisher discriminant method in which the first step consist of performing a linear transformation to an phase space where the correlations between variables are removed. In

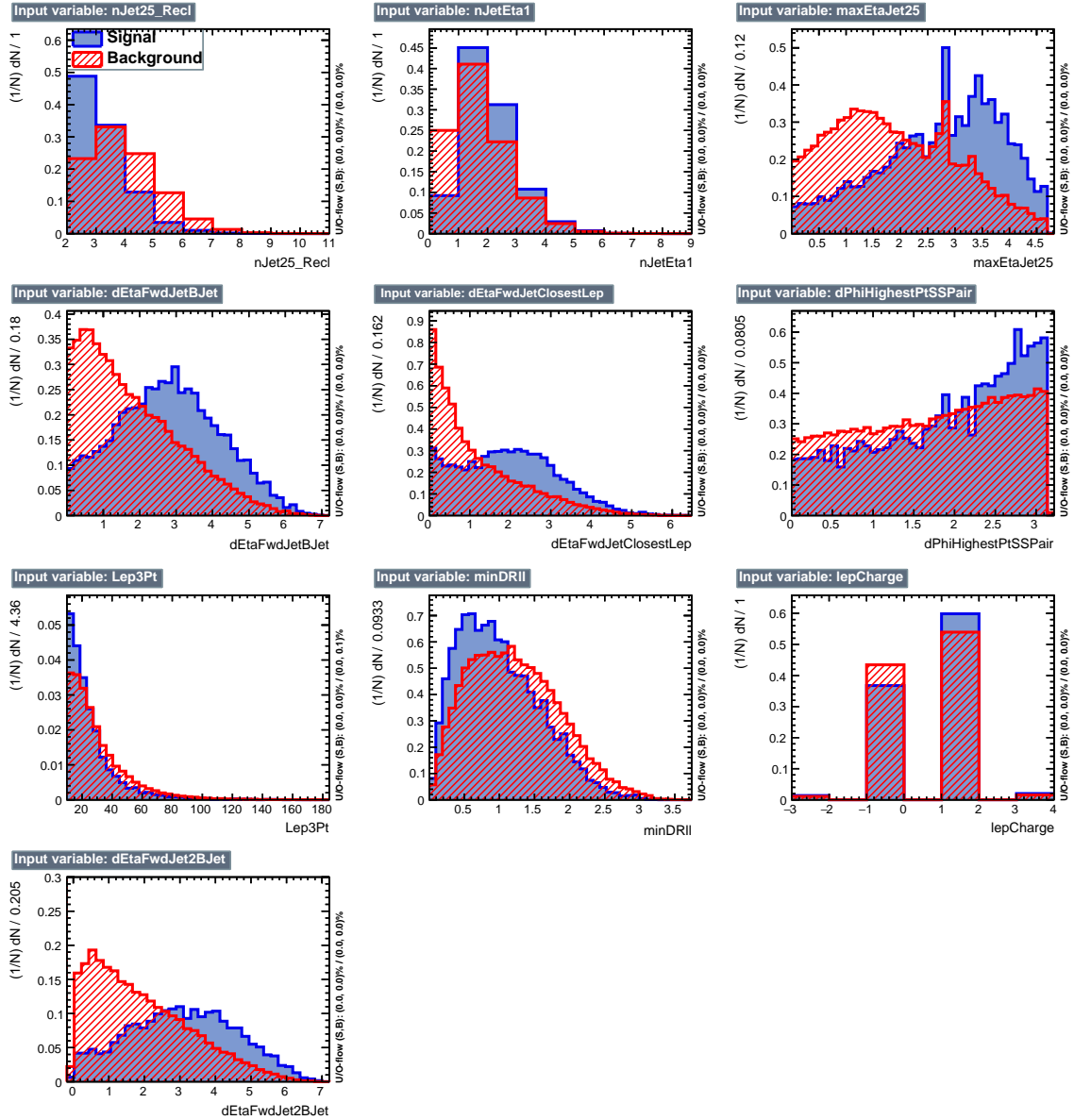


**Figure 6.8:** BDT inputs as seen by TMVA (signal, in blue, is  $tHq$ , background, in red, is  $t\bar{t}W+t\bar{t}Z$ ) for the three lepton channel, discriminated against  $t\bar{t}V$  background.

case a boosted decision tree (BDT) method however, correlations do not affect the performance. Figure 6.9 show the linear correlation coefficients for signal and background for the two training cases (the signal values are identical by construction). As expected, strong correlations appears for variables related to the forward jet activity. Same trend is seen in case of the same sign dilepton channel in Figure ??.

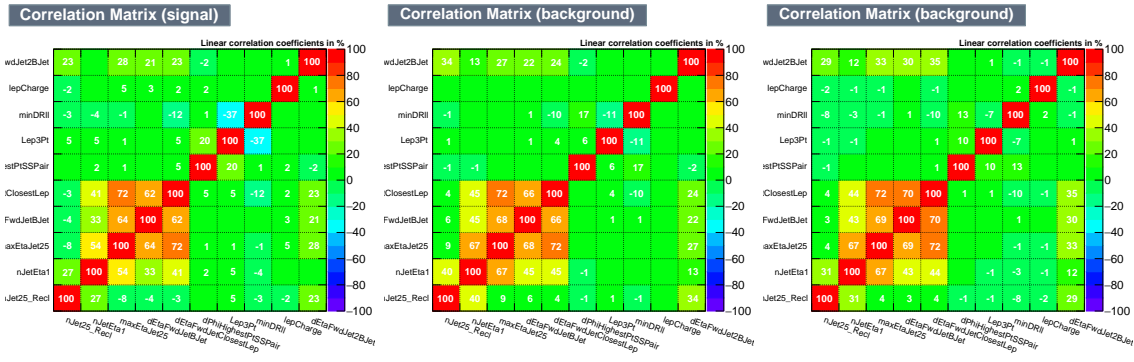


**Figure 6.9:** Signal (left),  $t\bar{t}$  background (middle), and  $t\bar{t}V$  background (right.) correlation matrices for the input variables in the TMVA analysis for the three lepton channel.

### 2524 6.8.1 Classifiers response

2525 Several MVA algorithms were evaluated to determine the most appropriate method  
 2526 for this analysis. The plots in Fig. 6.10 (top) show the background rejection as a  
 2527 function of the signal efficiency for  $t\bar{t}$  and  $t\bar{t}V$  trainings (ROC curves) for the different  
 2528 algorithms that were evaluated.

2529 In both cases the gradient boosted decision tree (“BDTA\_GRAD”) classifier offers  
 2530 the best results, followed by an adaptive BDT classifier (“BDTA”). The BDTA\_GRAD  
 2531 classifier output distributions for signal and backgrounds are shown on the bottom of  
 2532 Fig. 6.10. As expected, a good discrimination power is obtained using default discrim-  
 2533 inator parameter values, with minimal overtraining. TMVA provides a ranking of the  
 2534 input variables by their importance in the classification process, shown in Tab. 6.11.  
 2535 The TMVA settings used in the BDT training are shown in Tab. 6.12.

### 2536 6.9 Additional discriminating variables

2537 Two additional discriminating variables were tested considering the fact that the  
 2538 forward jet in the background could come from the pileup; since we have a real forward  
 2539 jet in the signal, it could give some improvement in the discriminating power. The

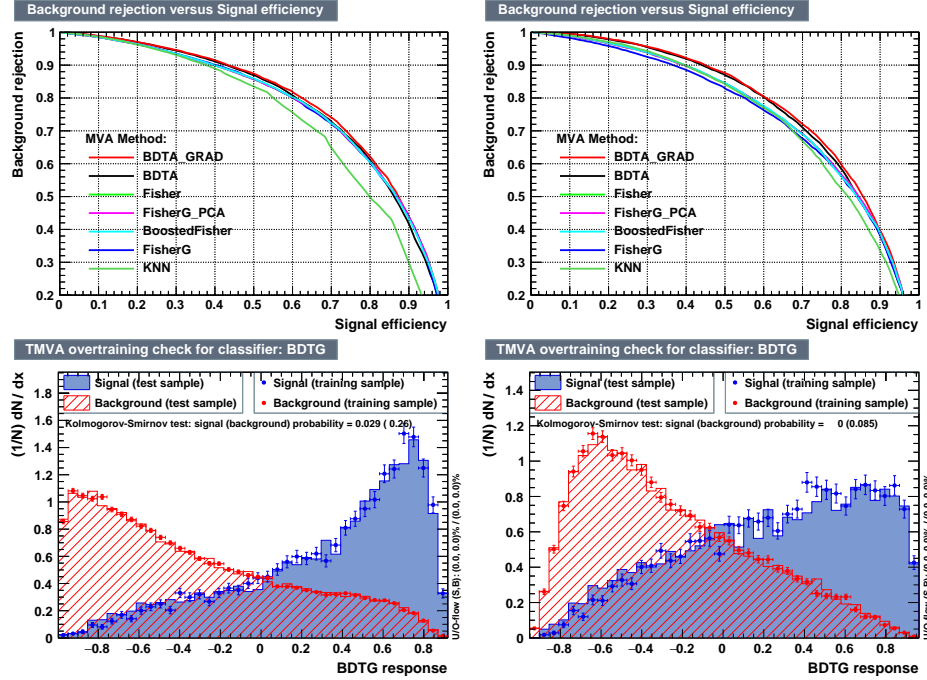


**Figure 6.10:** Top: background rejection vs signal efficiency (ROC curves) for various MVA classifiers (top) in the three lepton channel against  $t\bar{t}V$  (left) and  $t\bar{t}$  (right). Bottom: classifier output distributions for the gradient boosted decision trees, for training against  $t\bar{t}V$  (left) and against  $t\bar{t}$  (right).

ttbar training			ttV training		
Rank	Variable	Importance	Variable	Importance	
1	minDRll	1.329e-01	dEtaFwdJetBJet	1.264e-01	
2	dEtaFwdJetClosestLep	1.294e-01	Lep3Pt	1.224e-01	
3	dEtaFwdJetBJet	1.209e-01	maxEtaJet25	1.221e-01	
4	dPhiHighestPtSSPair	1.192e-01	dEtaFwdJet2BJet	1.204e-01	
5	Lep3Pt	1.158e-01	dEtaFwdJetClosestLep	1.177e-01	
6	maxEtaJet25	1.121e-01	minDRll	1.143e-01	
7	dEtaFwdJet2BJet	9.363e-02	dPhiHighestPtSSPair	9.777e-02	
8	nJetEta1	6.730e-02	nJet25_Recl	9.034e-02	
9	nJet25_Recl	6.178e-02	nJetEta1	4.749e-02	
10	lepCharge	4.701e-02	lepCharge	4.116e-02	

**Table 6.11:** TMVA input variables ranking for BDTA\_GRAD method for the trainings in the three lepton channel. For both trainings the rankings show almost the same 5 variables in the first places.

2540 additional variables describe the forward jet momentum (fwdJetPt25) and the forward  
 2541 jet identification(fwdJetPUID). Distributions for these variables in the three lepton  
 2542 channel are shown in the figure 6.11. The forward jet identification distribution show

---

```

TMVA.Types.kBDT
NTrees=800
BoostType=Grad
Shrinkage=0.10
!UseBaggedGrad
nCuts=50
MaxDepth=3
NegWeightTreatment=PairNegWeightsGlobal
CreateMVApdfs

```

---

**Table 6.12:** TMVA configuration used in the BDT training.

that for both, signal and background, jets are mostly real jets.

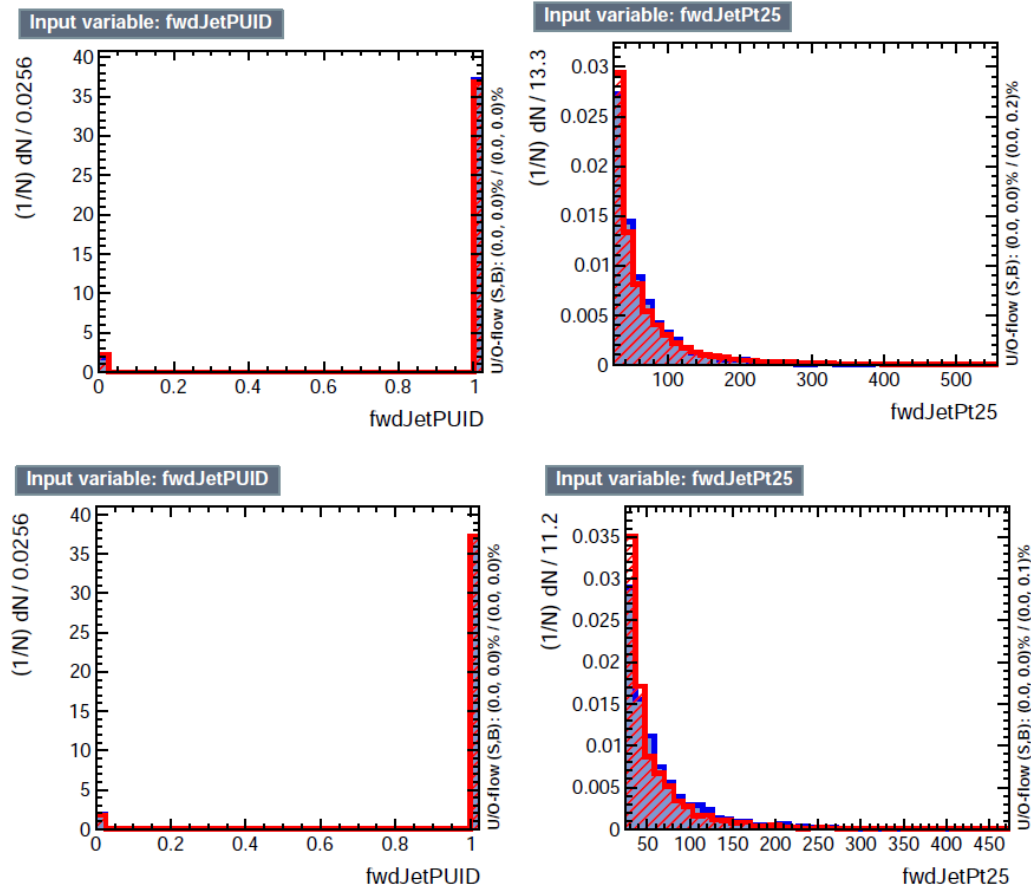


**Figure 6.11:** Additional discriminating variables distributions for ttv training (Top row) and tt training (bottom row) in the three lepton channel. The origin of the jets in the forward jet identification distribution is tagged as 0 for “pileup jets” while “real jets” are tagged as 1.

	ROC-integral
base 10 var ttv	0.848
+ fwdJetPUID ttv	0.849
+ fwdJetPt25 ttv	0.856
12 var ttv	0.856
base 10 var tt	0.777
+ fwdJetPUID tt	0.777
+ fwdJetPt25 tt	0.787
12 var	0.787

**Table 6.13:** ROC-integral for all the testing cases we made in the evaluation of the additional variables discriminating power. The improvement in the discrimination performance provided by the additional variables is about 1%

2544        The testing was made including in the MVA input one variable at a time, so we  
 2545        can evaluate the dicrimination power of each variable, and then both simultaneously.  
 2546        fwdJetPUID was ranked in the last place in importance (11) in both training (ttV  
 2547        and tt) while fwdJetPt25 was ranked 3 in the ttV training and 7 in the tt training.  
 2548        When training using 12 variables, fwdJetPt25 was ranked 5 and 7 in the ttV and tt  
 2549        trainings respectively, while fwdJetPUID was ranked 12 in both cases.

2550        The improvement in the discrimination performance provided by the additional  
 2551        variables is about 1%, so it was decided not to include them in the procedure. Table  
 2552        6.13 show the ROC-integral for all the testing cases we made.

2553 **References**

- 2554 [1] J. Schwinger. "Quantum Electrodynamics. I. A Covariant Formulation". Physical  
 2555 Review. 74 (10): 1439-61, (1948).
- 2556 [2] R. P. Feynman. "Space-Time Approach to Quantum Electrodynamics". Physical  
 2557 Review. 76 (6): 769-89, (1949).
- 2558 [3] S. Tomonaga. "On a Relativistically Invariant Formulation of the Quantum  
 2559 Theory of Wave Fields". Progress of Theoretical Physics. 1 (2): 27-42, (1946).
- 2560 [4] D.J. Griffiths, "Introduction to electrodynamics". 4th ed. Pearson, (2013).
- 2561 [5] F. Mandl, G. Shaw. "Quantum field theory." Chichester: Wiley (2009).
- 2562 [6] F. Halzen, and A.D. Martin, "Quarks and leptons: An introductory course in  
 2563 modern particle physics". New York: Wiley, (1984) .
- 2564 [7] File: Standard\_Model\_of\_Elementary\_Particle\_dark.svg. (2017, June 12)  
 2565 Wikimedia Commons, the free media repository. Retrieved November  
 2566 27, 2017 from <https://www.collegiate-advanced-electricity.com/single-post/2017/04/10/The-Standard-Model-of-Particle-Physics>.
- 2568 [8] E. Noether, "Invariante Variationsprobleme", Nachrichten von der Gesellschaft  
 2569 der Wissenschaften zu Göttingen, mathematisch-physikalische Klasse, vol. 1918,  
 2570 pp. 235-257, (1918).

- 2571 [9] C. Patrignani et al. (Particle Data Group), Chin. Phys. C, 40, 100001 (2016)  
2572 and 2017 update.
- 2573 [10] M. Goldhaber, L. Grodzins, A.W. Sunyar “Helicity of Neutrinos”, Phys. Rev.  
2574 109, 1015 (1958).
- 2575 [11] Palanque-Delabrouille N et al. “Neutrino masses and cosmology with Lyman-  
2576 alpha forest power spectrum”, JCAP 11 011 (2015).
- 2577 [12] M. Gell-Mann. “A Schematic Model of Baryons and Mesons”. Physics Letters.  
2578 8 (3): 214-215 (1964).
- 2579 [13] G. Zweig. “An SU(3) Model for Strong Interaction Symmetry and its Breaking”  
2580 (PDF). CERN Report No.8182/TH.401 (1964).
- 2581 [14] G. Zweig. “An SU(3) Model for Strong Interaction Symmetry and its Breaking:  
2582 II” (PDF). CERN Report No.8419/TH.412(1964).
- 2583 [15] M. Gell-Mann. “The Interpretation of the New Particles as Displaced Charged  
2584 Multiplets”. Il Nuovo Cimento 4: 848. (1956).
- 2585 [16] T. Nakano, K, Nishijima. “Charge Independence for V-particles”. Progress of  
2586 Theoretical Physics 10 (5): 581-582. (1953).
- 2587 [17] N. Cabibbo, “Unitary symmetry and leptonic decays” Physical Review Letters,  
2588 vol. 10, no. 12, p. 531, (1963).
- 2589 [18] M.Kobayashi, T.Maskawa, “CP-violation in the renormalizable theory of weak  
2590 interaction,” Progress of Theoretical Physics, vol. 49, no. 2, pp. 652-657, (1973).
- 2591 [19] File: Weak Decay (flipped).svg. (2017, June 12). Wikimedia Com-  
2592 mons, the free media repository. Retrieved November 27, 2017 from

- 2593 https://commons.wikimedia.org/w/index.php?title=File:Weak\_Decay\_(flipped)  
2594 .svg&oldid=247498592.
- 2595 [20] Georgia Tech University. Coupling Constants for the Fundamental  
2596 Forces(2005). Retrieved January 10, 2018, from http://hyperphysics.phy-  
2597 astr.gsu.edu/hbase/Forces/couple.html#c2
- 2598 [21] M. Strassler. (May 31, 2013).The Strengths of the Known Forces. Retrieved Jan-  
2599 uary 10, 2018, from https://profmattstrassler.com/articles-and-posts/particle-  
2600 physics-basics/the-known-forces-of-nature/the-strength-of-the-known-forces/
- 2601 [22] S.L. Glashow. “Partial symmetries of weak interactions”, Nucl. Phys. 22 579-  
2602 588, (1961).
- 2603 [23] A. Salam, J.C. Ward. “Electromagnetic and weak interactions”, Physics Letters  
2604 13 168-171, (1964).
- 2605 [24] S. Weinberg, “A model of leptons”, Physical Review Letters, vol. 19, no. 21, p.  
2606 1264, (1967).
- 2607 [25] M. Peskin, D. Schroeder, “An introduction to quantum field theory”. Perseus  
2608 Books Publishing L.L.C., (1995).
- 2609 [26] A. Pich. “The Standard Model of Electroweak Interactions”  
2610 https://arxiv.org/abs/1201.0537
- 2611 [27] F.Bellaiche. (2012, 2 September). “What’s this Higgs boson anyway?”. Retrieved  
2612 from: https://www.quantum-bits.org/?p=233
- 2613 [28] M. Endres et al. Nature 487, 454-458 (2012) doi:10.1038/nature11255

- 2614 [29] F. Englert, R. Brout. “Broken Symmetry and the Mass of Gauge  
 2615 Vector Mesons”. Physical Review Letters. 13 (9): 321-23.(1964)  
 2616 doi:10.1103/PhysRevLett.13.321
- 2617 [30] P.Higgs. “Broken Symmetries and the Masses of Gauge Bosons”. Physical Re-  
 2618 view Letters. 13 (16): 508-509,(1964). doi:10.1103/PhysRevLett.13.508.
- 2619 [31] G.Guralnik, C.R. Hagen and T.W.B. Kibble. “Global Conservation Laws  
 2620 and Massless Particles”. Physical Review Letters. 13 (20): 585-587, (1964).  
 2621 doi:10.1103/PhysRevLett.13.585.
- 2622 [32] CMS collaboration. “Observation of a new boson at a mass of 125 GeV with  
 2623 the CMS experiment at the LHC”. Physics Letters B. 716 (1): 30-61 (2012).  
 2624 arXiv:1207.7235. doi:10.1016/j.physletb.2012.08.021
- 2625 [33] ATLAS collaboration. “Observation of a New Particle in the Search for the Stan-  
 2626 dard Model Higgs Boson with the ATLAS Detector at the LHC”. Physics Letters  
 2627 B. 716 (1): 1-29 (2012). arXiv:1207.7214. doi:10.1016/j.physletb.2012.08.020.
- 2628 [34] ATLAS collaboration; CMS collaboration (26 March 2015). “Combined Mea-  
 2629 surement of the Higgs Boson Mass in pp Collisions at  $\sqrt{s}=7$  and 8 TeV with  
 2630 the ATLAS and CMS Experiments”. Physical Review Letters. 114 (19): 191803.  
 2631 arXiv:1503.07589. doi:10.1103/PhysRevLett.114.191803.
- 2632 [35] LHC InternationalMasterclasses“When protons collide”. Retrieved from [http://atlas.physicsmasterclasses.org/en/zpath\\_protoncollisions.htm](http://atlas.physicsmasterclasses.org/en/zpath_protoncollisions.htm)  
 2633
- 2634 [36] CMS Collaboration, “SM Higgs Branching Ratios and Total Decay Widths (up-  
 2635 date in CERN Report4 2016)”. <https://twiki.cern.ch/twiki/bin/view/LHCPhysics/CERNYellowReportPageBR> , last accessed on 17.12.2017.

- 2637 [37] R.Grant V. “Determination of Higgs branching ratios in  $H \rightarrow W^+W^- \rightarrow l\nu jj$   
2638 and  $H \rightarrow ZZ \rightarrow l^+l^-jj$  channels”. Physics Department, University of Ten-  
2639 nessee (Dated: October 31, 2012). Retrieved from <http://aesop.phys.utk.edu/ph611/2012/projects/Riley.pdf>
- 2640
- 2641 [38] LHC Higgs Cross Section Working Group, Denner, A., Heinemeyer, S. et al.  
2642 “Standard model Higgs-boson branching ratios with uncertainties”. Eur. Phys.  
2643 J. C (2011) 71: 1753. <https://doi.org/10.1140/epjc/s10052-011-1753-8>
- 2644 [39] F. Maltoni, K. Paul, T. Stelzer, and S. Willenbrock, “Associated production  
2645 of Higgs and single top at hadron colliders”, Phys.Rev. D64 (2001) 094023,  
2646 [hep-ph/0106293].
- 2647 [40] S. Biswas, E. Gabrielli, F. Margaroli, and B. Mele, “Direct constraints on the  
2648 top-Higgs coupling from the 8 TeV LHC data,” Journal of High Energy Physics,  
2649 vol. 07, p. 073, (2013).
- 2650 [41] M. Farina, C. Grojean, F. Maltoni, E. Salvioni, and A. Thamm, “Lifting de-  
2651 generacies in Higgs couplings using single top production in association with a  
2652 Higgs boson,” Journal of High Energy Physics, vol. 05, p. 022, (2013).
- 2653 [42] T.M. Tait and C.-P. Yuan, “Single top quark production as a window to physics  
2654 beyond the standard model”, Phys. Rev. D 63 (2000) 014018 [hep-ph/0007298].
- 2655 [43] F. Demartin, F. Maltoni, K. Mawatari, and M. Zaro, “Higgs production in  
2656 association with a single top quark at the LHC,” European Physical Journal C,  
2657 vol. 75, p. 267, (2015).

- 2658 [44] CMS Collaboration, “Modelling of the single top-quark production in associa-  
 2659 tion with the Higgs boson at 13 TeV.” [https://twiki.cern.ch/twiki/bin/](https://twiki.cern.ch/twiki/bin/viewauth/CMS/SingleTopHiggsGeneration13TeV)  
 2660 [viewauth/CMS/SingleTopHiggsGeneration13TeV](#), last accessed on 16.01.2018.
- 2661 [45] CMS Collaboration, “SM Higgs production cross sections at  $\sqrt{s} =$   
 2662 13 TeV.” [https://twiki.cern.ch/twiki/bin/](https://twiki.cern.ch/twiki/bin/view/LHCPhysics/CERNYellowReportPageAt13TeV)  
 2663 [view/LHCPhysics/CERNYellowReportPageAt13TeV](#), last accessed on 16.01.2018.
- 2664 [46] S. Dawson, The effective W approximation, Nucl. Phys. B 249 (1985) 42.
- 2665 [47] S. Biswas, E. Gabrielli and B. Mele, JHEP 1301 (2013) 088 [[arXiv:1211.0499 \[hep-ph\]](#)].
- 2667 [48] F. Demartin, B. Maier, F. Maltoni, K. Mawatari, and M. Zaro, “tWH associated  
 2668 production at the LHC”, European Physical Journal C, vol. 77, p. 34, (2017).  
 2669 [arXiv:1607.05862](#)
- 2670 [49] LHC Higgs Cross Section Working Group, “Handbook of LHC Higgs Cross  
 2671 Sections: 4.Deciphering the Nature of the Higgs Sector”, [arXiv:1610.07922](#).
- 2672 [50] J. Ellis, D. S. Hwang, K. Sakurai, and M. Takeuchi.“Disentangling Higgs-Top  
 2673 Couplings in Associated Production”, JHEP 1404 (2014) 004, [[arXiv:1312.5736](#)].
- 2674 [51] CMS Collaboration, V. Khachatryan et al., “Precise determination of the mass  
 2675 of the Higgs boson and tests of compatibility of its couplings with the standard  
 2676 model predictions using proton collisions at 7 and 8 TeV,” [arXiv:1412.8662](#).
- 2677 [52] ATLAS Collaboration, G. Aad et al., “Updated coupling measurements of the  
 2678 Higgs boson with the ATLAS detector using up to  $25 \text{ fb}^{-1}$  of proton-proton  
 2679 collision data”, ATLAS-CONF-2014-009.

- 2680 [53] ATLAS and CMS Collaborations, “Measurements of the Higgs boson produc-  
2681 tion and decay rates and constraints on its couplings from a combined ATLAS  
2682 and CMS analysis of the LHC pp collision data at  $\sqrt{s} = 7$  and 8 TeV,” (2016).  
2683 CERN-EP-2016-100, ATLAS-HIGG-2015-07, CMS-HIG-15-002.
- 2684 [54] File:Cern-accelerator-complex.svg. Wikimedia Commons,  
2685 the free media repository. Retrieved January, 2018 from  
2686 <https://commons.wikimedia.org/wiki/File:Cern-accelerator-complex.svg>
- 2687 [55] J.L. Caron , “Layout of the LEP tunnel including future LHC infrastructures.”,  
2688 (Nov, 1993). A C Collection. Legacy of AC. Pictures from 1992 to 2002. Re-  
2689 trieval from <https://cds.cern.ch/record/841542>
- 2690 [56] M. Vretenar, “The radio-frequency quadrupole”. CERN Yellow Report CERN-  
2691 2013-001, pp.207-223 DOI:10.5170/CERN-2013-001.207. arXiv:1303.6762
- 2692 [57] L.Evans. P. Bryant (editors). “LHC Machine”. JINST 3 S08001 (2008).
- 2693 [58] CERN Photographic Service.“Radio-frequency quadrupole, RFQ-1”, March  
2694 1983, CERN-AC-8303511. Retrieved from <https://cds.cern.ch/record/615852>.
- 2695 [59] CERN Photographic Service “Animation of CERN’s accelerator net-  
2696 work”, 14 October 2013. DOI: 10.17181/cds.1610170 Retrieved from  
2697 <https://videos.cern.ch/record/1610170>
- 2698 [60] C.Sutton. “Particle accelerator”.Encyclopedia Britannica. July 17, 2013. Re-  
2699 trieval from <https://www.britannica.com/technology/particle-accelerator>.
- 2700 [61] L.Guiraud. “Installation of LHC cavity in vacuum tank.”. July 27 2000. CERN-  
2701 AC-0007016. Retrieved from <https://cds.cern.ch/record/41567>.

- 2702 [62] J.L. Caron, “Magnetic field induced by the LHC dipole’s superconducting coils”.  
2703 March 1998. AC Collection. Legacy of AC. Pictures from 1992 to 2002. LHC-  
2704 PHO-1998-325. Retrieved from <https://cds.cern.ch/record/841511>
- 2705 [63] AC Team. “Diagram of an LHC dipole magnet”. June 1999. CERN-DI-9906025  
2706 retrieved from <https://cds.cern.ch/record/40524>.
- 2707 [64] CMS Collaboration “Public CMS Luminosity Information”.  
2708 <https://twiki.cern.ch/twiki/bin/view/CMSPublic/LumiPublicResults#2016>  
2709 \_proton\_proton\_13\_TeV\_collis, last accessed 24.01.2018
- 2710 [65] J.L. Caron. “LHC Layout” AC Collection. Legacy of AC. Pictures  
2711 from 1992 to 2002. September 1997, LHC-PHO-1997-060. Retrieved from  
2712 <https://cds.cern.ch/record/841573>.
- 2713 [66] J.A. Coarasa. “The CMS Online Cluster: Setup, Operation and Maintenance  
2714 of an Evolving Cluster”. ISGC 2012, 26 February - 2 March 2012, Academia  
2715 Sinica, Taipei, Taiwan.
- 2716 [67] CMS Collaboration. “The CMS experiment at the CERN LHC” JINST 3 S08004  
2717 (2008).
- 2718 [68] CMS Collaboration. “CMS detector drawings 2012” CMS-PHO-GEN-2012-002.  
2719 Retrieved from <http://cds.cern.ch/record/1433717>.
- 2720 [69] R. Breedon. “View through the CMS detector during the cooldown of the  
2721 solenoid on February 2006. CMS Collection”, February 2006, CMS-PHO-  
2722 OREACH-2005-004, Retrieved from <https://cds.cern.ch/record/930094>.
- 2723 [70] A. Dominguez et. al. “CMS Technical Design Report for the Pixel Detector  
2724 Upgrade”, CERN-LHCC-2012-016. CMS-TDR-11.

- 2725 [71] CMS Collaboration. “Description and performance of track and primary-vertex  
2726 reconstruction with the CMS tracker,” Journal of Instrumentation, vol. 9, no.  
2727 10, p. P10009,(2014).
- 2728 [72] CMS Collaboration and M. Brice. “Images of the CMS Tracker Inner  
2729 Barrel”, November 2008, CMS-PHO-TRACKER-2008-002. Retrieved from  
2730 <https://cds.cern.ch/record/1431467>.
- 2731 [73] M. Weber. “The CMS tracker”. 6th international conference on hyperons, charm  
2732 and beauty hadrons Chicago, June 28-July 3 2004.
- 2733 [74] CMS Collaboration. “Projected Performance of an Upgraded CMS Detector at  
2734 the LHC and HL-LHC: Contribution to the Snowmass Process”. Jul 26, 2013.  
2735 arXiv:1307.7135
- 2736 [75] L. Veillet. “End assembly of HB with EB rails and rotation in-  
2737 side SX ”,January 2002. CMS-PHO-HCAL-2002-002. Retrieved from  
2738 <https://cds.cern.ch/record/42594>.
- 2739 [76] J. Puerta-Pelayo.“First DT+RPC chambers installation round in the  
2740 UX5 cavern.”. January 2007, CMS-PHO-OREACH-2007-001. Retrieved from  
2741 <https://cds.cern.ch/record/1019185>
- 2742 [77] X. Cid Vidal and R. Cid Manzano. “CMS Global Muon Trigger” web  
2743 site: Taking a closer look at LHC. Retrieved from [https://www.lhc-closer.es/taking\\_a\\_closer\\_look\\_at\\_lhc/0.lhc\\_trigger](https://www.lhc-closer.es/taking_a_closer_look_at_lhc/0.lhc_trigger)
- 2745 [78] WLCG Project Office, “Documents & Reference - Tiers - Structure,” (2014).  
2746 <http://wlcg.web.cern.ch/documents-reference> , last accessed on 30.01.2018.

- 2747 [79] CMS Collaboration. “CMSSW Application Framework”,  
 2748 <https://twiki.cern.ch/twiki/bin/view/CMSPublic/WorkBookCMSSWFramework>,  
 2749 last accesses 06.02.2018
- 2750 [80] A. Buckleya, J. Butterworthb, S. Giesekec, et. al. “General-purpose event gen-  
 2751 erators for LHC physics”. arXiv:1101.2599v1 [hep-ph] 13 Jan 2011
- 2752 [81] A. Quadt. “Top Quark Physics at Hadron Colliders”. Advances in the Physics  
 2753 of Particles and Nuclei. Springer-Verlag Berlin Heidelberg. DOI: 10.1007/978-  
 2754 3-540-71060-8 (2007)
- 2755 [82] DurhamHep Data Project, “The Durham HepData Project - PDF Plotter.”  
 2756 <http://hepdata.cedar.ac.uk/pdf/pdf3.html> , last accessed on 02.02.2018.
- 2757 [83] F. Maltoni, G. Ridolfi, and M. Ubiali, “b-initiated processes at the LHC: a  
 2758 reappraisal,” Journal of High Energy Physics, vol. 07, p. 022, (2012).
- 2759 [84] B. Andersson, G. Gustafson, G.Ingelman and T. Sjostrand, “Parton fragmen-  
 2760 tation and string dynamics”, Physics Reports, Vol. 97, No. 2-3, pp. 31-145,  
 2761 1983.
- 2762 [85] CMS Collaboration, “Event generator tunes obtained from underlying event  
 2763 and multiparton scattering measurements;” European Physical Journal C, vol.  
 2764 76, no. 3, p. 155, (2016).
- 2765 [86] J. Alwall et. al., “The automated computation of tree-level and next-to-leading  
 2766 order differential cross sections, and their matching to parton shower simula-  
 2767 tions,” Journal of High Energy Physics, vol. 07, p. 079, (2014).

- 2768 [87] S. Frixione, P. Nason, and C. Oleari, “Matching NLO QCD computations with  
 2769 Parton Shower simulations: the POWHEG method,” Journal of High Energy  
 2770 Physics, vol. 11, p. 070, (2007).
- 2771 [88] S. Agostinelli et al., “GEANT4: A Simulation toolkit,” Nuclear Instruments  
 2772 and Methods in Physics, vol. A506, pp. 250–303, (2003).
- 2773 [89] J.Allison et.al.,“Recent developments in Geant4”, Nuclear Instruments and  
 2774 Methods in Physics Research A 835 (2016) 186-225.
- 2775 [90] CMS Collaboration “Full Simulation Offline Guide”, <https://twiki.cern.ch/twiki/bin/view/CMSPublic/SWGuideSimulation>, last accessed 04.02.2018
- 2777 [91] A. Giammanco. “The Fast Simulation of the CMS Experiment” J. Phys.: Conf.  
 2778 Ser. 513 022012 (2014)
- 2779 [92] A.M. Sirunyan et. al. “Particle-flow reconstruction and global event description  
 2780 with the CMS detector”, JINST 12 P10003 (2017) <https://doi.org/10.1088/1748-0221/12/10/P10003>.
- 2782 [93] The CMS Collaboration. “ Description and performance of track and pri-  
 2783 mary vertex reconstruction with the CMS tracker”. JINST 9 P10009 (2014).  
 2784 doi:10.1088/1748-0221/9/10/P10009
- 2785 [94] J. Incandela. “Status of the CMS SM Higgs Search” July 4, 2012. Pdf slides.  
 2786 Retrieved from [https://indico.cern.ch/event/197461/contributions/1478917/attachments/290954/406673/CMS\\_4July2012\\_Final.pdf](https://indico.cern.ch/event/197461/contributions/1478917/attachments/290954/406673/CMS_4July2012_Final.pdf)
- 2788 [95] P. Billoir and S. Qian, “Simultaneous pattern recognition and track fitting by  
 2789 the Kalman filtering method”, Nucl. Instrum. Meth. A 294 219. (1990).

- 2790 [96] W. Adam, R. Fruhwirth, A. Strandlie and T. Todorov, “Reconstruction of  
 2791 electrons with the Gaussian sum filter in the CMS tracker at LHC”, eConf  
 2792 C 0303241 (2003) TULT009 [physics/0306087].
- 2793 [97] K. Rose, “Deterministic Annealing for Clustering, Compression, Classification,  
 2794 Regression and related Optimisation Problems”, Proc. IEEE 86 (1998) 2210.
- 2795 [98] R. Fruhwirth, W. Waltenberger and P. Vanlaer, “ Adaptive Vertex Fitting”,  
 2796 CMS Note 2007-008 (2007).
- 2797 [99] CMS collaboration, “Performance of CMS muon reconstruction in pp collision  
 2798 events at  $\sqrt{s} = 7$  TeV ”, JINST 7 P10002 2012, [arXiv:1206.4071].
- 2799 [100] M. Cacciari, G. P. Salam, and G. Soyez, “The anti- $k_t$  jet clustering algorithm,”  
 2800 Journal of High Energy Physics, vol. 04, p. 063, (2008).
- 2801 [101] B. Dorney. “Anatomy of a Jet in CMS”. Quantum Diaries. June  
 2802 1st, 2011. Retrieved from <https://www.quantumdiaries.org/2011/06/01/anatomy-of-a-jet-in-cms/>
- 2804 [102] The CMS Collaboration.“Event Displays from the high-energy collisions at 7  
 2805 TeV”, May 2010, CMS-PHO-EVENTS-2010-007, Retrieved from <https://cds.cern.ch/record/1429614>.
- 2807 [103] The CMS collaboration. “Determination of jet energy calibration and transverse  
 2808 momentum resolution in CMS”. JINST 6 P11002 (2011). <http://dx.doi.org/10.1088/1748-0221/6/11/P11002>
- 2810 [104] The CMS Collaboration, “Introduction to Jet Energy Corrections at  
 2811 CMS.”. <https://twiki.cern.ch/twiki/bin/view/CMS/IntroToJEC>, last ac-  
 2812 cessed 10.02.2018.

- 2813 [105] CMS Collaboration Collaboration. “Identification of b quark jets at the CMS  
2814 Experiment in the LHC Run 2”. Tech. rep. CMS-PAS-BTV-15-001. Geneva:  
2815 CERN, (2016). <https://cds.cern.ch/record/2138504>.
- 2816 [106] CMS Collaboration Collaboration. “Performance of missing energy reconstruc-  
2817 tion in 13 TeV pp collision data using the CMS detector”. Tech. rep. CMS-PAS-  
2818 JME16-004. Geneva: CERN, 2016. <https://cds.cern.ch/record/2205284>.
- 2819 [107] CMS Collaboration, “New CMS results at Moriond (Electroweak) 2013”,  
2820 Retrieved from <http://cms.web.cern.ch/sites/cms.web.cern.ch/files/>  
2821 styles/large/public/field/image/HIG13004\_Event01\_0.png?itok=  
2822 LAwZzPHR
- 2823 [108] CMS Collaboration, “New CMS results at Moriond (Electroweak) 2013”,  
2824 Retrieved from <http://cms.web.cern.ch/sites/cms.web.cern.ch/>  
2825 files/styles/large/public/field/image/TOP12035\_Event01.png?itok=  
2826 uMdnSqzC
- 2827 [109] K. Skovpen. “Event displays highlighting the main properties of heavy flavour  
2828 jets in the CMS Experiment”, Aug 2017, CMS-PHO-EVENTS-2017-006. Re-  
2829 trieved from <https://cds.cern.ch/record/2280025>.
- 2830 [110] G. Cowan. “Topics in statistical data analysis for high-energy physics”.  
2831 arXiv:1012.3589v1
- 2832 [111] A. Hoecker et al., “TMVA-Toolkit for multivariate data analysis”  
2833 arXiv:physics/0703039v5 (2009)

- 2834 [112] L. Lista. “Statistical Methods for Data Analysis in Particle Physics”, 2nd  
2835 ed. Springer International Publishing. (2017) <https://dx.doi.org/10.1007/978-3-319-62840-0>
- 2837 [113] I. Antcheva et al., “ROOT-A C++ framework for petabyte data storage, sta-  
2838 tistical analysis and visualization ,” Computer Physics Communications, vol.  
2839 182, no. 6, pp. 1384â€¢1385, (2011).
- 2840 [114] Y. Coadou. “Boosted decision trees”, ESIPAP, Archamps, 9 Febru-  
2841 ary 2016. Lecture. Retrieved from [https://indico.cern.ch/event/472305/contributions/1982360/attachments/1224979/1792797/ESIPAP\\_MVA160208-BDT.pdf](https://indico.cern.ch/event/472305/contributions/1982360/attachments/1224979/1792797/ESIPAP_MVA160208-BDT.pdf)
- 2844 [115] J.H. Friedman. “Greedy function approximation: A gradient boosting ma-  
2845 chine”. Ann. Statist. Volume 29, Number 5 (2001), 1189-1232. [https://projecteuclid.org/download/pdf\\_1/euclid-aos/1013203451](https://projecteuclid.org/download/pdf_1/euclid-aos/1013203451).
- 2847 [116] F. James, M. Roos, “MINUIT: Function minimization and error analysis”. Cern  
2848 Computer Centre Program Library, Geneve Long Write-up No. D506, 1989
- 2849 [117] J. Neyman and E. S. Pearson, “On the problem of the most efficient tests  
2850 of statistical hypotheses”. Philosophical Transactions of the Royal Society of  
2851 London. Series A, Containing Papers of a Mathematical or Physical Character.  
2852 Vol. 231 (1933), pp. 289-337
- 2853 [118] B. Hespel, F. Maltoni, and E. Vryonidou, “Higgs and Z boson associated pro-  
2854 duction via gluon fusion in the SM and the 2HDM”, JHEP 06 (2015) 065,  
2855 [https://dx.doi.org/10.1007/JHEP06\(2015\)065](https://dx.doi.org/10.1007/JHEP06(2015)065), arXiv:1503.01656.

- 2856 [119] ATLAS Collaboration, “Measurements of Higgs boson produc-  
 2857 tion and couplings in diboson final states with the ATLAS  
 2858 detector at the LHC”, Phys. Lett. B726 (2013) 88âš119,  
 2859 doi:10.1016/j.physletb.2014.05.011,10.1016/j.physletb.2013.08.010,  
 2860 arXiv:1307.1427. [Erratum: Phys. Lett.B734,406(2014)].
- 2861 [120] CMS Collaboration, “Search for the associated production of a Higgs boson  
 2862 with a single top quark in proton-proton collisions at  $\sqrt{s} = 8$  TeV”, JHEP 06  
 2863 (2016) 177,doi:10.1007/JHEP06(2016)177, arXiv:1509.08159.
- 2864 [121] B. Stieger, C. Jordà Lope et al., “Search for Associated Production of a Single  
 2865 Top Quark and a Higgs Boson in Leptonic Channels”, CMS Analysis Note CMS  
 2866 AN-14-140, 2014.
- 2867 [122] M. Peruzzi, C. Mueller, B. Stieger et al., “Search for ttH in multilepton final  
 2868 states at  $\sqrt{s} = 13$  TeV”, CMS Analysis Note CMS AN-16-211, 2016.
- 2869 [123] CMS Collaboration, “Search for H to bbar in association with a single top quark  
 2870 as a test of Higgs boson couplings at  $\sqrt{s} = 13$  TeV”, CMS Physics Analysis  
 2871 Summary CMS-PAS-HIG-16-019, 2016.
- 2872 [124] CMS Collaboration, “Search for production of a Higgs boson and a single top  
 2873 quark in multilepton final states in proton collisions at  $\sqrt{s} = 13$  TeV”, CMS  
 2874 Physics Analysis Summary CMS-PAS-HIG-17-005, 2016.
- 2875 [125] B. WG, “BtagRecommendation80XReReco”, February, 2017. <https://twiki.cern.ch/twiki/bin/view/CMS/BtagRecommendation80XReReco>.

- 2877 [126] CMS Collaboration, “Identification of b quark jets at the CMS Experiment  
 2878 in the LHC Run 2”, CMS Physics Analysis Summary CMS-PAS-BTV-15-001,  
 2879 2016.
- 2880 [127] M. Peruzzi, F. Romeo, B. Stieger et al., “Search for ttH in multilepton final1  
 2881 states at  $\sqrt{s} = 13$  TeV”, CMS Analysis Note CMS AN-17-029, 2017.
- 2882 [128] CMS Collaboration, “Baseline muon selections for Run-II.” <https://twiki.cern.ch/twiki/bin/view/CMSPublic/SWGuideMuonIdRun2>, last accessed on  
 2883 24.02.2018.
- 2885 [129] G. Petrucciani and C. Botta, “Two step prompt muon identification”, January,  
 2886 2015. <https://indico.cern.ch/event/368007/contribution/2/material/slides/0.pdf>.
- 2888 [130] H. Brun and C. Ochando, “Updated Results on MVA eID with 13 TeV samples”,  
 2889 October, 2014. <https://indico.cern.ch/event/298249/contribution/3/material/slides/0.pdf>.
- 2891 [131] K. Rehermann and B. Tweedie, “Efficient Identification of Boosted Semileptonic  
 2892 Top Quarks at the LHC”, JHEP 03 (2011) 059, [https://dx.doi.org/10.1007/JHEP03\(2011\)059](https://dx.doi.org/10.1007/JHEP03(2011)059), arXiv:1007.2221.
- 2894 [132] CMS Collaboration. “Tag and Probe”, <https://twiki.cern.ch/twiki/bin/view/CMSPublic/TagAndProbe>, last accessed on 02.03.2018.
- 2896 [133] B. Maier, “SingleTopHiggProduction13TeV”, February, 2016.  
 2897 <https://twiki.cern.ch/twiki/bin/viewauth/CMS/SingleTopHiggsGeneration13TeV>.